TRIMMED MULTILEVEL FAST MULTIPOLE ALGORITHM FOR D-TYPE VOLUME INTEGRAL EQUATIONS IN ELECTROMAGNETIC SCATTERING PROBLEMS

A THESIS SUBMITTED TO

THE GRADUATE SCHOOL OF ENGINEERING AND SCIENCE

OF BILKENT UNIVERSITY

IN PARTIAL FULFILLMENT OF THE REQUIREMENTS FOR

THE DEGREE OF

MASTER OF SCIENCE

IN

ELECTRICAL AND ELECTRONICS ENGINEERING

By

Halil Topözlü

August 2022

TRIMMED MULTILEVEL FAST MULTIPOLE ALGORITHM FOR D-TYPE VOLUME INTEGRAL EQUATIONS IN ELECTROMAGNETIC SCATTERING PROBLEMS

By Halil Topözlü

August 2022

We certify that we have read this thesis and that in our opinion it is fully adequate, in scope and in quality, as a thesis for the degree of Master of Science.

Vakur Behçet Ertürk (Advisor)

Barışcan Karaosmanoğlu(Co-Advisor)

Orhan Arıkan

Seyit Sencer Koç

Approved for the Graduate School of Engineering and Science:

Orhan Arıkan
Director of the Graduate School

ABSTRACT

TRIMMED MULTILEVEL FAST MULTIPOLE ALGORITHM FOR D-TYPE VOLUME INTEGRAL EQUATIONS IN ELECTROMAGNETIC SCATTERING PROBLEMS

Halil Topözlü
M.S. in Electrical and Electronics Engineering
Advisor: Vakur Behçet Ertürk
August 2022

The Multilevel Fast Multipole Algorithm (MLFMA) is a state of the art computational method that requires $\mathcal{O}(NlogN)$ memory and computational complexity for N unknowns. Despite the low memory and computational complexity, the conventional MLFMA has still some challenges due to prolonging iterations for large-scale electromagnetic scattering problems, especially for volumetric problems.

We present a novel application of trimmed MLFMA (T-MLFMA) to D-type volume integral equations. In T-MLFMA, thresholding and machine learning (ML) techniques are performed to eliminate the unneeded interactions as the MLFMA iterations proceed. Particularly, the converged current coefficients are determined via a Fully Connected Neural Network (FCNN), and the tree structure is systematically modified and becomes sparser. Therefore, the convergence of the problem is accelerated while matrix-vector multiplication time per iteration is also reduced. The training of the network is performed with only a small size of homogeneous dielectric spheres with different permittivity values. Then, we attack the scattering problem of homogeneous and inhomogeneous relatively more complex dielectric geometries, such as spherical shell layer, cone, torus, cylinder, cube, etc. As a result, significant speed-up is achieved with a controllable and limited error with respect to the conventional MLFMA in all simulations.

Keywords: MLFMA, D-type volume integral equations, machine learning.

ÖZET

ELEKTROMANYETIK SACILMA PROBLEMLERINDEKI D-TIPI HACIM INTEGRAL DENKLEMLERININ KIRPILMIS ÇOK SEVIYELI ÇOKKUTUP YONTEMI ILE COZULMESI

Halil Topözlü
Elektrik ve Elektronik Mühendisliği, Yüksek Lisans
Tez Danışmanı: Vakur Behçet Ertürk
Ağustos 2022

Çok Seviyeli Hızlı Çok Kutup Yöntemi (ÇSHÇY), N bilinmeyen sayısı için $\mathcal{O}(NlogN)$ bellek ve hesaplama karmaşıklığı gerektiren en hızlı ve hassas hesaplama yöntemlerinden bir tanesidir. Düşük bellek ve hesaplama karmaşıklığına rağmen geleneksel ÇSHÇY, büyük ölçekli elektromanyetik saçılma problemleri, özellikle de hacimsel problemler için yüksek iterasyon sayısı nedeniyle hala bazı zorluklara sahiptir.

Bu çalışmada, D-tipi hacim integral denklemlerine kırpılmış ÇSHÇY'nın (K-ÇSHÇY) yeni bir uygulamasını sunuyoruz. K-ÇSHÇY'de, ÇSHÇY iterasyonları ilerledikçe gereksiz etkileşimler eşikleme ve makine öğrenimi (MÖ) teknikleri uygulanarak ortadan kaldırılır. Özellikle yakınsayan akım katsayıları, Tam Bağlantılı Sinir Ağı (TBSA) aracılığıyla belirlenir ve ağaç yapısı sistematik olarak değiştirilir ve daha seyrek hale gelir. Bu nedenle, her bir iterasyondaki matris-vektör çarpım süresi azalırken, problemin yakınsaması hızlandırılır. Ağın eğitimi için farklı dielektrik geçirgenlik değerlerine sahip sadece küçük boyutlu homojen kürelerin yeterli olduğu gözlemlenmiştir. Ardından, küresel kabuk tabakası, koni, torus, silindir, küp vb. gibi homojen ve homojen olmayan nispeten daha karmaşık geometrilerin saçılma problemleri bu sinir ağı kullanılarak çözülür. Sonuç olarak, tüm denemelerde geleneksel ÇSHÇY'ye göre kontrol edilebilir ve sınırlı bir hata ile önemli bir hızlanma elde edilir.

Anahtar sözcükler: ÇSHÇY, D-tipi hacim integral denklemleri, makine öğrenmesi.

Acknowledgement

Firstly, I would like to thank my advisor Prof. Vakur B. Ertürk for giving me the opportunity to work with him. In the past three years, he taught me how to become a better researcher step by step. He consistently guided me the right way and inspired me with his knowledge. His advice always will be in my pocket throughout my life.

I also would like to thank my co-advisor, Barışcan Karaosmanoğlu, for his invaluable contribution to this thesis. He always showed me the light in my darkest times. I learned a lot from him and he always advised me to question each and every detail in my research. He is a lifelong friend more than a mentor.

I am also grateful to my thesis committee members Prof. Orhan Arıkan and Prof. Seyit Sencer Koç for kindly accepting to review this thesis.

I would like to Aselsan Inc. for allowing me to use workstations for all simulations presented in this work.

Also, I am always grateful to all of my friends for their endless support and advice.

Finally but most importantly, I would like to express my deepest gratitude to my family. I am here due to their love. This thesis is dedicated to them.

Contents

List of Figures

List of Tables

Chapter 1

Introduction

The analyses of scattering problems have been rigorously investigated with computational electromagnetics (CEM) due to the advent of computers and improvements in numerical methods. The numerical solution of electromagnetic (EM) scattering problems is achieved mainly by solving either integral or partial-differential equations [1]. Integral equation-based solvers are one of the most commonly used classes of numerical methods to examine the EM scattering problems which involve homogeneous and/or inhomogeneous structures [2]. The homogeneous scatterers are mainly solved via surface integral equations (SIEs). However, usage of volume integral equations (VIEs) is inevitable in the analysis of highly inhomogeneous scatterers [3, 4]. These integral equations are converted into a system of linear equations by Method of Moments (MoM), which unfortunately requires high memory and computational complexity. The memory complexity is $\mathcal{O}(N^2)$ for both iterative and direct solvers, while the computational complexity is $\mathcal{O}(N^2)$ per iteration for iterative solvers, and $\mathcal{O}(N^3)$ for direct solvers for N unknowns [5]. On the other hand, as a state-of-the-art computational method, Multilevel Fast Multipole Algorithm (MLFMA), which is a hierarchical version of the Fast Multipole Method (FMM) [6], reduces both memory and computational complexity to $\mathcal{O}(NlogN)$ [7]. The improvement in the complexity of MLFMA comes from the group-by-group computations in different stages, which mainly use the factorization and diagonalization of the free-space Green's function. Therefore, large-scale problems can be solved faster with limited resources effectively [8, 9, 24].

In the literature, also some high-frequency techniques (physical optics (PO), geometrical optics (GO), etc.) are used to solve the scattering problems approximately under some assumptions, and these techniques provide fast solutions [10]. However, these techniques are not used in many applications due to their low accuracy [11]. Therefore, some novel strategies are introduced to accelerate MLFMA. One of these strategies is to apply parallelization techniques to MLFMA and this parallelization requires a hierarchical partitioning strategy for high efficiency [12, 13]. Alternatively, some preconditioners are used to reduce the number of iterations in MLFMA [14, 15]. Apart from these efforts, conventional MLFMA has still some challenges due to prolonging iterations for large-scale EM scattering problems, especially for volumetric problems, despite the computational complexity of $\mathcal{O}(NlogN)$ [16, 23, 24].

In recent years, machine learning (ML) techniques have become popular in many areas such as medical systems, speech recognition, image processing, etc., to make predictions, classifications, and decisions by learning from the data provided [17, 25]. In general, such systems learn from the available data and perform certain tasks based on examples without being programmed algorithmically. Also, in electromagnetics, ML techniques are recently used in some areas such as antenna design (generally optimization process) [18] and inverse scattering problems [19]. In addition to these applications, initial guesses in iterative solvers are enhanced via some ML techniques [20] and ML techniques are integrated into MLFMA [21, 22].

In this thesis, a novel trimming tree structure strategy in MLFMA, which is previously applied for SIEs [21, 22], is adopted and applied to VIEs. With this strategy, thresholding and ML techniques are performed to eliminate the redundant interactions in MLFMA iterations. In particular, the converged current coefficients are determined via a Fully Connected Neural Network (FCNN) and the tree structure is systematically modified and becomes sparser as the iterations proceed. Due to this sparsification, the convergence is accelerated and matrix-vector multiplication time per iteration is also reduced. As a result, significant speed-up is achieved with a limited and controllable error with respect to the conventional MLFMA.

Different from trimmed MLFMA (T-MLFMA) for SIEs, the interactions are arbitrary in any volume, therefore training of FCNN is completed with only a small size of homogeneous dielectric spheres with different permittivity values. Then, the trained network is used to estimate the current coefficients in the solution of scattering from larger and relatively complex objects. The results with T-MLFMA are presented and discussed in detail and significant speed-up is obtained for various types of homogeneous and inhomogeneous dielectric objects.

The rest of this thesis is organized as follows: In Chapter 2, the basics of electromagnetic theory to constitute volume integral equations are explained in detail. Firstly, the mathematical expressions for fields in terms of electric and magnetic sources are obtained, and then volume integral equations are derived by using the volume equivalence theorem. Next, the resultant volume integral equations are converted into a system of linear equations by using MoM. In Chapter 3, first, the conventional MLFMA is discussed. Then, T-MLFMA is introduced and the trimmed tree structure of T-MLFMA is deeply investigated. Next, the trimming process of coefficients and the details of FCNN are explained. In Chapter 4, the analyses for trimming parameters used in T-MLFMA are presented and performances of T-MLFMA and conventional MLFMA are compared for various dielectric objects.

Throughout this thesis, $e^{-i\omega t}$ notation is used and suppressed, where $\omega = 2\pi f$ is the angular frequency.

Chapter 2

Electromagnetic Theory Background

2.1 Basics of Electromagnetic Theory

Maxwell's equations provide a mathematical model on how electric and magnetic fields physically interact with matter. The time-harmonic form of these equations inside a linear, homogeneous and isotropic medium in frequency domain are given by

$$\nabla \times \mathbf{E}(\mathbf{r}) = i\omega\mu\mathbf{H}(\mathbf{r}) - \mathbf{M}(\mathbf{r}), \tag{2.1}$$

$$\nabla \times \mathbf{H}(\mathbf{r}) = -i\omega\epsilon\mathbf{E}(\mathbf{r}) + \mathbf{J}(\mathbf{r}), \tag{2.2}$$

$$\nabla \cdot \mathbf{E}(\mathbf{r}) = \frac{\rho_e(\mathbf{r})}{\epsilon}, \tag{2.3}$$

$$\nabla \cdot \mathbf{H}(\mathbf{r}) = \frac{\rho_m(\mathbf{r})}{\mu}. \tag{2.4}$$

In (2.1)-(2.4), $\mathbf{E}$ is the electric field intensity, $\mathbf{H}$ is the magnetic field intensity, $\mathbf{J}$ and $\mathbf{M}$ are the electric and magnetic current densities, respectively, whereas ρ_e and ρ_m are the electric and magnetic charge densities, respectively. ϵ and

μ denote the permittivity and permeability of of the medium, respectively, and finally $\mathbf{r}$ stands for the position vector. Note that, $\mathbf{M}$ and ρ_m are fictitious magnetic sources and provide a mathematical and computational symmetry in the equations [26]. Also note that, the relation between current and source densities is expressed via the continuity equations given by

$$\nabla \cdot \mathbf{J}(\mathbf{r}) = i\omega\rho_e(\mathbf{r}), \tag{2.5}$$

$$\nabla \cdot \mathbf{M}(\mathbf{r}) = i\omega\rho_m(\mathbf{r}). \tag{2.6}$$

The vector wave equations for the electric and magnetic fields can be derived from (2.1) to (2.4) by utilizing the continuity equations. Therefore, we obtain simpler expressions for $\mathbf{E}$ and $\mathbf{H}$ fields separately in terms of the sources in the medium. The resultant vector wave equations for $\mathbf{E}$ and $\mathbf{H}$ are given in

$$\nabla^2\mathbf{E}(\mathbf{r}) + k^2\mathbf{E}(\mathbf{r}) = -i\omega\mu\mathbf{J}(\mathbf{r}) + \frac{\nabla\rho_e(\mathbf{r})}{\epsilon} + \nabla \times \mathbf{M}(\mathbf{r}), \tag{2.7}$$

$$\nabla^2\mathbf{H}(\mathbf{r}) + k^2\mathbf{H}(\mathbf{r}) = -i\omega\epsilon\mathbf{M}(\mathbf{r}) + \frac{\nabla\rho_m(\mathbf{r})}{\mu} + \nabla \times \mathbf{J}(\mathbf{r}). \tag{2.8}$$

As an alternative form of Maxwell's equations, $\mathbf{E}$ and $\mathbf{H}$ fields can be written in terms of vector and scalar potentials given by [26]

$$\mathbf{E}(\mathbf{r}) = i\omega\mathbf{A}(\mathbf{r}) - \nabla\phi_e(\mathbf{r}) - \frac{1}{\epsilon}\nabla \times \mathbf{F}(\mathbf{r}), \tag{2.9}$$

$$\mathbf{H}(\mathbf{r}) = i\omega\mathbf{F}(\mathbf{r}) - \nabla\phi_m(\mathbf{r}) - \frac{1}{\mu}\nabla \times \mathbf{A}(\mathbf{r}). \tag{2.10}$$

In (2.9)-(2.10), $\mathbf{F}$ and $\mathbf{A}$ are the electric and magnetic vector potentials, respectively, ϕ_e and ϕ_m are the electric and magnetic scalar potentials, respectively. The vector and scalar potentials are satisfying the wave equations given by [26]

$$\nabla^2\mathbf{F}(\mathbf{r}) + k^2\mathbf{F}(\mathbf{r}) = -\epsilon\mathbf{M}(\mathbf{r}), \tag{2.11}$$

$$\nabla^2 \mathbf{A}(\mathbf{r}) + k^2 \mathbf{A}(\mathbf{r}) = -\mu \mathbf{J}(\mathbf{r}), \tag{2.12}$$

$$\nabla^2 \phi_e(\mathbf{r}) + k^2 \phi_e(\mathbf{r}) = -\frac{\rho_e(\mathbf{r})}{\epsilon}, \tag{2.13}$$

$$\nabla^2 \phi_m(\mathbf{r}) + k^2 \phi_m(\mathbf{r}) = -\frac{\rho_m(\mathbf{r})}{\mu}. \tag{2.14}$$

(2.11)-(2.14) are obtained by imposing the Lorenz gauges that are given by

$$\nabla \cdot \mathbf{A}(\mathbf{r}) = i\omega\epsilon\mu\phi_e(\mathbf{r}), \tag{2.15}$$

$$\nabla \cdot \mathbf{F}(\mathbf{r}) = i\omega\epsilon\mu\phi_m(\mathbf{r}). \tag{2.16}$$

Solutions of (2.11)-(2.14) for $\mathbf{F}$, $\mathbf{A}$, ϕ_e and ϕ_m can be expressed in a general form as

$$\mathbf{F}(\mathbf{r}) = \epsilon \int d\mathbf{r}' \mathbf{M}(\mathbf{r}') g(\mathbf{r}, \mathbf{r}'), \tag{2.17}$$

$$\mathbf{A}(\mathbf{r}) = \mu \int d\mathbf{r}' \mathbf{J}(\mathbf{r}') g(\mathbf{r}, \mathbf{r}'), \tag{2.18}$$

$$\phi_e(\mathbf{r}) = \frac{1}{\epsilon} \int d\mathbf{r}' \rho_e(\mathbf{r}') g(\mathbf{r}, \mathbf{r}'), \tag{2.19}$$

$$\phi_m(\mathbf{r}) = \frac{1}{\mu} \int d\mathbf{r}' \rho_m(\mathbf{r}') g(\mathbf{r}, \mathbf{r}'). \tag{2.20}$$

where $g(\mathbf{r}, \mathbf{r}')$ is the free space Green's function given by

$$g(\mathbf{r}, \mathbf{r}') = \frac{e^{ik|\mathbf{r}-\mathbf{r}'|}}{4\pi|\mathbf{r}-\mathbf{r}'|}. \tag{2.21}$$

In (2.17)-(2.21) $\mathbf{r}'$ denotes the position vector of the source region, whereas $\mathbf{r}$ denotes the position vector of the observation point. Substituting (2.17)-(2.20) into (2.9)-(2.10), we can write $\mathbf{E}$ and $\mathbf{H}$ fields as

$$\mathbf{E}(\mathbf{r}) = ik\sqrt{\frac{\mu}{\epsilon}} \int d\mathbf{r}' \Big(\mathbf{J}(\mathbf{r}') + \frac{1}{k^2} \nabla' \cdot \mathbf{J}(\mathbf{r}') \nabla\Big) g(\mathbf{r}, \mathbf{r}') - \int d\mathbf{r}' \nabla g(\mathbf{r}, \mathbf{r}') \times \mathbf{M}(\mathbf{r}'), \tag{2.22}$$

$$\mathbf{H}(\mathbf{r}) = ik\sqrt{\frac{\epsilon}{\mu}}\int d\mathbf{r}'\Big(\mathbf{M}(\mathbf{r}') + \frac{1}{k^2}\nabla'\cdot\mathbf{M}(\mathbf{r}')\nabla\Big)g(\mathbf{r},\mathbf{r}') + \int d\mathbf{r}'\nabla g(\mathbf{r},\mathbf{r}')\times\mathbf{J}(\mathbf{r}'). \tag{2.23}$$

(2.22)-(2.23) will be utilized to constitute volume integral equations in the following sections.

2.2 The Volume Equivalence Theorem

One can use the volume equivalence theorem to determine the scattered fields when a material object exists in a free-space environment. Consider the sources $\mathbf{J}_i$ and $\mathbf{M}_i$ that radiate into free space and generate $\mathbf{E}_0$, $\mathbf{H}_0$ fields. They satisfy the Maxwell's equations given by

$$\nabla\times\mathbf{E}_0(\mathbf{r}) = -\mathbf{M}_i + i\omega\mu_0\mathbf{H}_0(\mathbf{r}), \tag{2.24}$$

$$\nabla\times\mathbf{H}_0(\mathbf{r}) = \mathbf{J}_i - i\omega\epsilon_0\mathbf{E}_0(\mathbf{r}). \tag{2.25}$$

If we put the same sources into a material medium whose constitutive parameters are $\epsilon(\mathbf{r})$ and $\mu(\mathbf{r})$. They generate fields $\mathbf{E}$, $\mathbf{H}$ that satisfy Maxwell's equations given as

$$\nabla\times\mathbf{E}(\mathbf{r}) = -\mathbf{M}_i + i\omega\mu(\mathbf{r})\mathbf{H}(\mathbf{r}), \tag{2.26}$$

$$\nabla\times\mathbf{H}(\mathbf{r}) = \mathbf{J}_i - i\omega\epsilon(\mathbf{r})\mathbf{E}(\mathbf{r}). \tag{2.27}$$

Subtracting (2.24) from (2.26) and (2.25) from (2.27), we obtain

$$\nabla\times(\mathbf{E}(\mathbf{r}) - \mathbf{E}_0(\mathbf{r})) = i\omega\Big(\mu(\mathbf{r})\mathbf{H}(\mathbf{r}) - \mu_0\mathbf{H}_0(\mathbf{r})\Big), \tag{2.28}$$

$$\nabla\times(\mathbf{H}(\mathbf{r}) - \mathbf{H}_0(\mathbf{r})) = -i\omega\Big(\epsilon(\mathbf{r})\mathbf{E}(\mathbf{r}) - \epsilon_0\mathbf{E}_0(\mathbf{r})\Big). \tag{2.29}$$

The scattered fields $\mathbf{E}_{scat}(\mathbf{r})$ and $\mathbf{H}_{scat}(\mathbf{r})$ can be defined as [26]

$$\mathbf{E}_{scat}(\mathbf{r}) = \mathbf{E}(\mathbf{r}) - \mathbf{E}_0(\mathbf{r}), \tag{2.30}$$

$$\mathbf{H}_{scat}(\mathbf{r}) = \mathbf{H}(\mathbf{r}) - \mathbf{H}_0(\mathbf{r}). \tag{2.31}$$

Using (2.30) and (2.31), (2.28) and (2.29) can be expressed as [26]

$$\begin{aligned} \nabla \times \mathbf{E}_{scat}(\mathbf{r}) &= i\omega\mu(\mathbf{r})\mathbf{H}(\mathbf{r}) - i\omega\mu_0\mathbf{H}_0(\mathbf{r}) + i\omega\mu_0\mathbf{H}_{scat}(\mathbf{r}) \\ &= i\omega\Big(\mu(\mathbf{r})\mathbf{H}(\mathbf{r}) - \mu_0\mathbf{H}_0(\mathbf{r})\Big) + i\omega\mu_0\mathbf{H}_{scat}(\mathbf{r}) \end{aligned} \tag{2.32}$$

and

$$\begin{aligned} \nabla \times \mathbf{H}_{scat}(\mathbf{r}) &= -i\omega\epsilon(\mathbf{r})\mathbf{E}(\mathbf{r}) + i\omega\epsilon_0\mathbf{E}_0(\mathbf{r}) - i\omega\epsilon_0\mathbf{E}_{scat}(\mathbf{r}) \\ &= -i\omega\Big(\epsilon(\mathbf{r})\mathbf{E}(\mathbf{r}) - \epsilon_0\mathbf{E}_0(\mathbf{r})\Big) - i\omega\epsilon_0\mathbf{E}_{scat}(\mathbf{r}). \end{aligned} \tag{2.33}$$

Next, lets define volume equivalent electric current density $\mathbf{J}_{eq}(\mathbf{r})$ and volume equivalent magnetic current density $\mathbf{M}_{eq}(\mathbf{r})$ as [26]

$$\mathbf{J}_{eq}(\mathbf{r}) = -i\omega\Big(\epsilon(\mathbf{r}) - \epsilon_0\Big)\mathbf{E}(\mathbf{r}) = -i\omega\epsilon_0\Big(\epsilon_r(\mathbf{r}) - 1\Big)\mathbf{E}(\mathbf{r}), \tag{2.34}$$

$$\mathbf{M}_{eq}(\mathbf{r}) = -i\omega\Big(\mu(\mathbf{r}) - \mu_0\Big)\mathbf{H}(\mathbf{r}) = -i\omega\mu_0\Big(\mu_r(\mathbf{r}) - 1\Big)\mathbf{H}(\mathbf{r}). \tag{2.35}$$

These equivalent sources exist only inside the material and excite fields into the free space [26] as sketched in Fig. 2.1.

Next, using (2.34) and (2.35), (2.32) and (2.33) can be rewritten as [26]

$$\nabla \times \mathbf{E}_{scat}(\mathbf{r}) = i\omega\mu_0\mathbf{H}_{scat}(\mathbf{r}) - \mathbf{M}_{eq}(\mathbf{r}), \tag{2.36}$$

$$\nabla \times \mathbf{H}_{scat}(\mathbf{r}) = -i\omega\epsilon_0\mathbf{E}_{scat}(\mathbf{r}) + \mathbf{J}_{eq}(\mathbf{r}). \tag{2.37}$$

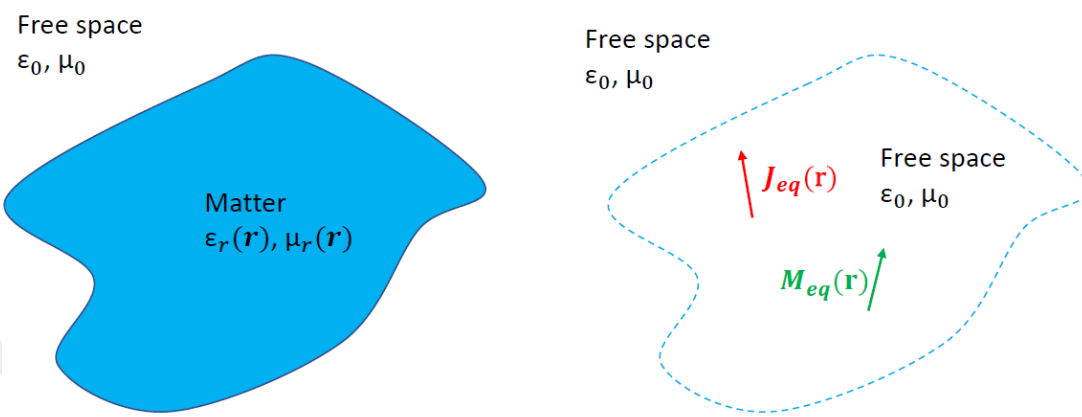

Figure 2.1: The Volume Equivalence Theorem: A dielectric or magnetic material (may be inhomogeneous) is replaced by equivalent sources and free space.

2.3 Volume Integral Equations

In scattering problems, it would be simpler to solve (2.36)-(2.37) if $\mathbf{J}_{eq}$ and $\mathbf{M}_{eq}$ equivalent sources were known. However $\mathbf{J}_{eq}$ and $\mathbf{M}_{eq}$ also depend on $\mathbf{E}$ and $\mathbf{H}$ fields, which are unknown due to the presence of a material object. Therefore, recognizing that solutions of (2.36)-(2.37) (i.e., the scattered fields) that use the equivalent current sources, $\mathbf{J}_{eq}$ and $\mathbf{M}_{eq}$, are given in (2.22) and (2.23), the volume integral equations for the total electric and magnetic fields (incident plus the scattered fields) can be written as

$$\begin{aligned}\mathbf{E}(\mathbf{r}) =& \mathbf{E}_{inc}(\mathbf{r}) + ik\sqrt{\frac{\mu_0}{\epsilon_0}}\int d\mathbf{r}'\mathbf{J}_{eq}(\mathbf{r}')g(\mathbf{r},\mathbf{r}') - \frac{i}{k}\sqrt{\frac{\mu_0}{\epsilon_0}}\nabla\int d\mathbf{r}'\mathbf{J}_{eq}(\mathbf{r}')\cdot\nabla' g(\mathbf{r},\mathbf{r}') \\ &- \int d\mathbf{r}'\nabla g(\mathbf{r},\mathbf{r}')\times\mathbf{M}_{eq}(\mathbf{r}'),\end{aligned} \tag{2.38}$$

$$\begin{aligned}\mathbf{H}(\mathbf{r}) =& \mathbf{H}_{inc}(\mathbf{r}) + ik\sqrt{\frac{\epsilon_0}{\mu_0}}\int d\mathbf{r}'\mathbf{M}_{eq}(\mathbf{r}')g(\mathbf{r},\mathbf{r}') - \frac{i}{k}\sqrt{\frac{\mu_0}{\epsilon_0}}\nabla\int d\mathbf{r}'\mathbf{M}_{eq}(\mathbf{r}')\cdot\nabla' g(\mathbf{r},\mathbf{r}') \\ &+ \int d\mathbf{r}'\nabla g(\mathbf{r},\mathbf{r}')\times\mathbf{J}_{eq}(\mathbf{r}').\end{aligned} \tag{2.39}$$

(2.38) and (2.39) can be solved by expressing the equivalent current sources, $\mathbf{J}_{eq}$ and $\mathbf{M}_{eq}$, in terms of the flux densities $\mathbf{D}$ and $\mathbf{B}$ (called-DB formulation) [27], or in terms of $\mathbf{E}$ and $\mathbf{H}$ fields (called EH-formulation) [28], or a modified version of the EH-formulation called EE- and HH-formulations [28]. In this thesis, we used the DB-formulation as explained in the next subsection.

2.3.1 DB Formulation

Firstly, $\mathbf{J}_{eq}$ and $\mathbf{M}_{eq}$ are replaced with the flux densities $\mathbf{D}$ and $\mathbf{B}$.

$$\mathbf{J}_{eq}(\mathbf{r}) = -i\omega\left(1 - \frac{1}{\epsilon_r(\mathbf{r})}\right)\mathbf{D}(\mathbf{r}), \tag{2.40}$$

$$\mathbf{M}_{eq}(\mathbf{r}) = -i\omega\left(1 - \frac{1}{\mu_r(\mathbf{r})}\right)\mathbf{B}(\mathbf{r}). \tag{2.41}$$

Then, substituting (2.40) and (2.41) into (2.38) and (2.39), and using the constitutive relations between $\mathbf{E}$ and $\mathbf{D}$ and $\mathbf{H}$ and $\mathbf{B}$, one can obtain DB formulations as

$$\begin{aligned}\frac{\mathbf{D}(\mathbf{r})}{\epsilon_r(\mathbf{r})} =& \mathbf{D}_{inc}(\mathbf{r}) + k_0\omega\sqrt{\mu_0\epsilon_0}\int d\mathbf{r}'(1 - \frac{1}{\epsilon_r(\mathbf{r}')})\mathbf{D}(\mathbf{r}')g(\mathbf{r},\mathbf{r}') \\ &- \frac{\omega}{k_0}\sqrt{\mu_0\epsilon_0}\,\nabla\int d\mathbf{r}'(1 - \frac{1}{\epsilon_r(\mathbf{r}')})\mathbf{D}(\mathbf{r}')\cdot\nabla' g(\mathbf{r},\mathbf{r}') \\ &+ i\omega\epsilon_0\int d\mathbf{r}'(1 - \frac{1}{\mu_r(\mathbf{r}')})\nabla g(\mathbf{r},\mathbf{r}')\times\mathbf{B}(\mathbf{r}'),\end{aligned} \tag{2.42}$$

$$\begin{aligned}\frac{\mathbf{B}(\mathbf{r})}{\mu(\mathbf{r})} =& \mathbf{B}_{inc}(\mathbf{r}) + k_0\omega\sqrt{\mu_0\epsilon_0}\int d\mathbf{r}'(1 - \frac{1}{\mu_r(\mathbf{r}')})\mathbf{B}(\mathbf{r}')g(\mathbf{r},\mathbf{r}') \\ &- \frac{\omega}{k_0}\sqrt{\mu_0\epsilon_0}\,\nabla\int d\mathbf{r}'(1 - \frac{1}{\mu_r(\mathbf{r}')})\mathbf{B}(\mathbf{r}')\cdot\nabla' g(\mathbf{r},\mathbf{r}') \\ &- i\omega\mu_0\int d\mathbf{r}'(1 - \frac{1}{\epsilon_r(\mathbf{r}')})\nabla g(\mathbf{r},\mathbf{r}')\times\mathbf{D}(\mathbf{r}').\end{aligned} \tag{2.43}$$

Because we only deal with inhomogenous dielectric objects in this thesis, $\mu_r(\mathbf{r}) = 1$ leading to [29]

$$
\begin{aligned}
\frac{\mathbf{D}(\mathbf{r})}{\epsilon_r(\mathbf{r})} =& \mathbf{D}_{inc}(\mathbf{r}) + k_0^2 \int d\mathbf{r}'(1 - \frac{1}{\epsilon_r(\mathbf{r}')})\mathbf{D}(\mathbf{r}')g(\mathbf{r},\mathbf{r}') \\
& - \nabla \int d\mathbf{r}'(1 - \frac{1}{\epsilon_r(\mathbf{r}')})\mathbf{D}(\mathbf{r}') \cdot \nabla' g(\mathbf{r},\mathbf{r}'),
\end{aligned} \tag{2.44}
$$

$$
\frac{\mathbf{B}(\mathbf{r})}{\mu(\mathbf{r})} = \mathbf{B}_{inc}(\mathbf{r}) - i\omega\mu_0 \int d\mathbf{r}'(1 - \frac{1}{\epsilon_r(\mathbf{r}')})\nabla g(\mathbf{r},\mathbf{r}') \times \mathbf{D}(\mathbf{r}'). \tag{2.45}
$$

However, (2.45) contains two unknowns (D and B) and hence, it is not useful. Hereafter, we proceed with the D-formulation given in (2.44), and solve it using the MoM procedure. It should be noted that because **D** (the electric flux density) is the unknown [27], divergence-conforming basis functions that maintain the continuity of the normal component of **D** at the boundaries should be used in the MoM procedure.

2.4 Method of Moments

MoM is a common technique to solve integral equations in frequency domain by converting them into system of linear equations. In this method, any linear operator $\mathcal{L}\Big\{.\Big\}$ acts on a vector $\mathbf{f}(\mathbf{r})$ and produces an output vector $\mathbf{g}(\mathbf{r})$ given by [5]

$$
\mathcal{L}\Big\{\mathbf{f}(\mathbf{r})\Big\} = \mathbf{g}(\mathbf{r}). \tag{2.46}
$$

The MoM procedure starts by expanding the unknown vector $\mathbf{f}(\mathbf{r})$ as a finite sum of pre-defined linearly independent (divergence conforming in our case) basis functions which satisfy the boundary conditions of electromagnetic fields on the discretized regions. In our problem, the region of object is discretized into tetrahedrons and the electric flux density vector inside the tetrahedrons is expressed in terms of weighted sum of basis functions as

$$\mathbf{f}(\mathbf{r}) \approx \sum_{n=1}^{N} a_n \mathbf{f}_n(\mathbf{r}). \tag{2.47}$$

In (2.47) a_n $n = 1, ..., N$ are the unknown coefficients of the known divergence conforming basis functions to be found at the end of the MoM procedure. By using the linearity of the $\mathcal{L}$ operator, (2.46) can be rewritten as

$$\sum_{n=1}^{N} a_n \mathcal{L}\Big\{\mathbf{f}_n(\mathbf{r})\Big\} \approx \mathbf{g}(\mathbf{r}). \tag{2.48}$$

Equation (2.48) consists of N unknown coefficients. In order to solve this equation, we use another set of N properly chosen testing functions (weighting functions) $\mathbf{w}_m(\mathbf{r})$, $m = 1, ..., N$ to test both sides of it by defining an inner product on each tetrahedron as

$$\langle \mathbf{f}_1(\mathbf{r}), \mathbf{f}_2(\mathbf{r}) \rangle = \int d\mathbf{r} \mathbf{f}_1(\mathbf{r}) \cdot \mathbf{f}_2(\mathbf{r}), \tag{2.49}$$

where the integration is inside the volume of each tetrahedron. Hereafter, by testing both sides of (2.48) we obtain [5]

$$\langle \mathbf{w}_m(\mathbf{r}), \sum_{n=1}^{N} a_n \mathcal{L}\Big\{\mathbf{f}_n(\mathbf{r})\Big\} \rangle \approx \langle \mathbf{w}_m(\mathbf{r}), \mathbf{g}(\mathbf{r}) \rangle, m = 1, ..., N \tag{2.50}$$

and interchanging the order of summation and integration, we obtain

$$\sum_{n=1}^{N} a_n \int d\mathbf{r} \mathbf{w}_m(\mathbf{r}) \cdot \mathcal{L}\Big\{\mathbf{f}_n(\mathbf{r})\Big\} \approx \int d\mathbf{r} \mathbf{w}_m(\mathbf{r}) \cdot \mathbf{g}(\mathbf{r}), m = 1, ..., N. \tag{2.51}$$

Equation (2.51) can be cast into an $N \times N$ matrix equation that can be expressed as

$$\sum_{n=1}^{N} a_n Z_{mn} = v_m, \tag{2.52}$$

where

$$Z_{mn} = \int d\mathbf{r}\mathbf{w}_m(\mathbf{r}) \cdot \mathcal{L}\Big\{\mathbf{f}_n(\mathbf{r})\Big\}, \tag{2.53}$$

and

$$v_m = d\mathbf{r}\mathbf{w}_m(\mathbf{r}) \cdot \mathbf{g}(\mathbf{r}). \tag{2.54}$$

Note that in this thesis, we use Galerkin's scheme, where the weighting functions are chosen to be the same as basis functions. Also note that the matrix equation given in (2.52) can be solved via direct methods or iterative techniques. In both direct and iterative solutions of (2.52), the memory requirement is $\mathcal{O}(N^2)$ for N unknowns (i.e. N basis functions) as the impedance matrix, Z_{mn}, must be stored in the memory. On the other hand, the direct solution of (2.52) requires an $\mathcal{O}(N^3)$ computational complexity, whereas iterative solvers require an $\mathcal{O}(N^2)$ computational complexity for each iteration [5]. Because we are interested to solve the scattering from inhomogenous dielectric objects, the volumetric discreatization requires large number of unknowns (i.e., N becomes very large quickly). Hence, we will solve (2.52) using some acceleration algorithms as will be explained in the upcoming chapters.

2.4.1 SWG Functions

In this thesis, we use DB-formulation as VIE and hence, we use divergence conforming SWG functions in the MoM solution of the resultant VIE. Once dielectric object is modeled by tetrahedral elements, SWG functions are defined for tetrahedron pairs as follows [29]:

A full SWG, as shown in Fig. 2.2 is formed from a pair of tetrahedrons, denoted with T_n^+ and T_n^-, with a triangular common face. In Fig. 2.2, V_n^+ and V_n^- denote the volumes of T_n^+ and T_n^-, respectively, while A_n is the area of the triangular common face. $\mathbf{r}_n^+$ and $\mathbf{r}_n^-$ are defined from origin to the free vertices of T_n^+ and T_n^-, respectively, representing the coordinates of these two vertices (opposite to the

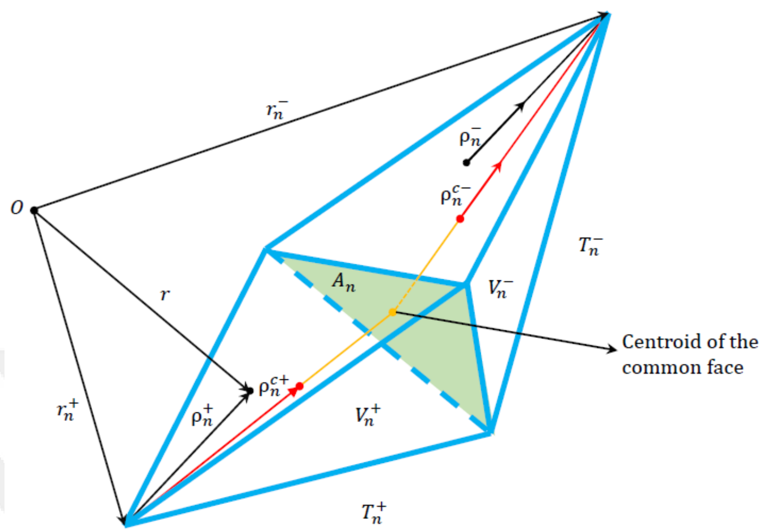

Figure 2.2: SWG Function

triangular common face). ρ_n^{c+} is defined from the vertex of T_n^+ to the centeroid of T_n^+, whereas ρ_n^{c-} is defined from the centeroid of T_n^- to its vertex. Finally, any point inside T_n^+ is shown either by the position vector $\mathbf{r}$ (defined from the origin) or by ρ_n^+ defined from the free vertex of T_n^+. Similarly, any point inside T_n^- is shown either $\mathbf{r}$ or by ρ_n^-, which is defined from the point to the vertex of T_n^-. Consequently, an SWG basis function is mathematically expressed as

$$\mathbf{f}_n(\mathbf{r}) = \begin{cases} \frac{A_n}{3V_n^+}(\mathbf{r} - \mathbf{r}_n^+), & \mathbf{r} \in T_n^+ \\ \frac{A_n}{3V_n^-}(\mathbf{r}_n^- - \mathbf{r}), & \mathbf{r} \in T_n^- \\ 0, & otherwise. \end{cases} \tag{2.55}$$

The following properties of SWG functions are important and useful in expanding the electric flux density $\mathbf{D}(\mathbf{r})$ [29] in terms of them:

(a) Because a tetrahedron is formed from four triangular faces, $\mathbf{D}(\mathbf{r})$ inside a tetrahedron is represented as the vector sum of four linearly independent basis functions, each of which corresponds to one of the faces.

(b) Each SWG, $\mathbf{f}_n(\mathbf{r})$, is tangential to three side faces and is normal to the common face (nth face) of T_n^+ and T_n^-. Morover, it is continuous across this common face and its value $(3V_n^{\pm})/A_n$, which is constant. Therefore, each $\mathbf{f}_n(\mathbf{r})$ has a multiplicative coefficient $A_n/(3V_n^{\pm})$ (see (2.55)) to normalize the value of the flux density to unity on the common face. This property ensures the continuity of the normal $\mathbf{D}$ across the common face of the tetrahedrons.

(c) The charge density of an SWG function, $\mathbf{f}_n(\mathbf{r})$, is given by

$$\nabla.\mathbf{f}_n(\mathbf{r}) = \begin{cases} \frac{A_n}{V_n^+}, & \mathbf{r} \in T_n^+ \\ \frac{-A_n}{V_n^-}, & \mathbf{r} \in T_n^- \\ 0, & o/w \end{cases} \tag{2.56}$$

which is constant within each tetrahedron.

(d) The unknown expansion coefficient a_n (to be determined at the end of the MoM procedure) represents the value of the normal component of $\mathbf{D}$ over the common face (nth face).

(e) The moment of an SWG function $\mathbf{f}_n(\mathbf{r})$ over $T_n^{\pm}$ is given by

$$\int_{T_n^{\pm}} d\mathbf{r}\,\mathbf{f}_n(\mathbf{r}) = \frac{A_n}{3}\rho_n^{c\pm}. \tag{2.57}$$

Finally, in some cases, if a common face of a pair of tetrahedrons is on the boundary, then only one of the tetrahedrons remains inside the volume of interest. In such a scenario, we define and use only half SWG function regarding the interior tetrahedron.

2.4.2 Discretization of VIEs

As mentioned before, in this thesis, we proceed with the D-formulation given in (2.44). On the other hand, we expand $i\omega\mathbf{D}(\mathbf{r})$ by the SWG functions [29] as

$$i\omega\mathbf{D}(\mathbf{r}) = \sum_{n=1}^{N} a_n \mathbf{f}_n(\mathbf{r}). \tag{2.58}$$

Therefore, first (2.44) is arranged as [30]

$$
\begin{aligned}
\mathbf{D}_{inc}(\mathbf{r}) =& \frac{1}{i\omega}\Big(1-\kappa(\mathbf{r})\Big)i\omega\mathbf{D}(\mathbf{r}) + ik_0\sqrt{\mu_0\epsilon_0}\int d\mathbf{r}'\kappa(\mathbf{r}')i\omega\mathbf{D}(\mathbf{r}')g(\mathbf{r},\mathbf{r}') \\
& - i\frac{\sqrt{\mu_0\epsilon_0}}{k_0}\nabla\int d\mathbf{r}'\kappa(\mathbf{r}')i\omega\mathbf{D}(\mathbf{r}')\cdot\nabla' g(\mathbf{r},\mathbf{r}'),
\end{aligned} \tag{2.59}
$$

where $\kappa(\mathbf{r}) = 1 - \frac{1}{\epsilon_r(\mathbf{r})}$.

Then, using the Galerkin's procedure (testing functions are chosen as the same as basis functions), an $N \times N$ dense matrix equation in the form of

$$
\mathbf{Z}\,\mathbf{a} = \mathbf{w} \tag{2.60}
$$

is formed. The elements of Z are given by [30]

$$
\begin{aligned}
\mathbf{Z}[m,n] =& \frac{1}{i\omega}\int_{V_m} d\mathbf{r}(1-\kappa(\mathbf{r}))\mathbf{f}_m(\mathbf{r})\cdot\mathbf{f}_n(\mathbf{r}) \\
& + i\omega\mu_0\epsilon_0\int_{V_m} d\mathbf{r}\mathbf{f}_m(\mathbf{r})\cdot\int_{V_n} d(\mathbf{r}')\kappa(\mathbf{r}')\mathbf{f}_n(\mathbf{r}')g(\mathbf{r},\mathbf{r}') \\
& + \frac{1}{i\omega}\int_{V_m} d\mathbf{r}\mathbf{f}_m(\mathbf{r})\cdot\nabla\int_{V_n} d(\mathbf{r}')\kappa(\mathbf{r}')\mathbf{f}_n(\mathbf{r}')\cdot\nabla' g(\mathbf{r},\mathbf{r}')
\end{aligned} \tag{2.61}
$$

and the elements of $\mathbf{w}$ is given by [30]

$$
\mathbf{w}[m] = \int_{V_m} d\mathbf{r}\mathbf{f}_m(\mathbf{r})\cdot\mathbf{D}^{inc}(\mathbf{r}). \tag{2.62}
$$

Note that in addition to the interactions of between the full SWG functions (basis and testing), there are interactions between full and half SWG functions (full SWG basis function, half SWG testing function or vice versa) as well as interactions between half SWG functions (basis and testing). Therefore, the matrix equation given in (2.60) can be rewritten as

$$\begin{bmatrix} \mathbf{Z}_{FF} & \mathbf{Z}_{FH} \\ \mathbf{Z}_{HF} & \mathbf{Z}_{HH} \end{bmatrix} \begin{bmatrix} \mathbf{a}_F \\ \mathbf{a}_H \end{bmatrix} = \begin{bmatrix} \mathbf{w}_F \\ \mathbf{w}_H \end{bmatrix}. \tag{2.63}$$

As a result, the interaction between the nth SWG basis function $\mathbf{f}_n^{\pm}$ (corresponding to + and - tetrahedrons of the nth face) and the mth testing function $\mathbf{f}_m^{\pm}$ (corresponding to + and $-$ tetrahedrons of the mth face), assuming a constant permittivity within each tetrahedron and using (2.55) and (2.61), can be written as

$$\begin{aligned} \mathbf{Z}[m,n] = \sum_{m\pm}\sum_{n\pm} \Bigg[& \frac{\zeta_{m^\pm,n^\pm}\delta_{m^\pm n^\pm}(1-\kappa_n^\pm)}{i\omega} \int_{V_m^\pm} d\mathbf{r}(\mathbf{r}-\mathbf{r}_m^\pm)\cdot(\mathbf{r}-\mathbf{r}_n^\pm) \\ & + i\omega\mu_0\epsilon_0\zeta_{m^\pm,n^\pm}\kappa_n^\pm \int_{V_m^\pm} d\mathbf{r}(\mathbf{r}-\mathbf{r}_m^\pm)\cdot \int_{V_n^\pm} d\mathbf{r}'(\mathbf{r}'-\mathbf{r}_n^\pm) g(\mathbf{r},\mathbf{r}') \\ & + \frac{\zeta_{m^\pm,n^\pm}\kappa_n^\pm}{i\omega} \int_{V_m^\pm} d\mathbf{r}(\mathbf{r}-\mathbf{r}_m^\pm)\cdot\nabla \int_{V_n^\pm} d\mathbf{r}'(\mathbf{r}'-\mathbf{r}_n^\pm)\nabla' g(\mathbf{r},\mathbf{r}') \Bigg] \end{aligned} \tag{2.64}$$

In (2.64), $\sum\limits_{\pm}$ notation is used to add contributions from both + and $-$ tetrahedrons of full SWG functions (for example; $m+$, $n+$ means the interaction between the + tetrahedron of the $m$the face and + tetrahedron of the nth face; or $m+$, $n-$ means the interaction between the + tetrahedron of the $m$the face and $-$ tetrahedron of the nth face, etc.), $\delta_{m^\pm n^\pm}$ is the Kronecker's delta function, which is 1 only if the testing ans basis tetrahedrons are the same. Furthermore, in (2.64),

$$\zeta_{m^\pm,n^\pm} = \frac{A_m A_n}{9V_m^\pm V_n^\pm}\gamma_m^\pm\gamma_n^\pm \tag{2.65}$$

where $\gamma_m^\pm = \pm 1$ and $\gamma_n^\pm = \pm 1$. Finally, only + tetrahedron (and hence + quantities) must be considered if a half SWG function is considered.

In a similar fashion, the right-hand side (RHS) vector is explicitly given as

$$\mathbf{w}[m] = \sum_{\pm} \frac{\gamma_m^{\pm} A_m}{3V_m^{\pm}} \int_{V_m^{\pm}} d\mathbf{r}(\mathbf{r} - \mathbf{r}_m^{\pm}) \cdot \mathbf{D}^{inc}(\mathbf{r}). \tag{2.66}$$

The last term of (2.64) contains a high-order ($\frac{1}{R^3}, R = |\mathbf{r} - \mathbf{r}'|$) singularity when $\mathbf{r} = \mathbf{r}'$. To reduce it to $\frac{1}{R^2}$ singularity, the vector identity $\mathbf{A} \cdot \nabla'\psi = \nabla' \cdot (\psi\mathbf{A}) - \psi\nabla' \cdot \mathbf{A}$ is used for its third term resulting [31]

$$\begin{aligned}\int_{V_n^{\pm}} d\mathbf{r}'(\mathbf{r}' - \mathbf{r}_n^{\pm}) \cdot \nabla' g(\mathbf{r}, \mathbf{r}') = \int_{V_n^{\pm}} d\mathbf{r}' \nabla' \cdot ((\mathbf{r}' - \mathbf{r}_n^{\pm}) g(\mathbf{r}, \mathbf{r}')) \\ - \int_{V_n^{\pm}} d\mathbf{r}' g(\mathbf{r}, \mathbf{r}') \nabla' \cdot (\mathbf{r}' - \mathbf{r}_n^{\pm}).\end{aligned} \tag{2.67}$$

Regarding the first integral in the right-hand side of (2.67), divergence theorem is used to convert the volume integral into a surface integral over the 4 faces of the tetrahedron (T_n^+ or T_n^-). However, the only contribution will be from the common surface (n^{th} surface), since the basis function has only tangential component on other three surfaces [30]. Additionally, evaluating the divergence of the position vector for the second term in the right-hand side of (2.67), we arrive at

$$\psi(\mathbf{r}) = \int_{V_n^{\pm}} d\mathbf{r}'(\mathbf{r}' - \mathbf{r}_n^{\pm}) \nabla' g(\mathbf{r}, \mathbf{r}') = \frac{3V_n^{\pm}}{A_n} \int_{S_n} d\mathbf{r}' g(\mathbf{r}, \mathbf{r}') - 3 \int_{V_n^{\pm}} d\mathbf{r}' g(\mathbf{r}, \mathbf{r}'). \tag{2.68}$$

Substituting (2.68) in place of the third term in the right-hand side of (2.64) and repeating the above mentioned procedure once again (i.e., using divergence theorem and making use of the properties of SWG functions,), we arrive at

$$\int_{V_m^{\pm}} d\mathbf{r}(\mathbf{r} - \mathbf{r}_m^{\pm}) \cdot \nabla \psi(\mathbf{r}) = \frac{3V_m^{\pm}}{A_m} \int_{S_m} d\mathbf{r} \psi(\mathbf{r}) - 3 \int_{V_m^{\pm}} d\mathbf{r} \psi(\mathbf{r}) \tag{2.69}$$

which replaces the third term in the right-hand side of (2.64) with only a $\frac{1}{R}$ type singularity. Consequently, the final form of the impedance matrix entries with $\frac{1}{R}$ type singularity (when $\mathbf{r} = \mathbf{r}'$) is given by

$$
\begin{aligned}
\mathbf{Z}[m,n] = \sum_{\pm}\sum_{\pm} \Bigg[& \frac{\zeta_{m^\pm,n^\pm}\delta_{m^\pm n^\pm}(1-\kappa_n^\pm)}{i\omega} \int_{V_m^\pm} d\mathbf{r}(\mathbf{r}-\mathbf{r}_m^\pm)\cdot(\mathbf{r}-\mathbf{r}_n^\pm) \\
& + i\omega\mu_0\epsilon_0\zeta_{m^\pm,n^\pm}\kappa_n^\pm \int_{V_m^\pm} d\mathbf{r}(\mathbf{r}-\mathbf{r}_m^\pm)\cdot\int_{V_n^\pm} d\mathbf{r}'(\mathbf{r}'-\mathbf{r}_n^\pm)g(\mathbf{r},\mathbf{r}') \\
& + \frac{9\zeta_{m^\pm,n^\pm}\kappa_n^\pm}{i\omega}\int_{V_m^\pm} d\mathbf{r}\int_{V_n^\pm} d\mathbf{r}' g(\mathbf{r},\mathbf{r}') \\
& - \frac{A_m\gamma_m^\pm\gamma_n^\pm\kappa_n^\pm}{i\omega V_m^\pm}\int_{V_m^\pm} d\mathbf{r}\int_{S_n} d\mathbf{r}' g(\mathbf{r},\mathbf{r}') \\
& - \frac{A_n\gamma_m^\pm\gamma_n^\pm\kappa_n^\pm}{i\omega V_n^\pm}\int_{S_m} d\mathbf{r}\int_{V_n^\pm} d\mathbf{r}' g(\mathbf{r},\mathbf{r}') \\
& + \frac{\gamma_m^\pm\gamma_n^\pm\kappa_n^\pm}{i\omega}\int_{S_m} d\mathbf{r}\int_{S_n} d\mathbf{r}' g(\mathbf{r},\mathbf{r}') \Bigg]
\end{aligned} \tag{2.70}
$$

During the numerical calculations of the integrals, Gaussian quadrature rules with different orders are used. Second-order quadrature is used for basis functions (4 basis points), and first-order quadrature is used for testing functions (1 testing point). These points are the barycentric coordinates [32], which make the volume integrals easier to solve by avoiding the singularity in the tetrahedrons. However, particularly, to increase the accuracy, proper singularity extraction routines [33, 34] are utilized in some geometries as will be specified in the Numerical Results chapter.

Chapter 3

MLFMA and Trimmed MLFMA

3.1 Introduction

As mentioned in the previous chapter, MoM solution of VIEs results in a matrix equation $\mathbf{Z}\,\mathbf{a} = \mathbf{w}$, where $\mathbf{Z}$ is an $N \times N$ dense matrix with N being the number of unknowns. The solution of such a matrix equation requires $\mathcal{O}(N^3)$ computational complexity when direct inversion methods are used. Iterative methods, which are based on matrix-vector-multiplication (MVM), reduce the computational complexity to $\mathcal{O}(N^2)$ for each iteration. Furthermore, the memory requirement is $\mathcal{O}(N^2)$ for both iterative and direct solutions. Unfortunately, electrically large inhomogenous dielectric type volumetric problems that require millions/billions of unknowns cannot be investigated because of such complexity levels. Therefore, as a state-of-the-art computational method MLFMA, which is a hierarchical extension of FMM, reduces both time and memory complexity to $\mathcal{O}(NlogN)$ for N unknowns, and enables us to attack the aforementioned problems. Furthermore, as will be explained later in this chapter, MLFMA is futher accelerated by a progressive elimination of interactions during the iterations (when iterative solvers are used) using artificial neural networks (ANN) and thresholding, referred to as trimmed MLFMA (T-MLFMA), which is previously applied to the solutions of surface integral equations (SIEs) successfully [21, 22].

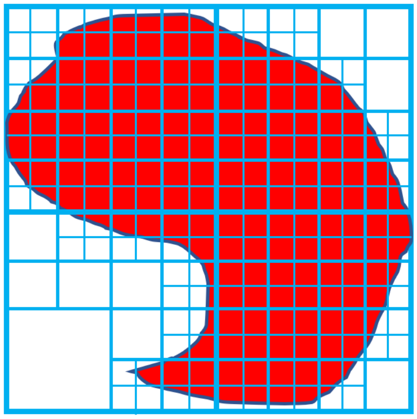

(a) 2D view of clustering of 3D object

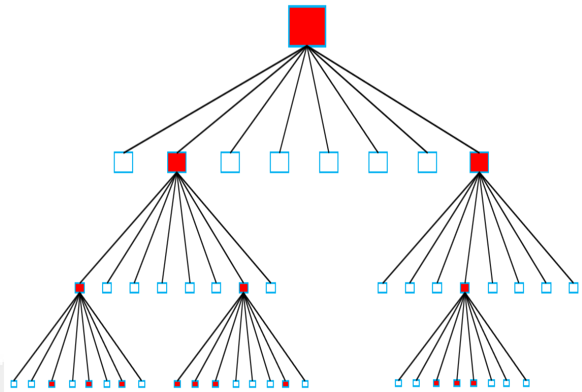

(b) Oct tree structure of boxing scheme

Figure 3.1: Boxing scheme of 3D object

As a result, a significant improvement in the solution time of VIEs is achieved without sacrificing much from the accuracy.

3.2 Multilevel Fast Multipole Algorithm

Any MLFMA implementation starts by constructing a tree structure in order to perform majority of the interaction computations in a group-by-group manner. The object to be analyzed is placed in a cubic box, and is recursively divided into eight identical subboxes by bisecting the box edges (referred to as "clustering"). A 2D view of a clustered 3D object is shown if Fig. 3.1(a). The resultant hierarchy of boxes is called the tree structure (see Fig. 3.1(b)). The recursive division ends when a stopping criterion is met. This criterion is usually the size of the box (its edge length) at the leaf (lowest/deepest) level. In this thesis, the size of the box at the leaf level is decided to be equal or greater than $\lambda/16$. During this step, all empty boxes at any level are omitted.

The next step is the grouping of boxes. Using the one-box-buffer scheme [8] and depending on the distance between the boxes, a box may be a near-zone-box, a far-zone-box or a very-far-zone-box with respect to a given box of interest as shown in Fig. 3.2 (a 2D view). As a result of such grouping, the matrix equation

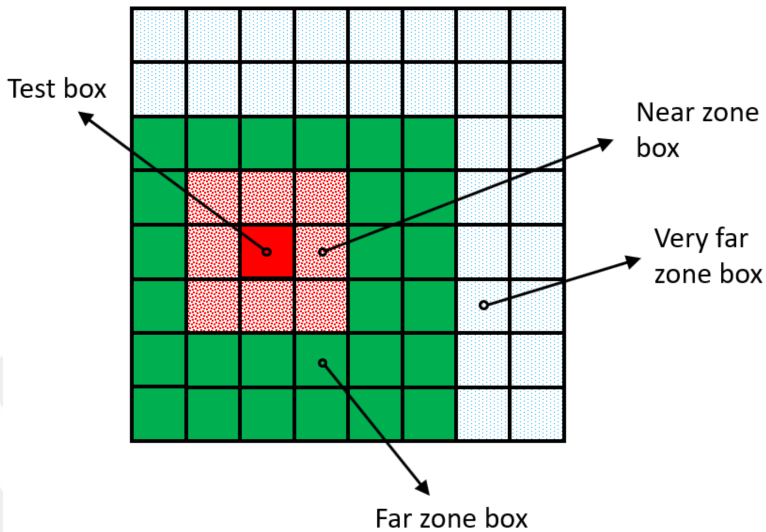

Figure 3.2: 2D view of the one-box-buffer scheme (and grouping of boxes) at the 4^{th} level of MLFMA

$\mathbf{Z}\,\mathbf{a} = \mathbf{w}$ can be decomposed as

$$\mathbf{Z}\,\mathbf{a} = \mathbf{Z}_{near}\,\mathbf{a} + \mathbf{Z}_{far}\,\mathbf{a} = \mathbf{w}, \tag{3.1}$$

where $\mathbf{Z}_{near}$ denotes all the interactions among the near-zone-boxes, whereas $\mathbf{Z}_{far}$ denotes all the interactions among the far-zone (and very-far-zone) boxes. The main contribution comes form the interactions of basis and testing SWG functions that remain in the near-zone-boxes of each other, $\mathbf{Z}_{near}$, as they are calculated directly in an element-by-element fashion, and stored in the memory. However, they constitute a small portion of the total interactions and $\mathbf{Z}_{near}$ is very sparse. Interactions of basis and testing SWG functions of the far-zone boxes, $\mathbf{Z}_{far}$, are computed in a group-by-group manner in each and every level. Finally, basis and testing SWG functions that remain in the very-far-zone boxes (with respect to each other) have indirect interactions among each other that only occur at higher levels (still they are in $\mathbf{Z}_{far}$).

The improvement in the complexity of MLFMA comes from the group-by-group computations of $\mathbf{Z}_{far}$ in each iteration that is performed in three separable stages: Aggregation, translation and disaggregation. Separation of these stages

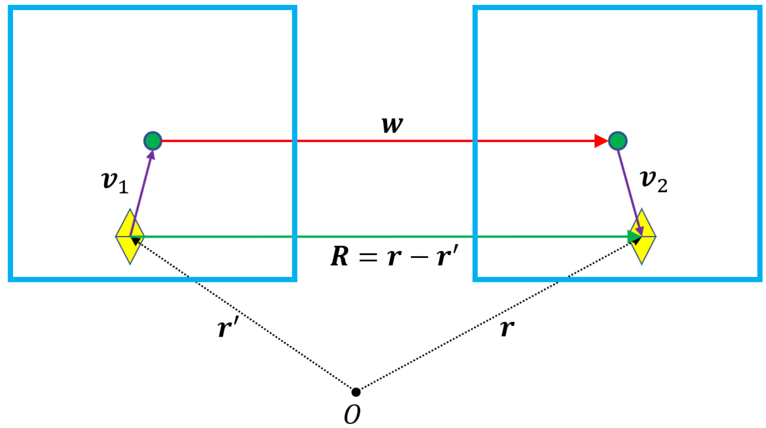

Figure 3.3: Interaction of two SWG functions (illustrated in 2D) located in two far-zone boxes

is achieved by factorizing and diagonalizing the free-space Green's function using Gegenbauer's addition theorem [35]. Consider the interactions of two SWG functions (one basis and one testing) that remain in the far-zone boxes with respect to each other as shown in Fig. 3.3. The free-space Green's function can be expanded in terms of spherical harmonics using Gegenbauer's addition theorem (factorization) as

$$\frac{e^{ik|\mathbf{r}-\mathbf{r}'|}}{4\pi|\mathbf{r}-\mathbf{r}'|} = \frac{e^{ik|\mathbf{w}+\mathbf{v}|}}{4\pi|\mathbf{w}+\mathbf{v}|} = \frac{ik}{4\pi}\sum_{t=0}^{\infty}(-1)^t(2t+1)j_t(kv)h_t^{(1)}(kw)P_t(\hat{w}\cdot\hat{v}), \tag{3.2}$$

where j_t and $h_t^{(1)}$ are spherical Bessel and spherical Hankel functions of the first kind, respectively, with order t, and P_t is the Legendre polynomial of order t, $\mathbf{w}$ is the translation vector with $w = |\mathbf{w}|$, $\mathbf{v} = \mathbf{v_1} + \mathbf{v_2}$ is the shift vector with $v = |\mathbf{v}|$, and $w > v$. Next, the spherical waves can be represented as integral over the plane-wave spectrum as

$$j_t(kv)P_t(\hat{w}\cdot\hat{v}) = \frac{1}{4\pi(i)^t}\int d^2\hat{k}e^{i\mathbf{k}\cdot\mathbf{v}}P_t(\hat{k}\cdot\hat{w}), \tag{3.3}$$

leading to the diagonal form of the Green's function given by

$$\frac{e^{ik|\mathbf{w}+\mathbf{v}|}}{4\pi|\mathbf{w}+\mathbf{v}|} = \frac{ik}{(4\pi)^2}\int d^2\hat{k}e^{i\mathbf{k}\cdot\mathbf{v}}\sum_{t=0}^{\infty}(i)^t(2t+1)h_t^{(1)}(kw)P_t(\hat{k}\cdot\hat{w}). \tag{3.4}$$

In (3.4), $\hat{k}$ represents the unit vector in the radial direction and $d^2\hat{k}$ represents the sampling over the unit sphere. Defining the shift operator as

$$\beta(\mathbf{k},\mathbf{v}) = e^{i\mathbf{k}\cdot\mathbf{v}}, \tag{3.5}$$

the translation operator as

$$T(\mathbf{k},\mathbf{w}) = \sum_{t=0}^{\infty}(i)^t(2t+1)h_t^{(1)}(kw)P_t(\hat{k}\cdot\hat{w}), \tag{3.6}$$

and using $\mathbf{v} = \mathbf{v_1} + \mathbf{v_2}$, (3.4) can be expressed as

$$\frac{e^{ik|\mathbf{w}+\mathbf{v_1}+\mathbf{v_2}|}}{4\pi|\mathbf{w}+\mathbf{v_1}+\mathbf{v_2}|} = \frac{ik}{(4\pi)^2}\int d^2\hat{k}\beta(\mathbf{k},\mathbf{v_1})T(\mathbf{k},\mathbf{w})\beta(\mathbf{k},\mathbf{v_2}). \tag{3.7}$$

The infinite summation in the translation operator, $T(\mathbf{k},\mathbf{w})$, must be truncated at a finite τ value (truncation number) during MLFMA implementations. Hence, the translation operator is approximated as

$$T_\tau(\mathbf{k},\mathbf{w}) \approx \sum_{t=0}^{\tau}(i)^t(2t+1)h_t^{(1)}(kw)P_t(\hat{k}\cdot\hat{w}). \tag{3.8}$$

The τ value is selected via the excess bandwidth formula (EBF) [8] for large translation distances given by

$$\tau \approx 1.73ka + 2.16(d_0)^{2/3}(ka)^{1/3}. \tag{3.9}$$

In (3.9) a is the box size (i.e., box edge length) and d_0 is the desired number of accurate digits [8]. On the other hand, for small box sizes (and hence, for small translation distances), τ can be selected as [37]

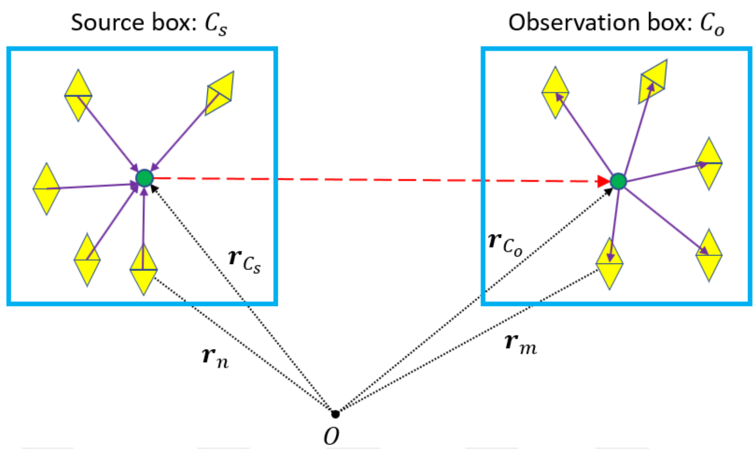

Figure 3.4: Illustration of group-by-group interaction of several basis and testing SWG functions (depicted in 2D) that remain in two far-zone boxes (source box C_s and observation box C_o)

$$\tau \approx 14.14(d_0) - 7.17. \tag{3.10}$$

Also note that τ is defined for each level and it not only affects the accuracy of the translation operator but also determines the number of sampling points along θ and ϕ for the integration in (3.7).

Now at this point, let's consider two boxes that are in the far-zone of each other. Each box contains several SWG functions (source box C_s contains SWG basis functions and observation box C_o contains SWG testing functions) as depicted in Fig. 3.4, where $\mathbf{r}_{C_s}$ and $\mathbf{r}_{C_o}$ are the centers of the source C_s and observation C_o boxes, respectively.

Assume each SWG as a point source and $\mathbf{r}_n$ denotes the position vector of the n^{th} source (source point: centroid of the common face of the n^{th} SWG basis function) in C_s (n=1,...,N_{C_s}). Similarly, $\mathbf{r}_m$ denotes the position vector of the m^{th} testing function (observation point) in C_o. Using (3.7), the Green's function due to the n^{th} source point (located at $\mathbf{r}_n$) in C_s at the observation point $\mathbf{r}_m$ in C_o is written as

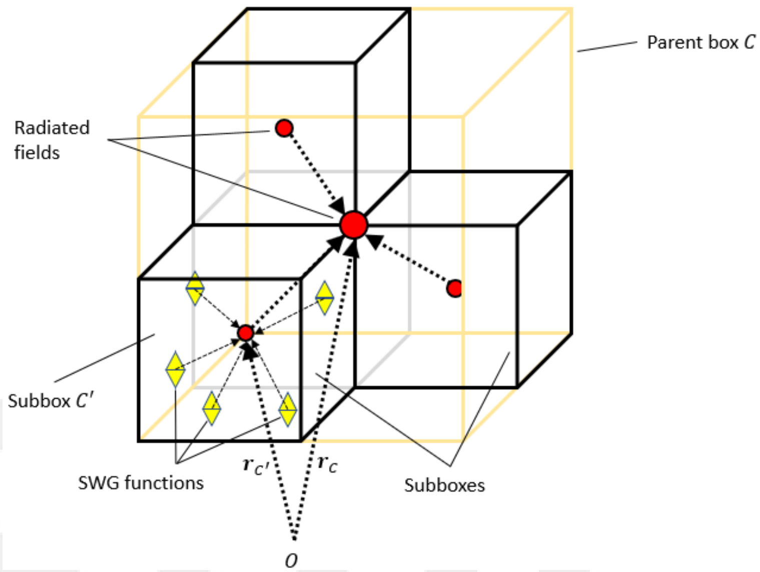

Figure 3.5: Aggregation in the leaf and a higher levels

$$\frac{e^{ik|\mathbf{r}_m-\mathbf{r}_n|}}{4\pi|\mathbf{r}_m-\mathbf{r}_n|}=\frac{ik}{(4\pi)^2}\int d^2\hat{k}\beta_S(\mathbf{k},\mathbf{r}_{C_s}-\mathbf{r}_n)T_\tau(\mathbf{k},\mathbf{r}_{C_o}-\mathbf{r}_{C_s})\beta_R(\mathbf{k},\mathbf{r}_m-\mathbf{r}_{C_o}), \quad (3.11)$$

where $\beta_S(\mathbf{k},\mathbf{r}_{C_s}-\mathbf{r}_n)$ and $\beta_R(\mathbf{k},\mathbf{r}_m-\mathbf{r}_{C_o})$ are the shift operators at the source box C_s and the observation box C_o, respectively. As can be seen from (3.11), a change in the position of source and/or observation points only change the shift operators while the translation operator stays intact. Hence, the field due to N_{C_s} sources in C_s can be written at the observation point $\mathbf{r}_m$ as

$$\sum_{n=1}^{N_{C_s}}\frac{e^{ik|\mathbf{r}_m-\mathbf{r}_n|}}{4\pi|\mathbf{r}_m-\mathbf{r}_n|}=\frac{ik}{(4\pi)^2}\int d^2\hat{k}\beta_R(\mathbf{k},\mathbf{r}_m-\mathbf{r}_{C_o})T_\tau(\mathbf{k},\mathbf{r}_{C_o}-\mathbf{r}_{C_s})\sum_{n=1}^{N_{C_s}}\beta_S(\mathbf{k},\mathbf{r}_{C_s}-\mathbf{r}_n), \quad (3.12)$$

which enables the group-by-group computations for the far-zone interactions.

Finally, let's briefly explain the three stages of MLFMA: Aggregation, translation and disaggregation.

Aggregation: In this stage, the radiated fields for each box at every level are computed in a recursive manner from the leaf level to the highest level (mother level). In the leaf level, the radiation pattern of each SWG basis function is multiplied with the corresponding element of the coefficient vector $a[n]$, and aggregated into the center of the subbox C' as depicted in Fig. 3.5. As a result, the field at the center of a leaf-level box can be expressed as

$$\mathbf{S}_{C'}(\mathbf{k}, \mathbf{r}_{C'}) = \sum_{b_n \in C'} a[n] \beta_S(\mathbf{k}, \mathbf{r}_{C'} - \mathbf{r}_n) \mathbf{S}_n(\mathbf{k}, \mathbf{r}_n), \tag{3.13}$$

where $\mathbf{r}_{C'}$ is the position vector for the center of the box C', and $\mathbf{S}_n(\mathbf{k}, \mathbf{r}_n)$ is the radiation pattern of the n^{th} SWG function positioned at $\mathbf{r}_n$. At higher levels, the radiation pattern at the center of each child box (subbox) C' is multiplied by a shift function, and aggregated into the center of the parent box C (see Fig. 3.5). The final field expression at the center of the parent box C is written as

$$\mathbf{S}_C(\mathbf{k}, \mathbf{r}_C) = \sum_{C' \in C} \beta_S(\mathbf{k}, \mathbf{r}_C - \mathbf{r}_{C'}) \mathbf{S}_{C'}(\mathbf{k}, \mathbf{r}_{C'}), \tag{3.14}$$

where $\mathbf{S}_{C'}(\mathbf{k}, \mathbf{r}_{C'})$ is the radiation pattern of the child box C' centered at $\mathbf{r}_{C'}$. Note that, because the truncation number may differ (increase) due to the change (increase) of the box size at different (higher) levels, we may need different (more) number of θ and ϕ samples in (3.12). Hence, interpolation might be necessary [8].

Translation: After the aggregation stage, computed aggregated fields are translated to boxes with available far-zone interactions, denoted as $F\{C\}$. Hence, the receiving pattern (translated field) at the center of a box C (positioned at $\mathbf{r}_C$) is given by

$$\mathbf{G}_C(\mathbf{k}, \mathbf{r}_C) = \sum_{C' \in F\{C\}} T_\tau(\mathbf{k}, \mathbf{r}_C - \mathbf{r}_{C'}) \mathbf{S}_{C'}(\mathbf{k}, \mathbf{r}_{C'}) \tag{3.15}$$

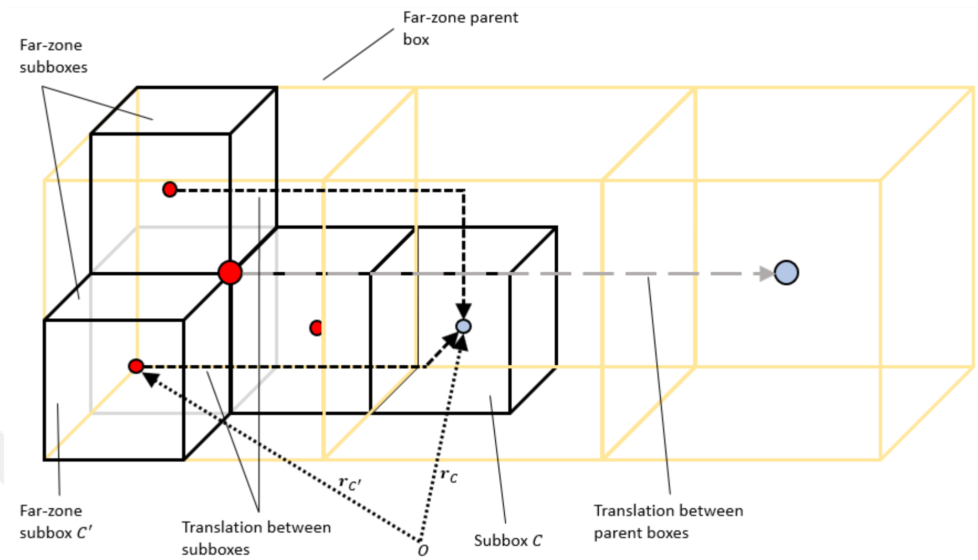

Figure 3.6: Translation at two different levels

Note that the translation stage is done for each level of MLFMA, as illustrated in Fig. 3.6.

<u>Disaggregation</u>: Once the translated fields, $\mathbf{G}_C(\mathbf{k}, \mathbf{r}_C)$ are computed, they are distributed to the lower level boxes by disaggregation as depicted in Fig. 3.7. Basically, a disaggregated field from the center of the parent box to the center of a child box is added to the field conveyed via translation from the far-zone boxes at the level of the child box. Hence, the disaggregated field, $\mathbf{G}^+_{C'}(\mathbf{k}, \mathbf{r}_{C'})$, at the center of the child box $\mathbf{r}_{C'}$, can be expressed as

$$\mathbf{G}^+_{C'}(\mathbf{k}, \mathbf{r}_{C'}) = \mathbf{G}_{C'}(\mathbf{k}, \mathbf{r}_{C'}) + \beta_R(\mathbf{k}, \mathbf{r}_{C'} - \mathbf{r}_C)\mathbf{G}^+_C(\mathbf{k}, \mathbf{r}_C) \qquad C' \in C. \tag{3.16}$$

In (3.16), $\mathbf{G}_{C'}(\mathbf{k}, \mathbf{r}_{C'})$ is the receiving field of the child box due to the translation from the far-zone boxes (at the same level), and $\mathbf{G}^+_C(\mathbf{k}, \mathbf{r}_C)$ is the disaggregated field at the center of the parent box C, centered at $\mathbf{r}_C$. This process is continued until we arrive to the leaf level, where receiving fields of boxes $\mathbf{G}^+_{C'}$ are distributed to the SWG functions by performing a dot product with the radiation pattern of the m^{th} SWG function, $\mathbf{F}_m(\mathbf{k}, \mathbf{r}_m)$ $m = 1, ..., N$ and integrating over the radiation sphere. Also note that, the truncation number may again differ at lower levels,

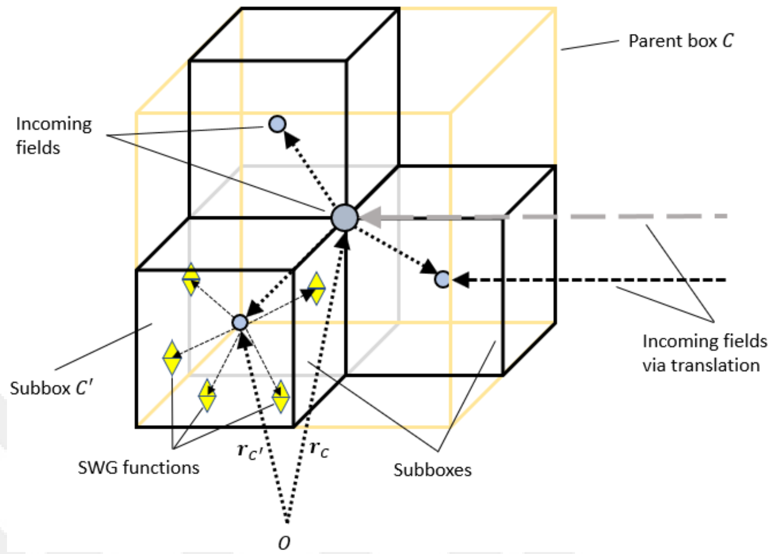

Figure 3.7: Disaggregation in the leaf and a higher level

and hence we may need different (less) number of θ and ϕ samples in (3.12). Hence, anterpolation [8] might be necessary. Consequently, the m^{th} element of MVM is give by

$$\sum_{n=1}^{N} Z_{far}[m,n]a[n] = \left(\frac{ik}{4\pi}\right)^2 \int d^2\hat{k}\mathbf{F}_m(\mathbf{k},\mathbf{r}_m)\cdot\beta_R(\mathbf{k},\mathbf{r}_m-\mathbf{r}_C)\mathbf{G}_C^{+}(\mathbf{k},\mathbf{r}_C). \quad (3.17)$$

The resulting MVM is used at each iteration of the iterative solver, where we use the flexible generalized minimal residual (F-GMRES) method [38], and iterations are terminated when a predefined residual error is achieved.

3.3 Trimmed MLFMA

MLFMA, explained in the previous section, is accelerated by a progressive elimination of interactions during the iterations as will be explained in this section. Such an elimination of interactions results in trimmed tree structures [21, 22], and hence the method is called trimmed MLFMA (T-MLFMA).

Consider the matrix equation in (3.1), the solution for vector **a** can be constructed by using the Krylov subspace vectors which are given in

$$\mathcal{K}_r(\mathbf{Z}, \mathbf{w}) = span\{\mathbf{w}, \mathbf{Z}\,\mathbf{w}, \mathbf{Z}^2\,\mathbf{w}, ..., \mathbf{Z}^{r-1}\,\mathbf{w}\}, \tag{3.18}$$

where r is the order of the subspace and can have smaller values up to N. The order r increases as the iterations continue in the iterative solver. In general, as the number of Krylov subspace vectors increases, the error of the solution decreases. However, the contribution to the solution coming from Krylov subspace vectors decreases as the iterations proceed and most of the subspace vectors converge after some iterations [21]. As a result, we obtain negligible variations in some elements of the calculated **w** and updated **a** after a certain iteration (say i), and these elements can be eliminated in the far-zone interaction computations for the next iterations $(i+1, i+2, ...)$. To illustrate this behaviour, a sample problem is investigated where a homogenous dielectric sphere of radius 300 mm with relative dielectric permittivity $\epsilon_r = 4$ is illuminated by a uniform plane wave at 0.3 GHz. MoM is employed to solve the resultant VIE, where the dielectric sphere is discretized with $\lambda/20$ edge length tetrahedrons leading to 7190 SWG functions, and the unknown coefficient vector **a** is obtained iteratively. Next, we calculate the normalized error between $\mathbf{w}_i$ and the actual **w** for each element of the right-hand side (RHS) vector **w** at each iteration as

$${e_i}^w[n] = log_{10}\frac{|w_i[n] - w[n]|}{|w[n]|}, \tag{3.19}$$

where $w[n]$ is the actual value for the n^{th} element of **w**, whereas $w_i[n]$ is its value at the i^{th} iteration. Similarly, the normalized error between $\mathbf{a}_i$ and the resultant **a** for each element of the coefficient vector **a** at each iteration is calculated as

$${e_i}^a[n] = log_{10}\frac{|a_i[n] - a[n]|}{|a[n]|}, \tag{3.20}$$

where $a[n]$ is the final value for the n^{th} element (solved value) of **a**, whereas $a_i[n]$ is

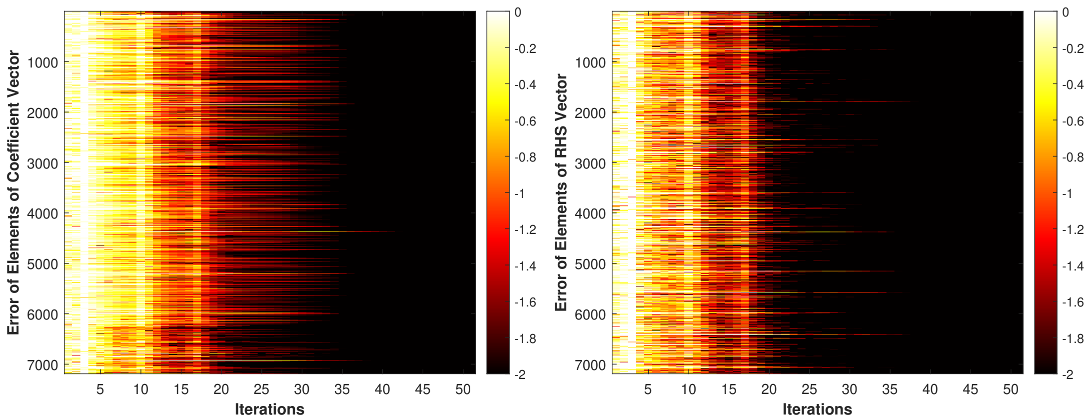

(a) (b)

Figure 3.8: Error between (a) the final $\mathbf{a}$ and the calculated $\mathbf{a}_i$ at each iteration; (b) the actual $\mathbf{w}$ and the calculated $\mathbf{w}_i$ at each iteration for a homogeneous dielectric sphere of radius 300 mm with $\epsilon = 4$ illuminated by a uniform plane wave at 0.3 GHz

its value at the i^{th} iteration. These errors versus number of iterations are plotted in Fig. 3.8. As can be seen from Fig. 3.8(a), the variation in ${e_i}^a[n]$ is (n=1, ..., 7190) is negligible for most of the elements after $i = 25$ iterations. Similarly, the variation in ${e_i}^w[n]$ is also negligible after $i = 20$ iterations as observed in Fig. 3.8(b).

Therefore, after a number of iterations, the interactions of the converged elements ($a_i[n]$ and $w_i[n]$) can be omitted, because they contribute significantly less, which leads to a trimming in the tree structure yielding a reduction in the number of operations in each MVM as follows: Let's rewrite (3.1) as

$$\left[\mathbf{Z}_{near}\right] \cdot \begin{bmatrix} a_1 \\ . \\ . \\ a_p \\ . \\ . \\ a_N \end{bmatrix} + \begin{bmatrix} Z_{11} & . & . & Z_{1p} & . & . & Z_{1N} \\ . & . & . & . & . & . & . \\ . & . & . & . & . & . & . \\ Z_{m1} & . & . & Z_{mp} & . & . & Z_{mN} \\ . & . & . & . & . & . & . \\ . & . & . & . & . & . & . \\ Z_{N1} & . & . & Z_{Np} & . & . & Z_{NN} \end{bmatrix} \cdot \begin{bmatrix} a_1 \\ . \\ . \\ a_p \\ . \\ . \\ a_N \end{bmatrix} = \begin{bmatrix} w_1 \\ . \\ . \\ w_m \\ . \\ . \\ w_N \end{bmatrix}, \quad (3.21)$$

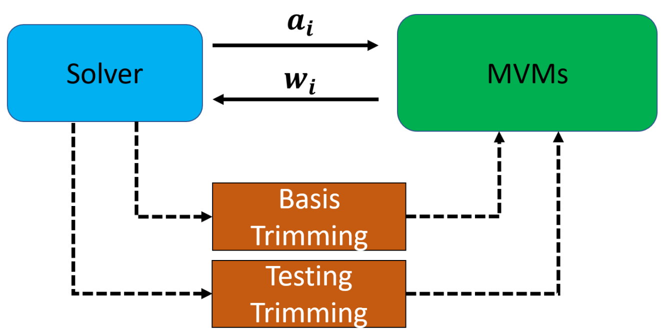

Figure 3.9: Iterative solution scheme in T-MLFMA

and assume that a_p and w_m are the converged elements of $\mathbf{a}$ and $\mathbf{w}$, shown in green and red colors, respectively. Because a_p is converged, there is no need to make calculations with the p^{th} column (highlighted with green box) of $\mathbf{Z}_{far}$. In a similar fashion, because w_m is converged, there is no need to make calculation with the m^{th} row (highlighted with the red box) of $\mathbf{Z}_{far}$. Deleting this row and column in MVMs in MLFMA for the next iterations, the conventional tree structure is trimmed (trimming scheme is explained in the next section), and the number of operations decrease in $\mathbf{Z}_{far}\,\mathbf{a}$ calculations. On the other hand, because the sparse $\mathbf{Z}_{near}$ is calculated before the iterations and stored in the memory, its trimming does not provide any significant reduction in the MVM time. Hence, trimming is not implemented to $\mathbf{Z}_{near}$ and it stays intact [21, 22].

The trimming of the converged elements of $\mathbf{w}$ is called the testing function trimming (briefly testing trimming) and the trimming of the converged elements of $\mathbf{a}$ is called the basis function trimming (briefly basis trimming). Testing and basis function trimmings are processed separately at each iteration as illustrated in Fig. 3.9, which shows the workflow of iterative solutions. Basically, the solver produces the coefficient vector $\mathbf{a}_i$ by taking $\mathbf{w}_i$ as an input at iteration i (shown in solid lines) separately. Regarding the testing trimming process, we exploit a simple comparison of calculated $\mathbf{w}_i$ at the i^{th} iteration with the actual $\mathbf{w}$ to trim testing functions. However, regarding the basis trimming process, we employ ML techniques to predict which elements of $\mathbf{a}$ can be omitted as the final solution of $\mathbf{a}$ is not known.

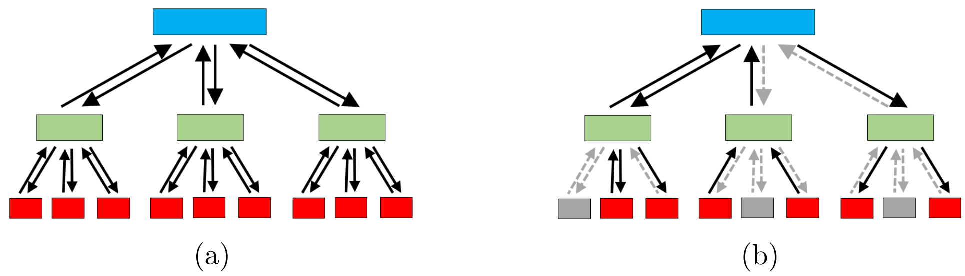

Figure 3.10: Regular (a) and jointly (b) trimmed tree structure for aggregation and disaggregation stages

3.3.1 Trimming Scheme on MLFMA

In regular MLFMA, all stages (aggregation, disaggregation, and translation) share the same tree structure at each iteration as depicted in Fig. 3.10(a) where the aggregation and disaggregation of fields between boxes at different levels are shown in solid black arrows. Because all boxes are included in calculations, the MVMs in all these stages are performed in the same manner and computation time for MVMs are constant at each and every iteration. On the other hand, explained in the previous section, some converged interactions give opportunity to omit some portions of $\mathbf{Z}_{far}$ after some iterations. However, this trimming process should be considered carefully, since the tree structure of MLFMA changes significantly and all stages are affected notably. Basically, as explained in [21, 22], we need to consider the followings: (a) The convergence behaviour of basis and testing trimmings is different, which leads to different tree structures for aggregation and disaggregation. Note that basis trimming affects the aggregation while the testing trimming affects the disaggregation. (b) Once started, trimming must propagate to all branches of the tree. Otherwise we cannot obtain maximum efficiency. (c) The trimming process should be cumulative based on the evolution of the tree structure at each iteration.

Fig. 3.10(b) shows the tree structure (both for aggregation and disaggregation) when the trimming is applied to both aggregation and disaggregation. In this figure, if any box is trimmed from both aggregation and disaggregation, that box is depicted in gray color, and trimmed aggregated and disaggregated fields are shown in gray dashed arrows. As can be noticed from this figure (see also Fig.

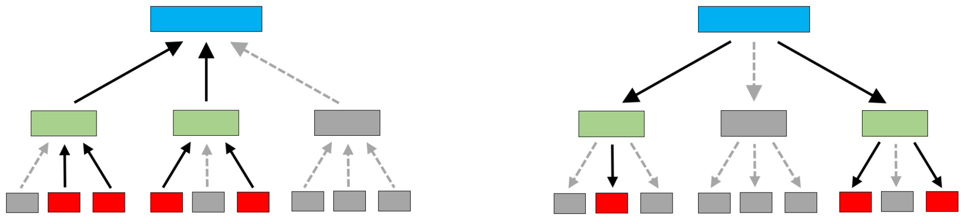

(a) (b)

Figure 3.11: Trimmed (a) aggregation and (b) disaggregation tree structures

3.11(a) for aggregation and Fig. 3.11(b) for disaggregation), the tree structure that is employed for aggregation differs from that for disaggregation. For instance, a box can be omitted from aggregation, but it is not necessarily trimmed in disaggregation and vice versa. Algorithm 1 describes the box trimming algorithm in aggregation due to basis function trimming.

Algorithm 1 Box Trimming Algorithm in Aggregation due to Basis Function Trimming

```
procedure AT EACH ITERATION
    for Box=1:B do
        if all basis functions in the Box are excluded then
            exclude the Box from aggregation and translation
        end if
    end for
end procedure
```

First of all, if all basis functions are trimmed in a box, there will be no radiated field in the center of the box, and aggregation of the zero-field to the parent box becomes redundant and the box is trimmed from aggregation calculations as illustrated in Fig. 3.11(a). Second of all, the translation of this field to far zone boxes does not contribute the solution and becomes unnecessary as indicated in Fig. 3.12(a). In Fig. 3.12(a), trimmed boxes in aggregation are shown in grey color, despite included boxes in aggregation are shown in green color. The translation of fields due to included boxes are shown in solid yellow arrows, and redundant translation of fields due to the omitted boxes from aggregation are shown in dashed grey arrows. The same procedure is adopted at higher levels. Finally, if a basis function is trimmed solely, the radiation of this basis function to the center of the box at the lowest level becomes redundant.

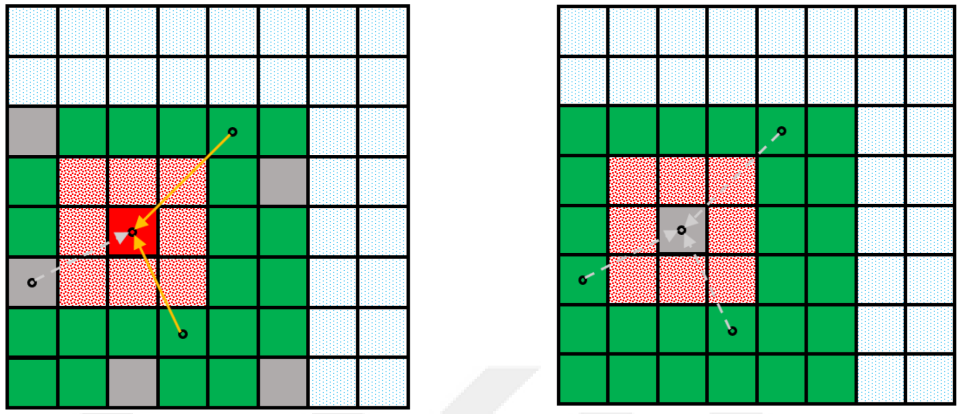

(a) (b)

Figure 3.12: Box trimming in translation (a) basis box, (b) testing box

Similarly, Algorithm 2 describes the box trimming algorithm in disaggregation due to testing function trimming. First of all, if all testing functions are trimmed in a box, it will be redundant to disaggregate any field to that box from the parent box and the box is trimmed from disaggregation calculations as illustrated in Fig. 3.11(b). Second of all, translation to the trimmed box from all far zone boxes becomes unnecessary as depicted in Fig. 3.12(b). In Fig. 3.12(b), the trimmed box in disaggregation is depicted in gray color and redundant translation of fields to the omitted box from disaggregation are shown in dashed gray arrows. Finally, if a testing function is trimmed solely, there is no need to receive any field to this testing function from the box center at the lowest level.

Algorithm 2 Box Trimming Algorithm in Disaggregation due to Testing Function Trimming

```
procedure AT EACH ITERATION
    for Box=1:B do
        if all testing functions in the Box are excluded then
            exclude the Box from translation and disaggregation
        end if
    end for
end procedure
```

In the following subsections, we explain in detail how the testing and basis function trimmings are performed.

3.3.1.1 Testing Function Trimming

To determine the converged elements of the right-hand-side vector $\mathbf{w}$ and trim the testing functions, a straightforward comparison is performed between the calculated $\mathbf{w}_i$ at each iteration and the actual $\mathbf{w}$.

Algorithm 3 Testing Function Trimming Algorithm

procedure AT EACH ITERATION
    for `m=1:N` **do**
        $e_i^w = \frac{|w_i[m]-w_{actual}[m]|}{|w_{actual}[m]|}$
        if $e_i^w \leq$Testing Trimming Error Threshold **then**
            Counter[m] = Counter[m]+1
        else
            Counter[m] = 0
        end if
        if Counter[m] = Testing Trimming Count **then**
            exclude the testing function f_m
        else
            store the Counter for the next iteration
        end if
    end for
end procedure

Algorithm 3 presents the steps of the testing trimming algorithm at each iteration. As the first step, an error is calculated for each element of $\mathbf{w}_i$ at each iteration given by

$$e_i^w[m] = \frac{|w_i[m] - w_{actual}[m]|}{|w_{actual}[m]|}, \tag{3.22}$$

where m is the index of the element, $\mathbf{w}_{actual}$ is the actual right-hand-side vector and $\mathbf{w}_i$ is the latest calculated right-hand-side vector. Next, this error is compared with a predetermined Testing Trimming Error Threshold (TTET) value. To avoid the undesired trimming of not fully converged interactions, we wait until the error is below the TTET value Testing Trimming Counter (TTC) (let's say this value is 3 or 5) times in a row. If the error $e_i^w[m]$ is TTC times below the TTET value, we assume the convergence of this testing function $w[m]$ is ensured, and $w[m]$ is trimmed (i.e., removed from the MLFMA calculations) for the next iterations, and the disaggregation tree is updated starting from the bottom level.

3.3.1.2 Basis Function Trimming

To determine the converged elements of the coefficient vector **a** and trim the basis functions, a simple comparison as done with **w** is not sufficient because the actual coefficient vector **a** is not available in the solver. Therefore, an estimation is made using a Fully-connected neural network (ML technique) based on the coefficient vector results that are obtained in previous iterations. The estimation process and the details of the fully-connected neural network are provided in detail in the next subsection.

Algorithm 4 Basis Function Trimming Algorithm

procedure AT EACH ITERATION
    for `n=1:N` **do**
        $a_{estimated}[n] = ECV(a_{i-1}[n], a_{i-2}[n], a_{i-3}[n])$

        $e_i^a = \frac{|a_i[n]-a_{estimated}[n]|}{|a_{estimated}[n]|}$

        if $e_i^a \leq$ Basis Trimming Error Threshold **then**
            Counter[n] = Counter[n]+1
        else
            Counter[n] = 0
        end if
        if Counter[n] = Basis Trimming Count **then**
            exclude the basis function f_n
        else
            store the Counter for the next iteration
        end if
    end for
end procedure

Algorithm 4 presents the steps of the basis function trimming algorithm at each iteration. As the first step, the Estimate Coefficient Vector (ECV) function takes the latest (usually the last 3 iterations $i-1$, $i-2$, $i-3$ before the current iteration

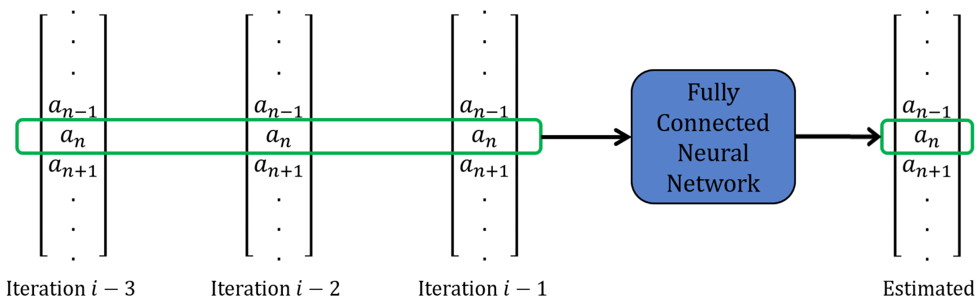

Figure 3.13: Coefficient vector estimation via Fully-Connected Neural Network

i) 3 coefficient vectors as input and calculates the estimation for each element of $\mathbf{a}$ as shown in Fig. 3.13. Then, an error is calculated for each element of $\mathbf{a}_i$ at each iteration given by

$$e_i^a[n] = \frac{|a_i[n] - a_{estimated}[n]|}{|a_{estimated}[n]|}, \tag{3.23}$$

where n is the index of the coefficient vector element, $\mathbf{a}_{estimated}$ is the estimated coefficient vector and $\mathbf{a}_i$ is the latest calculated coefficient vector. As the next step, this error is compared with a predetermined Basis Trimming Error Threshold (BTET) value. Similar to the testing function trimming, to avoid the undesired trimming of not fully converged interactions, we wait until the error is below the BTET value Basis Trimming Counter (BTC) (let's say this value is 3 or 5) times in a row. If the error $e_i^a[n]$ is BTC times below the BTET value, we assume the convergence of this basis function $a[n]$ is ensured, and $a[n]$ is trimmed (i.e., removed from the MLFMA calculations) for the next iterations, and the aggregation tree is updated starting from the bottom level.

As will be mentioned in the Numerical Results chapter, several analyzes are performed to determine the values of TTET, TTC, BTET and BTC. Therefore, the performance of T-MLFMA (e.g., far-field error with respect to the conventional MLFMA, total MVMs time, etc.) is compared for different values of these threshold and counter values.

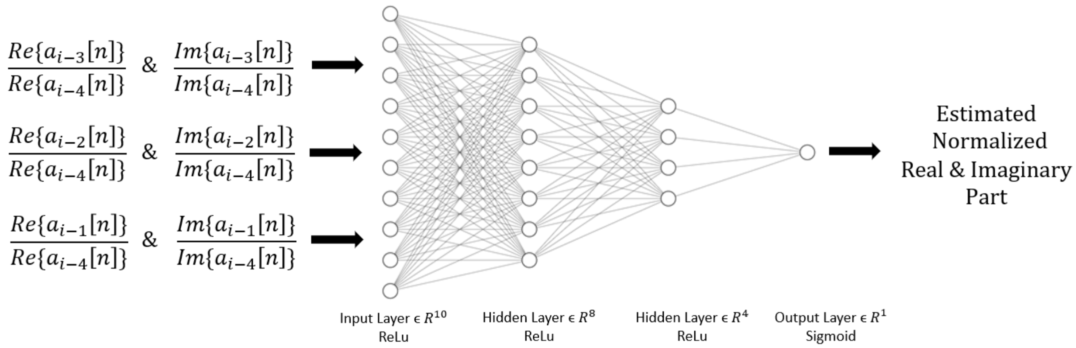

Figure 3.14: Estimation of real and imaginary parts of coefficient vector via FCNN

3.3.1.3 Fully-Connected Neural Network

A four-layer fully-connected neural network (FCNN) is constructed similar to the one in [21, 22] to estimate $\mathbf{a}$ (i.e., $\mathbf{a}_{estimated}$ in Algorithm 4) for the aforementioned basis function trimming. The first (input) layer has 10 neurons, the second and third layers have 8 and 4 neurons, respectively, and finally the fourth (output) layer has 1 neuron. Besides, the first, second and the third layers use rectified linear unit (ReLU) activation function, whereas the last layer uses the Sigmoid activation function.

The inputs of this FCNN at iteration i are the real and imaginary parts of the normalized coefficient vector elements coming from the previous 3 iterations (i.e., i-3, i-2, i-1). The normalization is performed with respect to the real and imaginary parts of the coefficient vector element obtained at $(i-4)^{th}$ iteration as illustrated in Fig. 3.14.

Regarding the data set, $\lambda/4$ homogeneous dielectric spheres with different ϵ_r values ($\epsilon_r = 1.5, 2, 3, 4, 6, 8, 10, 15, 20$ and 25) are considered. The objects are discretized with 71,466 SWG functions and illuminated by linearly polarized plane waves, and coefficient vectors at each iteration are saved. Desired residual error in the solutions are 10^{-4} and results at all iterations are used in the training without omitting any sample. After that, the FCNN is trained via Adam optimizer using mean-absolute-error (MAE) loss function for 500 epochs [39]. The training takes approximately 1 hour on AMD Ryzen 7 PRO 2700 Eight-Core Processor CPUs. We believe that the training with such a small size full spheres is sufficient to estimate the current coefficients for larger and more complex geometries, since, unlike the interactions of RWGs, the interactions of SWG functions are random in any volume, and the SWGs have many different directions yielding various interactions in a sufficiently large volume. For this reason, trained network is used for the solution of homogeneous and inhomogeneous of significantly more complex geometries (e.g., sphere, torus, cone, cube, cylinder) with different ϵ_r values. Numerical results are presented and discussed in the Numerical Results chapter in detail.

Chapter 4

Numerical Results

In this chapter, numerical results of scattering from several homogenous and inhomogenous dielectric objects are presented. These results are obtained via both conventional MLFMA and T-MLFMA. Scattered far-zone electric fields, number of iterations, and MVM times in iterations are discussed for both MLFMA and T-MLFMA simulations. Firstly, T-MLFMA analyses for different BTET, TTET, and BTC, TTC values (basis and testing trimming parameters which are explained in the previous chapter) are performed for a homogeneous dielectric sphere. These analyses are performed to observe the sensitivity of T-MLFMA method to different BTET, TTET, and BTC, TTC values. After these analyses, parameter values are determined. Next, we discuss the solutions of different homogenous and inhomogenous spheres, layered spherical shells, torus, cone, cube, cylinder, and some other relatively complex geometries by considering the sensitivity analyses results.

In all simulations, the objects are illuminated by linearly polarized uniform plane waves (x-polarized uniform plane wave propagating in the z-direction) and FGMRES is used as the iterative solver. The desired residual error of the iterative solver and the maximum number of iterations are set to 10^{-3} and 2000, respectively. Moreover, a block diagonal preconditioner (block size = 2) is used in all simulations. Singularity extraction techniques are applied in the simulations involving dielectric cone. In T-MLFMA simulations, the far-zone scattered electric field error is given by

$$Error = \frac{||\mathbf{E}_{simulated} - \mathbf{E}_{reference}||_2}{||\mathbf{E}_{reference}||_2}, \tag{4.1}$$

and calculated with respect to the conventional MLFMA result or Mie series solution (if available), where $|| \quad ||_2 = L_2$ norm of the vector. In (4.1), $\mathbf{E}_{simulated}$ stands for the far zone electric field vector calculated with T-MLFMA (or MLFMA if Mie series solution is available), and $\mathbf{E}_{reference}$ is used to denote the far-zone electric field vector calculated with either Mie series solution (if available) or the conventional MLFMA.

4.1 Trimming Threshold Analysis

In this section, T-MLFMA simulations are performed for different values of BTET and TTET separately. BTC and TTC values are set to 2 in these simulations for basis and testing trimmings, respectively. Therefore, separate analyses are performed for both basis and testing trimming to analyze the effect of error threshold levels. 2λ diameter homogeneous sphere with $\epsilon_r = 3$ is used in this set of simulations and the operating frequency is 1 GHz (λ=0.3 m). The object is discretized with 413,654 SWG functions. The far-zone scattered electrical field, error, and MVM times obtained from the T-MLFMA simulations are compared with that of MLFMA. Also the error of MLFMA and T-MLFMA with respect to the Mie series solution are investigated.

First, only basis trimming is applied. BTC is set to 2, and both MLFMA and T-MLFMA results are compared to the Mie series solution.

In Fig. 4.1(a), the scattered far-zone fields obtained with T-MLFMA for different threshold values (BTET = 0.01, 0.05 and 0.1), and the scattered far-zone

Table 4.1: Numerical results for MLFMA and T-MLFMA with only basis trimming for different BTET values for the scattering from a homogeneous dielectric sphere with 2λ diameter and $\epsilon_r = 3$ at 1 GHz

	BTET	Number Of Iterations	MVM Time (s)	Error w.r.t. MLFMA (%)	Error w.r.t. Mie (%)
MLFMA	-	161	4824	-	4.85
T-MLFMA	0.1	89	2593	9.63	12.99
	0.05	116	3403	5.13	6.68
	0.01	158	4607	0.31	4.70

field obtained with conventional MLFMA are depicted. The progress of residual errors in T-MLFMA and MLFMA for corresponding simulations are shown in Fig. 4.1(b). In Fig. 4.1(c), the included SWG basis functions at each iteration in T-MLFMA simulations are given, and lastly, MVM times for each iteration for T-MLFMA and conventional MLFMA simulations are shown in Fig. 4.1(d).

We can observe that, when the BTET value decreases from 0.1 to 0.01, the number of iterations increases, and the resultant far-zone electric field converges to the MLFMA solution. This convergence can be observed more clearly in the back-scattered fields in Fig. 4.1(a) when the BTET value decreases from 0.1 to 0.01 in a controllable manner and Table 4.1 tabulates the details of the analysis. The far-field errors of T-MLFMA for BTET 0.1, 0.05 and 0.01 are 12.99%, 6.68%, and 4.70% with respect to Mie series solution (which is analytical). The same errors with respect to the conventional MLFMA are 9.63%, 5.13%, and 0.31%. As expected, as BTET is decreased, the number of iterations and MVM time increase but the accuracy improves. Nevertheless, T-MLFMA is always faster than the conventional MLFMA. Depending on the application one can sacrifice from the accuracy and increase the efficiency or vice versa.

In the second part, only testing function trimming is applied, and the numerical results for T-MLFMA for TTET = 0.01, 0.05, and 0.1 with TTC = 2 are compared with the conventional MLFMA and Mie series results in Fig. 4.2. In Fig. 4.2(a), the scattered far-zone fields obtained with T-MLFMA for different threshold values (TTET = 0.01, 0.05 and 0.1), and the scattered far-zone field obtained with conventional MLFMA are shown. The progress of residual errors in

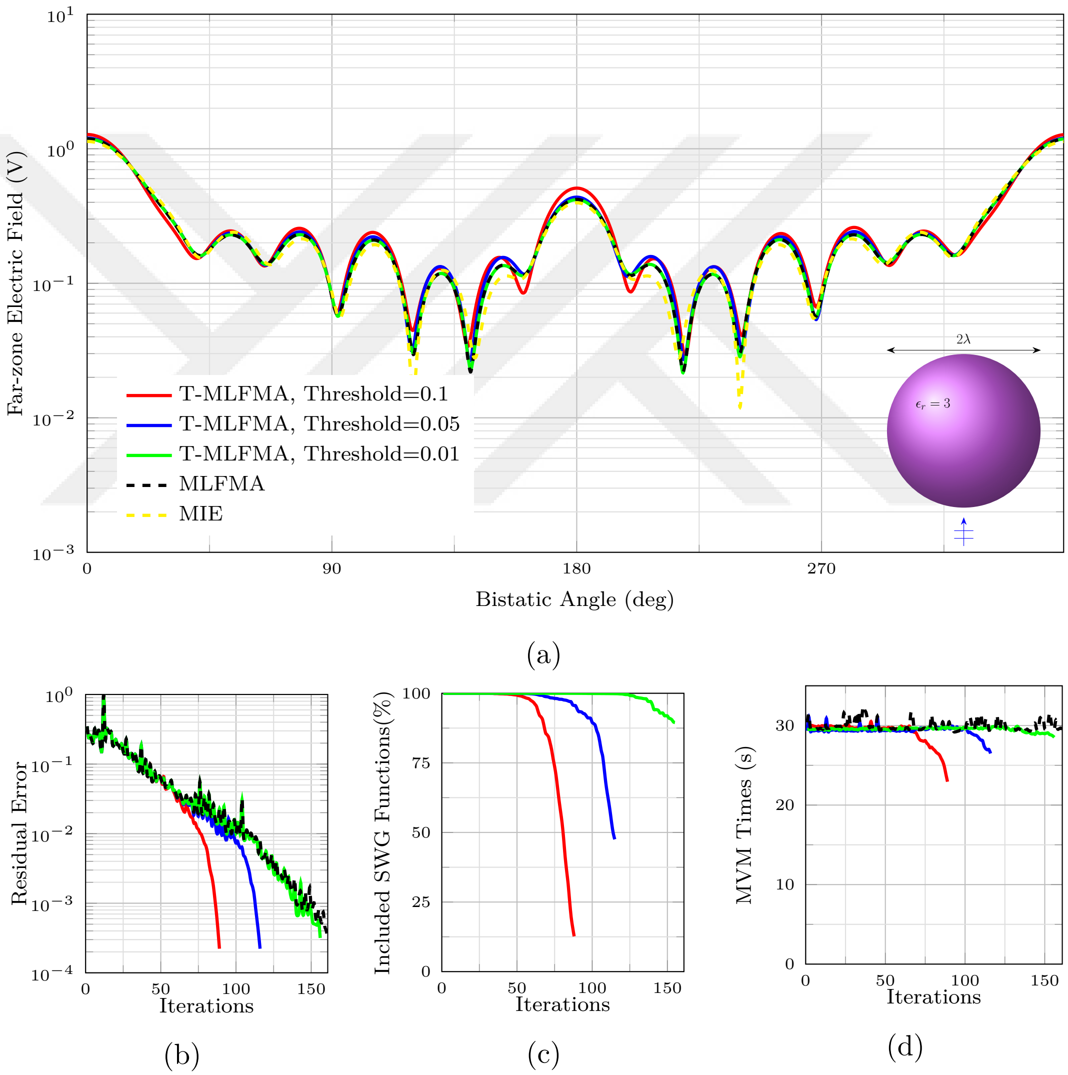

Figure 4.1: (a) The scattered electric field of the homogenous dielectric sphere with 2λ diameter and $\epsilon_r = 3$ for different Basis Trimming Error Threshold values with BTC = 2, (b) residual errors, (c) included SWG functions, and (d) MVM time at each iteration

T-MLFMA and MLFMA for corresponding simulations are shown in Fig. 4.2(b). In Fig. 4.2(c), the included SWG testing functions at each iteration in T-MLFMA simulations are given, and lastly, MVM times for each iteration for T-MLFMA and conventional MLFMA simulations are depicted in Fig. 4.2(d).

Table 4.2: Numerical results for MLFMA and T-MLFMA with only testing trimming for different TTET values for the scattering from a homogeneous dielectric sphere with 2λ diameter and $\epsilon_r = 3$ at 1 GHz

	TTET	Number Of Iterations	MVM Time (s)	Error w.r.t. MLFMA (%)	Error w.r.t. Mie (%)
MLFMA	-	161	4824	-	4.85
T-MLFMA	0.1	111	3203	7.50	12.36
	0.05	127	3719	2.45	6.68
	0.01	148	4328	0.39	4.68

It can be observed that when the TTET value decreases from 0.1 to 0.01, the number of iterations increases and the resultant far-zone electric field converges to the MLFMA solution. This convergence can be observed more clearly in back-scattered fields in Fig. 4.2(a) when the TTET value decreases from 0.1 to 0.01 and Table 4.2 tabulates the details of the analysis. The far-field errors of T-MLFMA for TTET 0.1, 0.05 and 0.01 are 12.36%, 6.68%, and 4.68% with respect to the Mie series solution (which is analytical). The same errors with respect to the conventional MLFMA are 7.50%, 2.45%, and 0.39%. As expected, as TTET is decreased, the number of iterations and MVM time increase but the accuracy improves. Still, T-MLFMA is always faster than the conventional MLFMA. Depending on the application one can sacrifice from the accuracy and increase the efficiency or vice versa.

One final conclusion (based on the results) that the basis function trimming provides faster convergence than the testing function trimming for the same counter and threshold values, however the scattered far-field error is smaller in testing trimming case. Note that, as BTET and TTET decrease, the number of iterations and MVM time increase and results become more accurate, and T-MLFMA is always faster than conventional MLFMA. More efficient results can be obtained by sacrificing from the accuracy and vice versa.

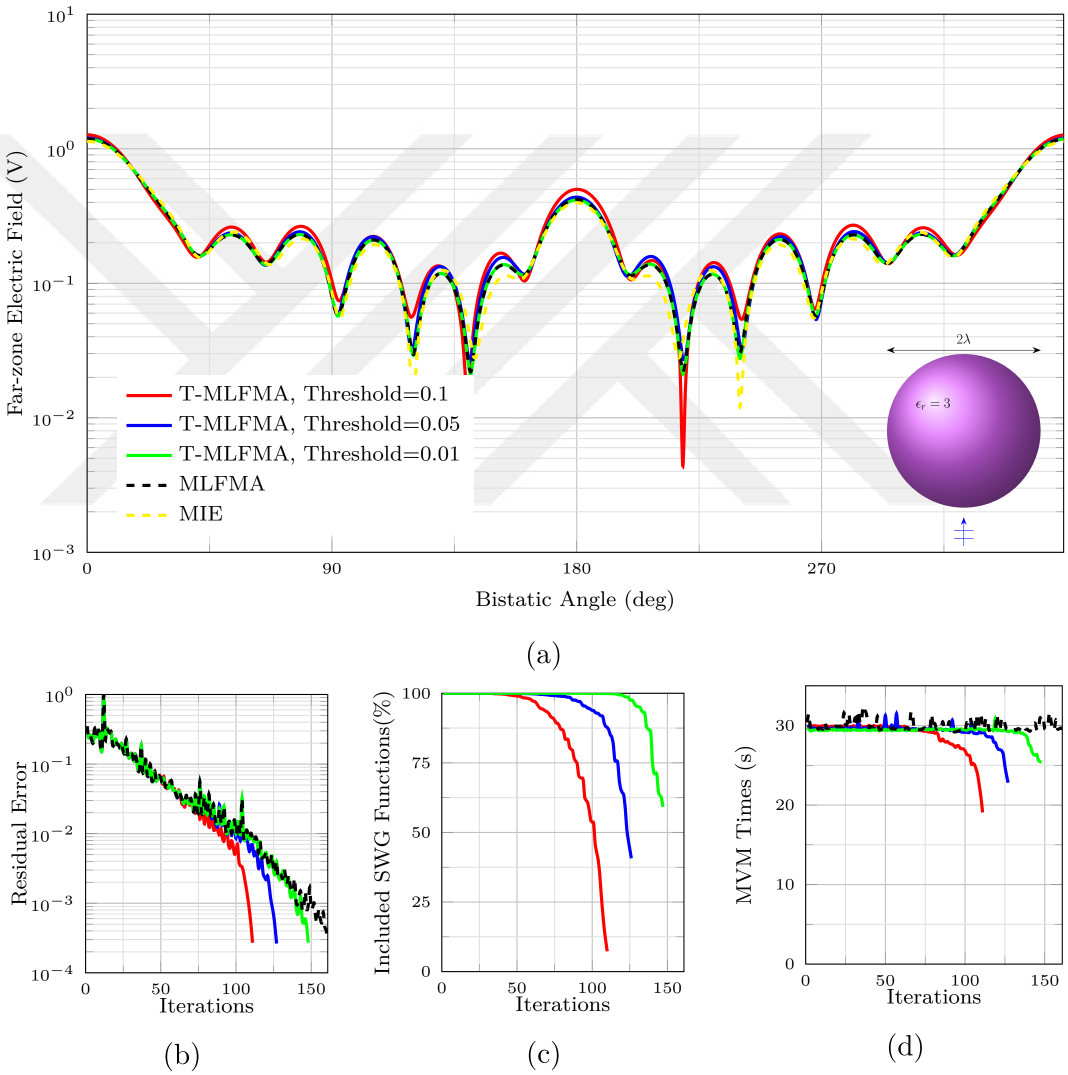

Figure 4.2: (a) The scattered electric field of the homogenous dielectric sphere with 2λ diameter and $\epsilon_r = 3$ for different Testing Trimming Error Threshold values with TTC = 2, (b) residual errors, (c) included SWG functions, and (d) MVM time at each iteration

4.2 Trimming Counter Analysis

As we have observed in Fig 4.1 and Fig 4.2, the trimming alters the accuracy of MVM calculations and yields errors in far-zone scattered electric fields. These errors are mainly caused by the improper trimming of basis and testing functions, since the trimming process is based on predictions. To decrease this undesired errors, we allow the interactions of trimmed basis and testing functions proceed in a certain number of iterations called trimming counter (BTC for basis and TTC for testing as explained during the explanation of T-MLFMA). In this set of simulations, we analyze the effect of these counter values to the performance of T-MLFMA. Similar simulation parameters are used and the object is illuminated in the same way as those explained in the Trimming Threshold Analysis section.

First, only basis function trimming is employed in the simulations, and numerical results for T-MLFMA for BTC = 2, 3, 4, 5, 6 with BTET = 0.1 are compared with the conventional MLFMA and the Mie series results in Fig. 4.3.

We can observe that, when the BTC values are lowered from 6 to 2, the number of iterations reduces, and the MVM time for each iteration also decreases. However, the far-field error both with respect to the conventional MLFMA and Mie series solution increase due to the rapid convergence for small values of BTC. The far field errors for BTC = 2, 3, 4, 5, and 6 are listed in Table 4.3 as 9.63%, 7.36%, 5.82%, 4.91%, and 3.42%, respectively. The same errors with respect to the Mie series solution are also tabulated in the same table. T-MLFMA simulations converge in 89, 105, 117, 120, 124 iterations on the contrary to 161 iterations of MLFMA leading to a decrease in the run time of the total MVM as seen in Table 4.3. We can conclude that keeping BTC = 3 can limit the far field error under 1% and we obtain approximately 30% speed up by using only basis function trimming.

Second, only testing function trimming is applied in the simulations and numerical results for T-MLFMA for TTC = 2, 3, 4, 5, 6 with TTET = 0.1 are compared with the conventional MLFMA and Mie series results in Fig. 4.4.

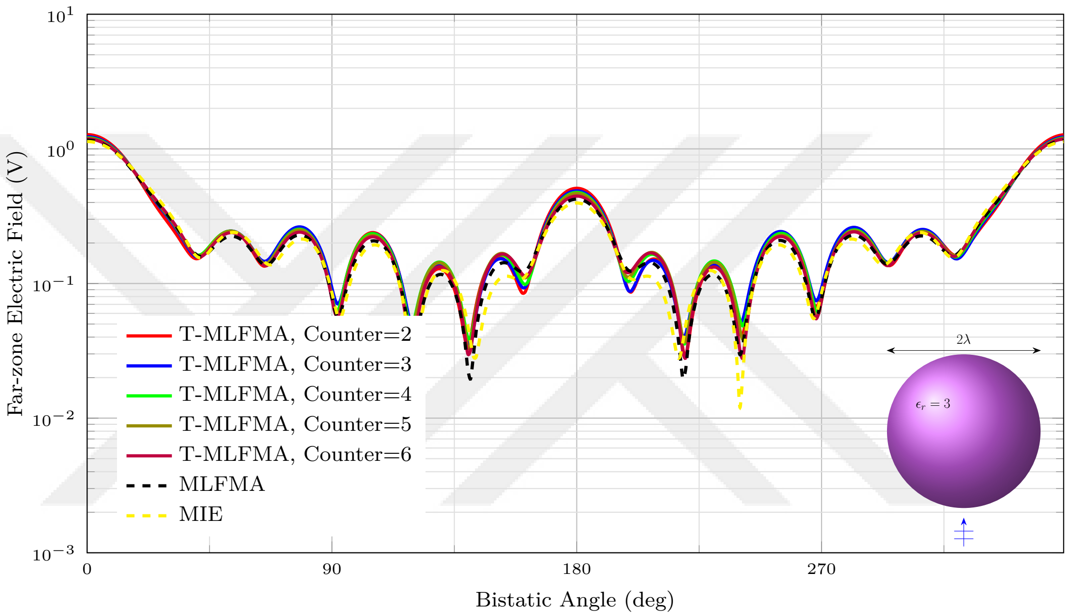

(a)

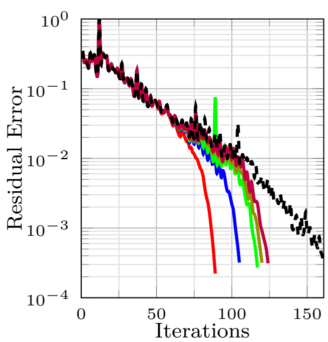

(b)

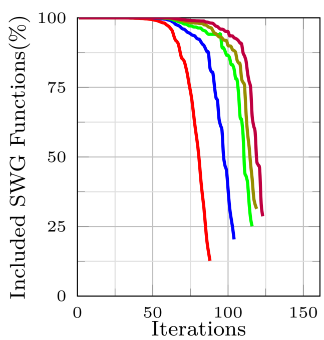

(c)

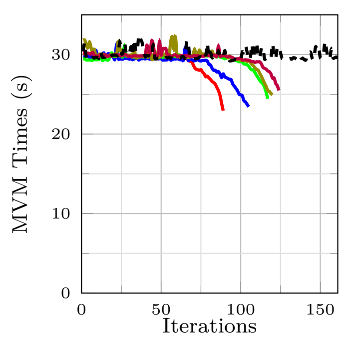

(d)

Figure 4.3: (a) The scattered electric field of the homogenous dielectric sphere with 2λ diameter and $\epsilon_r = 3$ for different Basis Trimming Counter values with BTET $= 0.1$, (b) residual errors, (c) included SWG functions, and (d) MVM time at each iteration

Table 4.3: Numerical results for MLFMA and T-MLFMA with only basis trimming for different BTC values for the scattering from a homogeneous dielectric sphere with 2λ diameter and $\epsilon_r = 3$ at 1 GHz (BTET = 0.1)

	BTC	Number Of Iterations	MVM Time (s)	Error w.r.t. MLFMA (%)	Error w.r.t. Mie (%)
MLFMA	-	161	4824	-	4.85
T-MLFMA	2	89	2590	9.63	12.99
	3	105	3024	7.35	10.49
	4	117	3435	5.82	9.21
	5	120	3557	4.91	8.38
	6	124	3676	3.42	6.95

In Fig. 4.4(a), the scattered far-zone fields obtained with T-MLFMA for different threshold values (TTC = 2, 3, 4, 5, and 6), and the scattered far-zone field obtained with the conventional MLFMA are depicted. The progress of residual errors in T-MLFMA and MLFMA for corresponding simulations are shown in Fig. 4.4(b). In Fig. 4.4(c), the included SWG testing functions at each iteration in T-MLFMA simulations are given and lastly, MVM times for each iteration for T-MLFMA and conventional MLFMA simulations are shown in Fig. 4.4(d).

Table 4.4 tabulates the details of the analysis. The far-field errors of T-MLFMA with respect to the conventional MLFMA for TTC 2, 3, 4, 5, and 6 are 7.50%, 3.72%, 2.02%, 1.35%, and 1.02%, respectively. The same errors with respect to the Mie series solution are also tabulated in the same table. As expected, as TTC is increased, the number of iterations and MVM time increase but the accuracy improves. Nonetheless, T-MLFMA is always faster than the conventional MLFMA. Depending on the application one can sacrifice from the accuracy and increase the efficiency or vice versa.

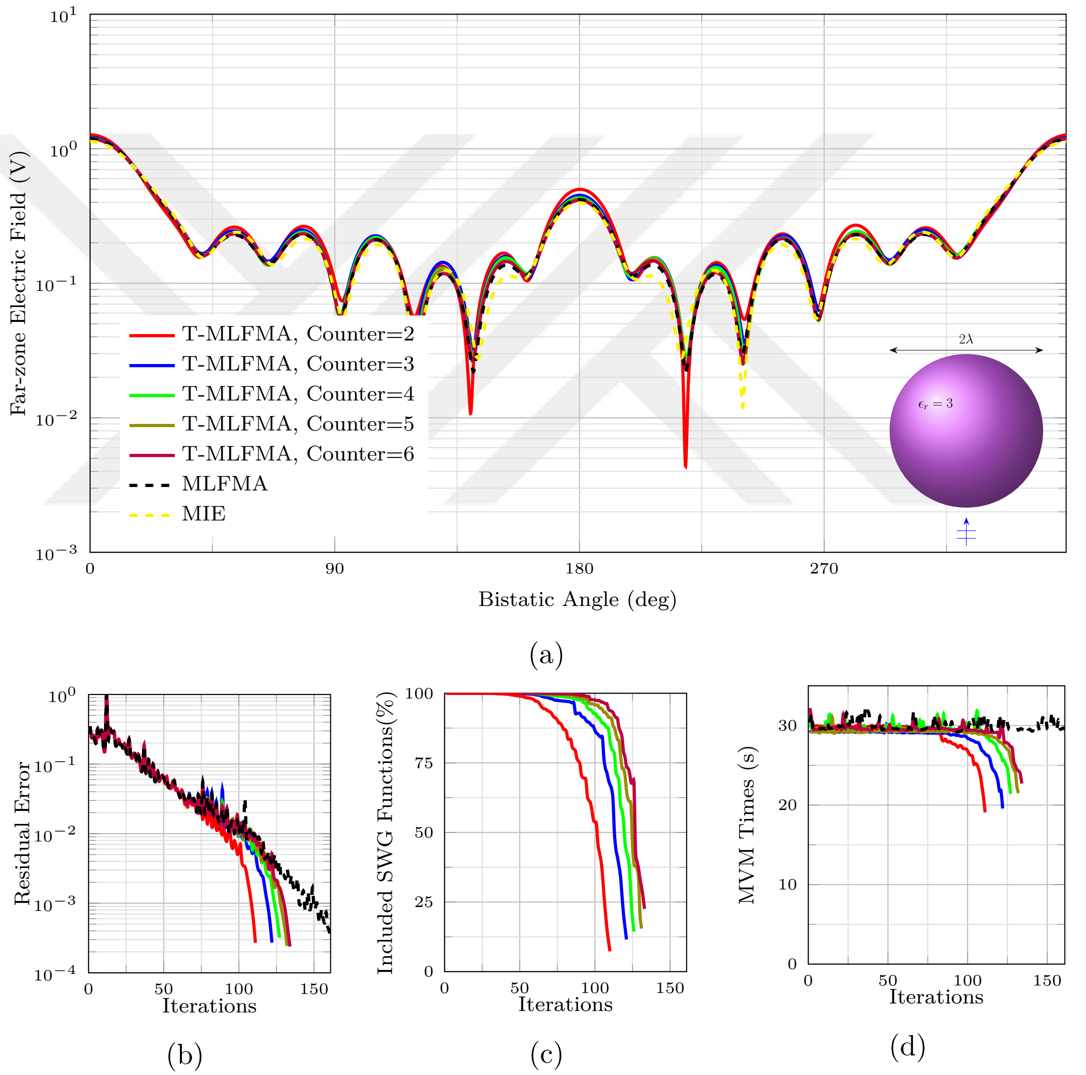

Figure 4.4: (a) The scattered electric field of the homogenous dielectric sphere with 2λ diameter and $\epsilon_r = 3$ for different Testing Trimming Counter values with TTET = 0.1, (b) residual errors, (c) included SWG functions, and (d) MVM time at each iteration

Table 4.4: Numerical results for MLFMA and T-MLFMA with only testing trimming for different TTC values for the scattering from a homogeneous dielectric sphere with 2λ diameter and $\epsilon_r = 3$ at 1 GHz (TTET = 0.1)

	TTC	Number Of Iterations	MVM Time (s)	Error w.r.t. MLFMA (%)	Error w.r.t. Mie (%)
MLFMA	-	161	4824	-	4.85
T-MLFMA	2	111	3203	7.50	12.36
	3	122	3477	3.72	7.84
	4	127	3719	2.02	6.18
	5	132	3809	1.35	5.25
	6	134	3928	1.02	5.12

4.3 Investigation of T-MLFMA Performance for relatively More Complex Objects

In this section, trimming threshold and trimming counter analyses (if necessary) are performed for different homogeneous and inhomogeneous dielectric objects. Both basis and testing trimmings are applied in T-MLFMA simulations. Same values are assigned to testing and basis threshold values (BTET & TTET), and also same values are used for basis and testing counter values (BTC & TTC).

Homogeneous Full-Sphere Results: Firstly, a homogeneous sphere with 1.5λ diameter and $\epsilon_r = 6$ is considered and the operating frequency is 1 GHz ($\lambda = 0.3$ m). The object is discretized with 777,308 SWG functions. Far-zone scattered electrical field, residual errors and MVM times in each iteration obtained from T-MLFMA are presented and are compared with that of the conventional MLFMA.

Different from Fig. 4.1(b) - 4.4(b), in Fig. 4.5(b), the included basis and testing SWG functions are depicted together in solid and dashed colors, respectively. The numerical results for threshold value of 0.1, 0.05 and 0.03 are shown in red, blue and green colors, respectively. Moreover, BTC and TTC values are set to 5 and the details of the analysis are given in Table 4.5. We can observe that, the reduction of threshold value from 0.1 to 0.03 provides more accurate results while the number of iterations increase slightly but still significantly less than that of the

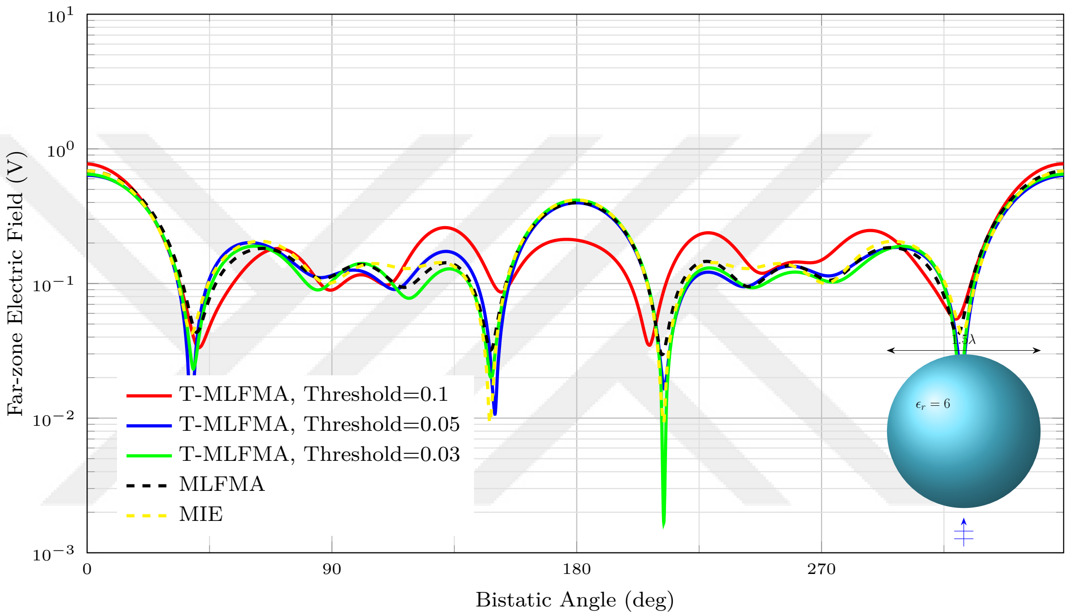

(a)

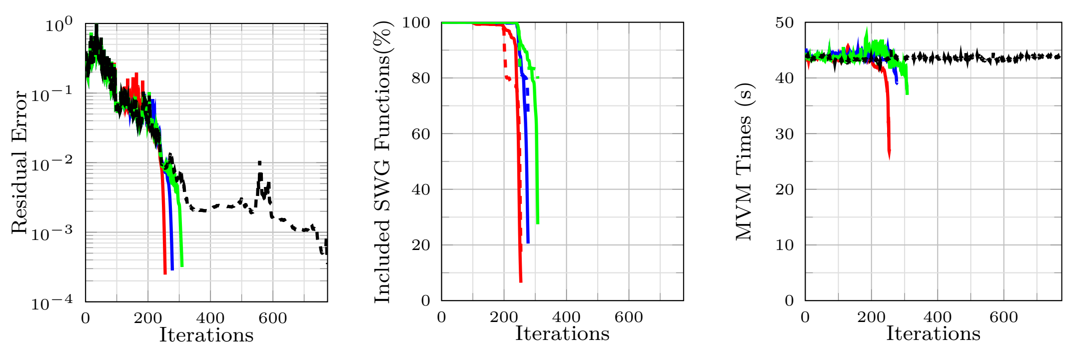

(b) (c) (d)

Figure 4.5: (a) The scattered electric field of the homogeneous dielectric sphere with 1.5λ diameter and $\epsilon_r = 6$ for different Testing-Basis Trimming Error Threshold values with BTC = TTC = 5, (b) residual errors, (c) included SWG functions, and (d) MVM time at each iteration

conventional MLFMA. By using the TTET and BTET value of 0.03, T-MLFMA and MLFMA results are very consistent with each other for forward-scattered and back-scattered fields. The MVM time is reduced from 33307 seconds to 13471 seconds, resulting in approximately three-fold acceleration.

Table 4.5: Numerical results of MLFMA and T-MLFMA with different threshold values for the scattering from a homogeneous dielectric sphere with 1.5λ diameter and $\epsilon_r = 6$ at 1 GHz

	BTET and TTET Value	Number Of Iterations	MVM Time (s)	Error w.r.t. MLFMA (%)	Error w.r.t. Mie (%)
MLFMA	-	774	33307	-	6.62
T-MLFMA	0.03	308	13471	6.41	7.27
	0.05	277	12163	8.33	7.87
	0.10	254	10914	23.57	29.27

Next, another an homogeneous sphere with 0.375λ diameter and $\epsilon_r = 25$ is considered and the operating frequency is 750 MHz ($\lambda = 0.4$ m). The object is discretized with 178,286 SWG functions. Far-zone scattered electrical field, residual errors and MVM times in each iteration obtained from T-MLFMA are presented and are compared with that of the conventional MLFMA in Fig. 4.6. The numerical results for threshold value of 0.01 and 0.005 are shown in red and blue colors, respectively. Moreover, BTC and TTC values are set to 5 and the details of the analysis are given in Table 4.6. We can observe that, the reduction of threshold value from 0.01 to 0.005 provides more accurate results while the number of iterations is not changed significantly but still less than that of the conventional MLFMA. By using the TTET and BTET value of 0.005, T-MLFMA and MLFMA results are very consistent with each other for forward-scattered and back-scattered fields. The MVM time is reduced from 989 seconds to 889 seconds, resulting in 1.2 times acceleration.

Table 4.6: Numerical results of MLFMA and T-MLFMA with different threshold values for the scattering from a homogeneous dielectric sphere with 0.5λ diameter and $\epsilon_r = 25$ at 0.75 GHz

	BTET and TTET Value	Number Of Iterations	MVM Time (s)	Error w.r.t. MLFMA (%)	Error w.r.t. Mie (%)
MLFMA	-	177	989	-	1.45
T-MLFMA	0.005	148	818	3.44	3.85
	0.01	156	789	24.70	25.64

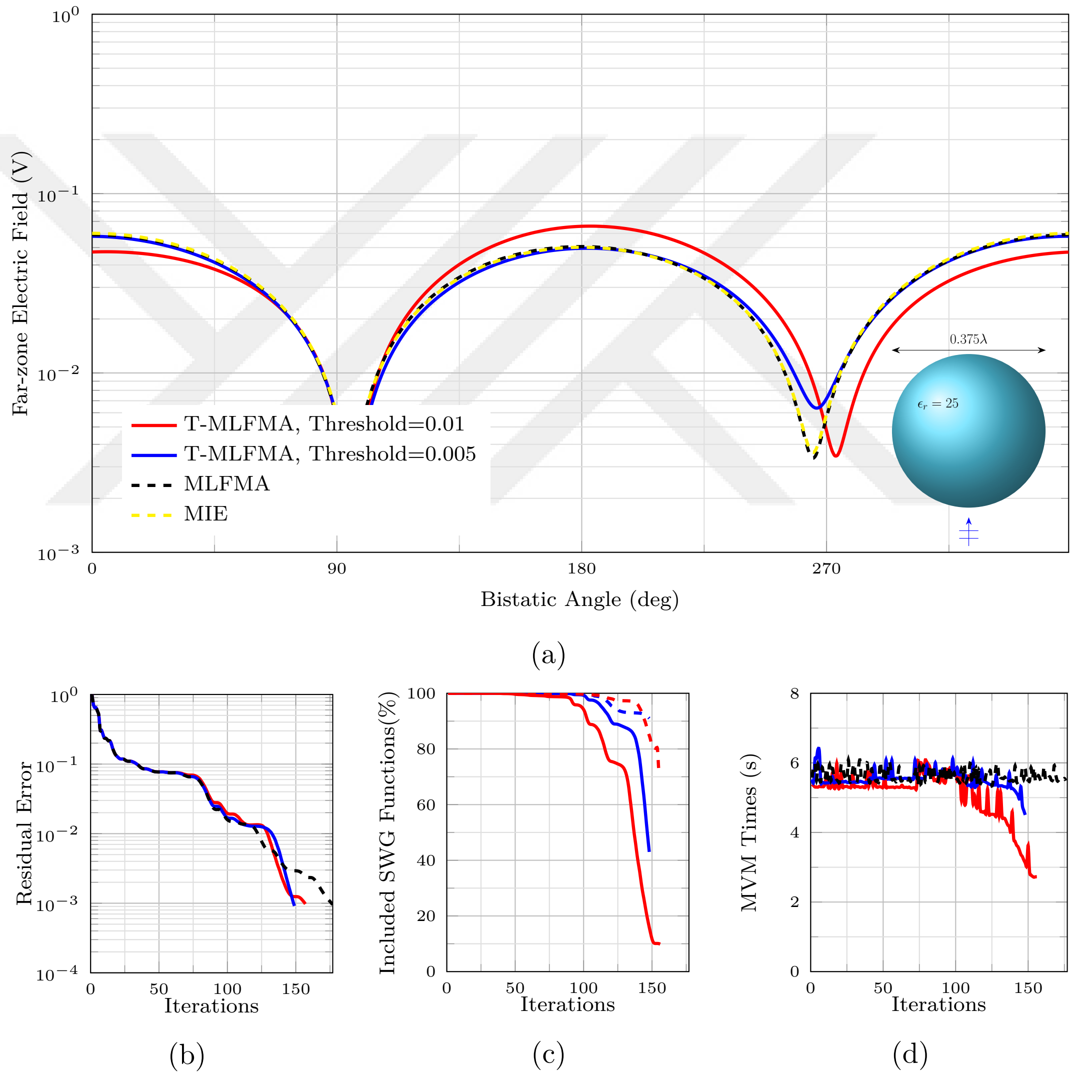

Figure 4.6: (a) The scattered electric field of the homogeneous dielectric sphere with 0.375λ diameter and $\epsilon_r = 25$ for different Testing-Basis Trimming Error Threshold values with BTC = TTC = 5, (b) residual errors, (c) included SWG functions, and (d) MVM time at each iteration

Inhomogeneous Full Sphere Results: Next, scattering from an inhomogeneous (layered) sphere is investigated, and results for T-MLFMA and MLFMA are presented and compared with each other as well as with the Mie series solution in Fig. 4.7. The inhomogeneous sphere involves two concentric spheres. The inner sphere has $\lambda/2$ radius and filled with a dielectric material with $\epsilon_r = 2$, and the outer homogeneous spherical shell has $\lambda/2$ thickness and filled with a dielectric material with $\epsilon_r = 5$. The operating frequency is 1 GHz (λ= 0.3 m). The object is discretized with 1,035,465 SWG functions by considering the mesh mating conditions, which ensure smooth transitions in meshing at the border of two regions. Far-zone scattered electric field, residual errors and MVM times in each iteration obtained from T-MLFMA are compared with that of the conventional MLFMA.

The numerical results for 3 different threshold values of 0.1, 0.03 and 0.01 are shown in red, blue and green colors, respectively, in Fig. 4.7. Also, TTC and BTC values are set to 5 and the details of the numerical results are tabulated in Table 4.7. For the threshold value of 0.1, the number of iterations is reduced significantly from 1661 to 1112. However, the accuracy of the far-zone scattered field is not sufficient and the far-field error is approximately 19.11%. We observe that, the reduction of threshold value from 0.1 to 0.03 provides more accurate results while the number of iterations increase slightly; but still significantly less than that of the conventional MLFMA. By using the threshold value of 0.03, we achieve 6.41% far-field error and T-MLFMA and MLFMA results become significantly consistent for forward-scattered and back-scattered fields. The MVM time is reduced from 620271 seconds to 343702 seconds, resulting in approximately two-fold acceleration. For further accurate results, the threshold value is decreased to 0.01 and far-field error is obtained as 3.61% while 1.5 times speed-up in MVM time is achieved.

As the next simulation, again an inhomogeneous sphere involving two concentric spheres is analyzed, However, this time, the inner sphere has $\lambda/2$ radius and filled with a dielectric material with $\epsilon_r = 5$, and the outer spherical shell has $\lambda/2$ thickness and filled with a dielectric material with $\epsilon_r = 2$. The operating frequency is again 1 GHz (λ= 0.3 m). The object is discretized with 322,930 SWG functions by considering the mesh mating conditions which ensure smooth

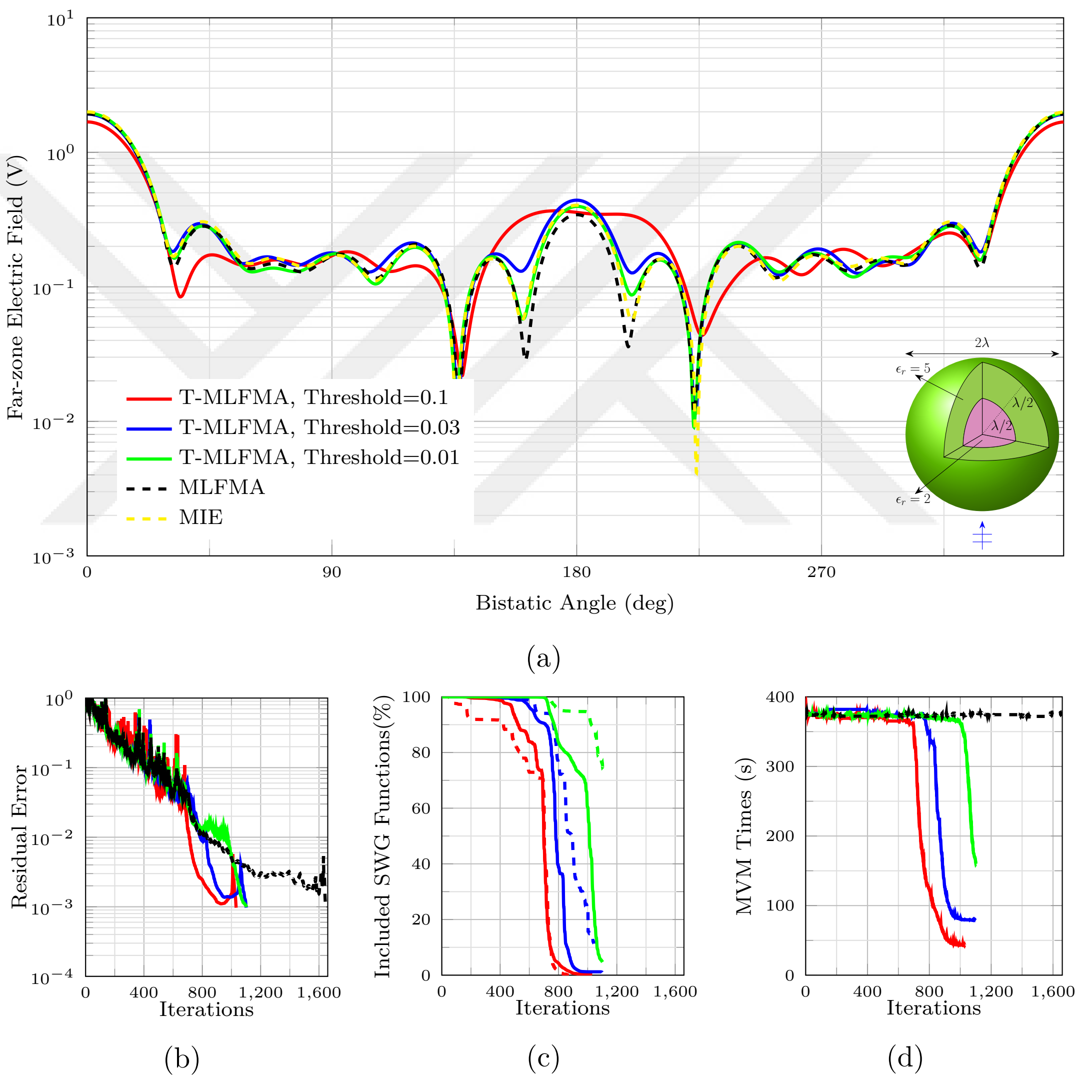

Figure 4.7: (a) The scattered electric field of the inhomogeneous concentric sphere with radius^{in} $=\lambda/2$, $\epsilon_r^{in} = 2$ and radius^{out} $=\lambda$, $\epsilon_r^{out} = 5$ for different Testing-Basis Trimming Error Threshold values with BTC = TTC = 5 (b) residual errors, (c) included SWG functions, and (d) MVM time at each iteration

Table 4.7: Numerical results of MLFMA and T-MLFMA for different threshold values for the scattering from a inhomogeneous dielectric sphere with radius^{in} $=\lambda/2$, $\epsilon_r^{in} = 2$ and radius^{out} $=\lambda$, $\epsilon_r^{out} = 5$ at 1 GHz

	BTET and TTET Value	Number Of Iterations	MVM Time (s)	Error w.r.t. MLFMA (%)	Error w.r.t. Mie (%)
MLFMA	-	1661	620271	-	4.65
T-MLFMA	0.01	1112	400534	3.61	2.96
	0.03	1109	343702	6.41	5.04
	0.10	1040	294105	19.11	19.90

transitions in meshing at the border of two regions. Far-zone scattered electric field, residual errors and MVM times in each iteration obtained from T-MLFMA are compared with that of the conventional MLFMA. The numerical results are depicted in Fig. 4.8 for 3 different threshold values of 0.05, 0.03 and 0.01 and these results are shown in red, blue and green colors, respectively. Also, TTC and BTC values are set to 5 and the details of the numerical results are tabulated in Table 4.8. For the threshold value of 0.03 and 0.05, the number of iterations are not reduced significantly. However, T-MLFMA provides approximately 2.3 and 2.7 times speed-up in MVM times while the far field errors are obtained as 5.38% and 9.91%, respectively. Moreover, more accurate result with 2.37% far-field error is obtained for the threshold value of 0.01 with 1.2 times speed-up in MVM time.

Table 4.8: Numerical results of MLFMA and T-MLFMA for different threshold values for the scattering from a inhomogeneous dielectric sphere with radius^{in} $=\lambda/2$, $\epsilon_r^{in} = 5$ and radius^{out} $=\lambda$, $\epsilon_r^{out} = 2$ at 1 GHz

	BTET and TTET Value	Number Of Iterations	MVM Time (s)	Error w.r.t. MLFMA (%)	Error w.r.t. Mie (%)
MLFMA	-	1319	35888	-	1.54
T-MLFMA	0.01	1171	29493	2.37	2.35
	0.03	1059	15652	5.38	4.95
	0.05	1049	13653	9.91	9.43

Spherical Single-Layer Shell Results: Next, we consider spherical shell geometries, which enable us to increase the size of geometry without sacrificing from the high number of unknowns. As the first example, we present the results for a spherical shell with 4λ diameter, $\lambda/15$ thickness and $\epsilon_r = 6$. The operating

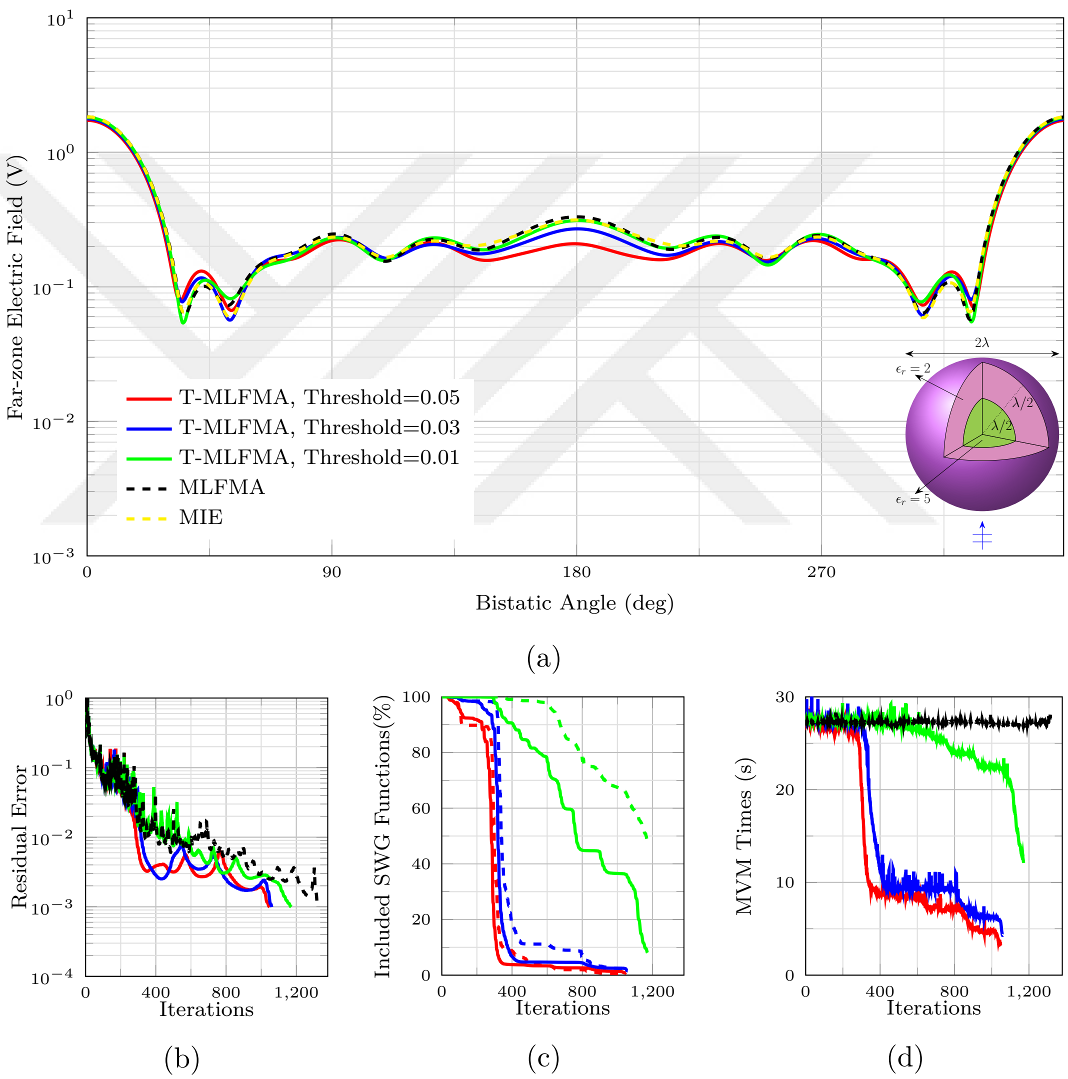

Figure 4.8: (a) The scattered electric field of the inhomogeneous concentric sphere with radius^{in} $=\lambda/2$, $\epsilon_r^{in} = 5$ and radius^{out} $=\lambda$, $\epsilon_r^{out} = 2$ for different Testing-Basis Trimming Error Threshold values with BTC = TTC = 5 (b) residual errors, (c) included SWG functions, and (d) MVM time at each iteration

frequency is 1 GHz ($\lambda = 0.3$ m). The object is discretized with 1,093,971 SWG functions. Far-zone scattered electric field, residual errors and MVM times in each iteration obtained from T-MLFMA are compared with that of the conventional MLFMA. The numerical results are depicted in Fig. 4.9 for 3 different threshold values of 0.1, 0.05 and 0.03, and these results are shown in red, blue and green colors, respectively. Moreover, TTC and BTC values are set to 3 and the details of the numerical results are tabulated in Table 4.9. For the threshold value of 0.1, the number of iterations are reduced significantly from 274 to 97 leading three-fold speed-up in MVM time. However, it does not provide accurate result for the back-scattered fields. Therefore, we decrease the threshold value to 0.05 and even further to 0.03, and we obtain more accurate results for the back-scattered field as can be observed in Fig. 4.9. Moreover, for the threshold values of 0.05 and 0.03, we obtain approximately 1.86 and 1.77 times speed-ups in MVM times while the far-field errors with respect to the conventional MLFMA are obtained as 3.62% and 0.62%, respectively.

Table 4.9: Numerical results of MLFMA and T-MLFMA for different threshold values for the scattering from the shell geometry with 4λ diameter, $\lambda/15$ thickness and $\epsilon_r = 6$ at 1 GHz

	BTET and TTET Value	Number Of Iterations	MVM Time (s)	Error w.r.t. MLFMA (%)	Error w.r.t. Mie (%)
MLFMA	-	274	16816	-	1.18
T-MLFMA	0.03	165	9463	0.62	1.41
	0.05	161	9026	3.62	4.00
	0.10	97	5526	2.97	2.52

Next, after investigating the performance of T-MLFMA for different BTET and TTET values for a shell geometry with 4λ diameter and $\epsilon = 6$, we set BTET and TTET values to 0.1, BTC and TTC values to 3 for another set of single-layer shell geometry simulations. The performance of T-MLFMA with these parameters for different shell objects are presented. The operating frequency is 1 GHz ($\lambda = 0.3$ m). The diameters of these shells are 4λ, 5λ and 6λ with the same thickness $\lambda/15$. The details of T-MLFMA and MLFMA results are tabulated in Table 4.10 for two different ϵ_r values, 4 and 6. The trimming is applied for both basis and testing, and BTET and TTET have the same value of 0.1 and also BTC and TTC values are set to 3 for all T-MLFMA simulations given in Table 4.10. In

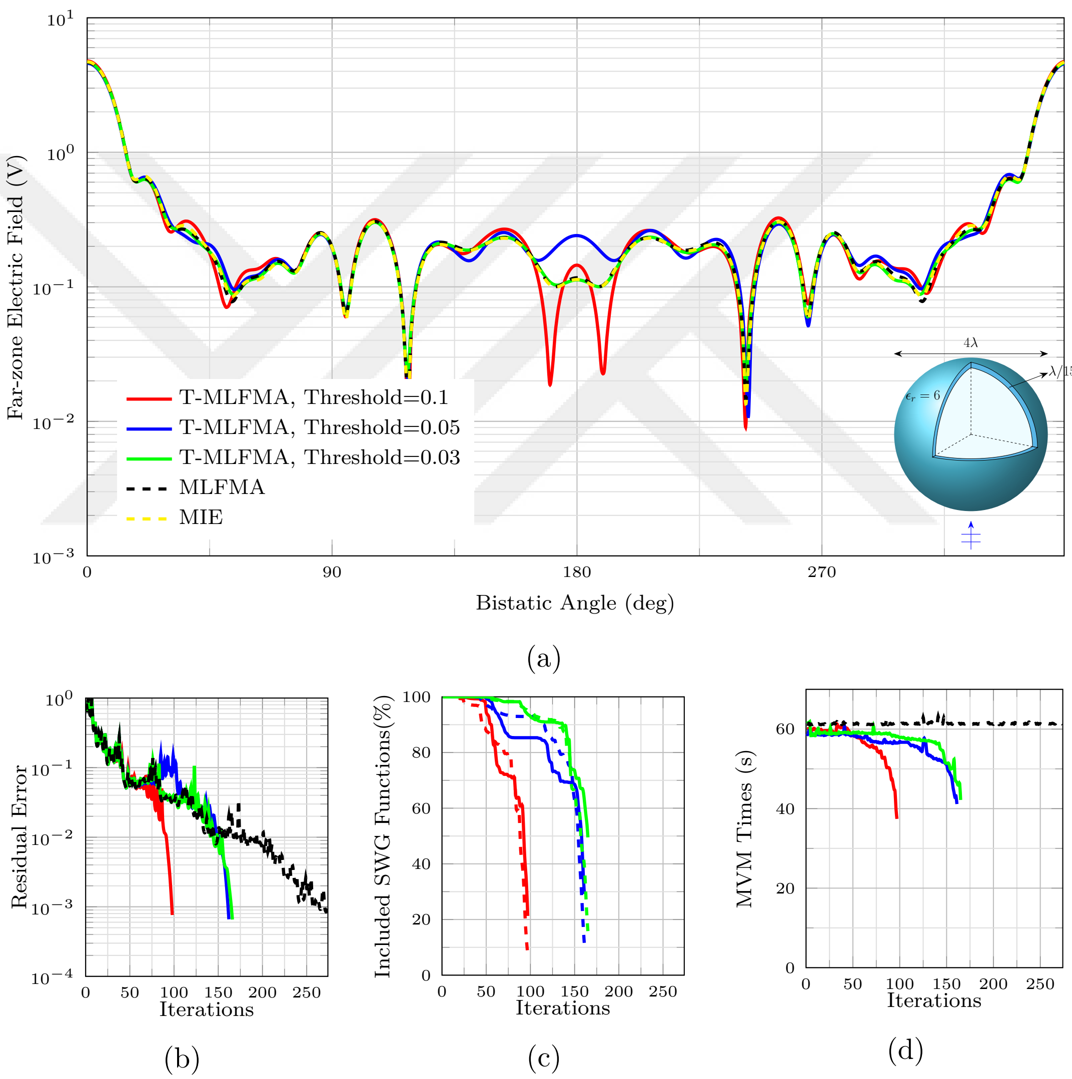

Figure 4.9: (a) The scattered electric field of the shell geometry with 4λ diameter, $\lambda/15$ thickness and $\epsilon_r = 6$ obtained with MLFMA and T-MLFMA for different Basis-Testing Trimming Error Threshold Values with BTC = TTC = 3, (b) residual errors, (c) included SWG functions, and (d) MVM time at each iteration

Fig. 4.10(a), (b) and (c), the scattered far-fields for T-MLFMA and MLFMA are presented for 4λ, 5λ and 6λ shell geometries with $\epsilon_r = 4$, respectively. In Fig. 4.11(a), (b) and (c), the scattered far-fields for T-MLFMA and MLFMA are presented for same shell geometries with $\epsilon_r = 6$. These objects are discretized with 1,131,236, 1,815,147 and 2,589,663 SWG functions. T-MLFMA provides 1.58, 1.82 and 1.83 times speed-up in MVM times for these shell geometries with ϵ_r value of 4. Moreover, significantly accurate results are achieved while far-field error value is below 3% for each simulation. Similar to ϵ_r value of 4 case, accurate results are obtained for the solution of the same shell geometries with $\epsilon_r = 6$. We achieve 3.05, 4.51 and 11.55 times speed-up in MVM times while the far-field errors are below 3%. We observe that T-MLFMA provides significant speed-up with highly accurate results for the scattered far-fields when the size of the object is large and ϵ_r value is high.

Table 4.10: Numerical results of MLFMA and T-MLFMA for the shell geometry with 4λ, 5λ and 6λ diameter, $\lambda/15$ thickness and $\epsilon_r = 4, 6$. In T-MLFMA BTET = TTET = 0.1 and BTC = TTC = 3 at 1 GHz

	Diameter	ϵ_r	Number of Iterations	MVM Time (s)	Error w.r.t. MLFMA (%)	Error w.r.t. Mie (%)
MLFMA	4λ	4	65	4182	-	1.09
	5λ		85	36240		1.95
	6λ		120	49373		1.58
T-MLFMA	4λ	4	44	2649	1.11	1.20
	5λ		49	19805	1.93	1.87
	6λ		69	27158	2.56	1.83
MLFMA	4λ	6	274	16816	-	1.18
	5λ		491	20416		2.44
	6λ		1392	580510		2.31
T-MLFMA	4λ	6	97	5526	2.97	2.52
	5λ		116	4524	1.92	3.72
	6λ		127	50302	1.21	2.33

Spherical Three-Layer Shell Results: Next, we consider a more complex problem involving 3 concentric dielectric spherical shell layers. The outermost diameter of the geometry is 1.5λ. From outer to inner, thicknesses and ϵ_r values of the shells are $\lambda/15$, $\lambda/20$, $\lambda/20$ and 2, 4, 6, respectively, as sketched as an in set in Fig. 4.12. The operating frequency is 0.5 GHz ($\lambda = 0.6$ m). The object is discretized with 1,955,966 SWG functions by considering the mesh mating conditions. Scattered

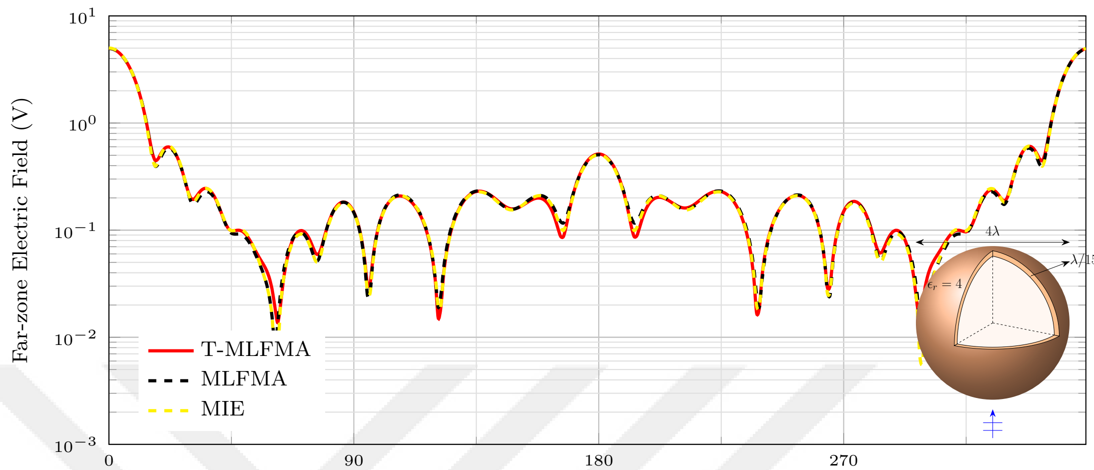

(a)

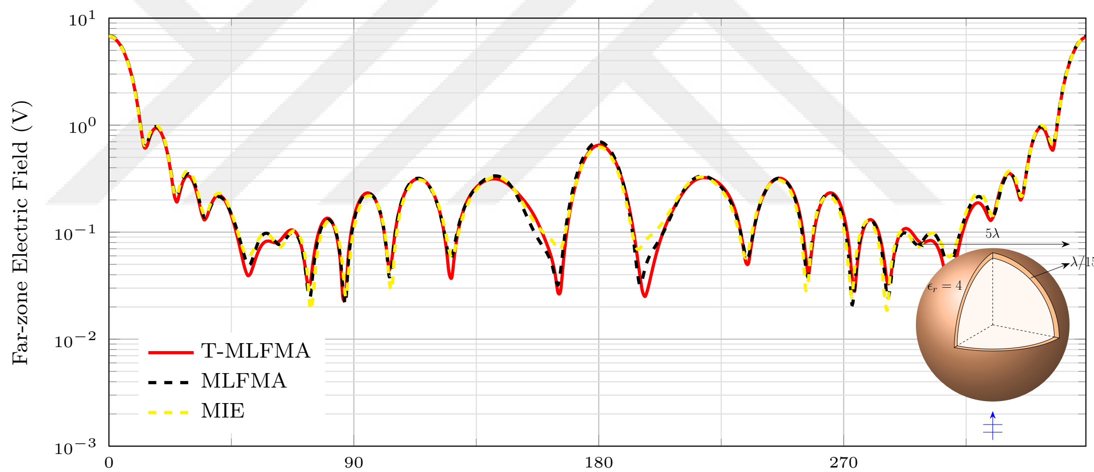

(b)

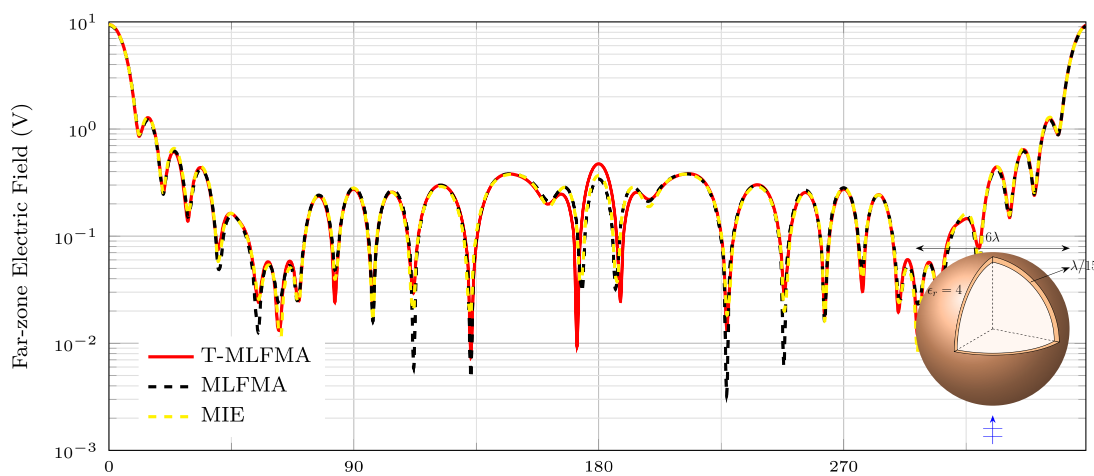

(c)

Figure 4.10: The scattered electric field of the shell geometry with a diameter of (a) 4λ, (b) 5λ and (c) 6λ. In each case, the thickness is $\lambda/15$ and $\epsilon_r = 4$. In T-MLFMA results, BTC = TTC = 3 and BTET = TTET = 0.1

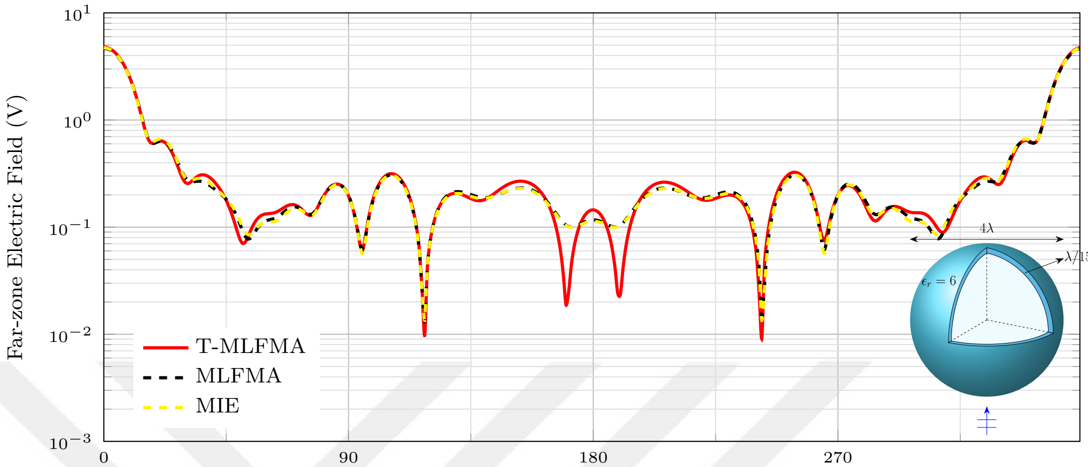

(a)

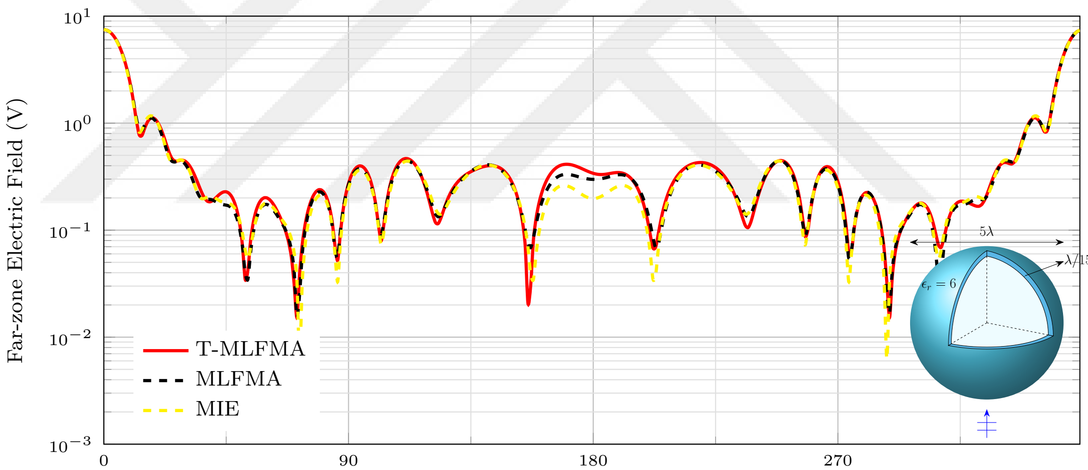

(b)

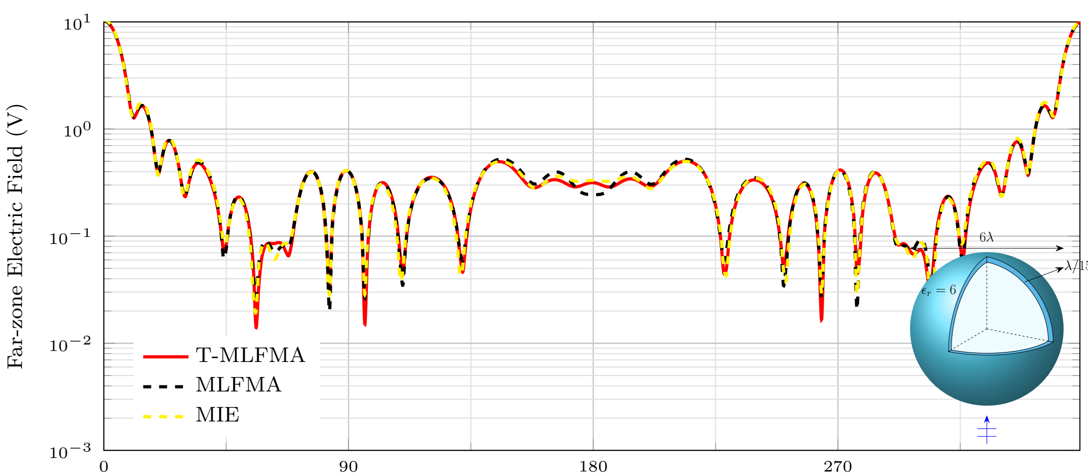

(c)

Figure 4.11: The scattered electric field of the shell geometry with a diameter of (a) 4λ, (b) 5λ and (c) 6λ. In each case, the thickness is $\lambda/15$ and $\epsilon_r = 6$. In T-MLFMA results, BTC = TTC = 3 and BTET = TTET = 0.1

Table 4.11: Numerical results of MLFMA and T-MLFMA for different threshold values for the scattering from the 3 layer shell geometry with the outermost diameter = 1.5λ with $\lambda/15$, $\lambda/20$ and $\lambda/20$ thicknesses and ϵ_r values 2, 4 and 6, respectively, from outer to inner at 0.5 GHz

	BTET and TTET Value	Number Of Iterations	MVM Time (s)	Error (%)
MLFMA	-	74	18944	-
T-MLFMA	0.05	47	12252	1.29
	0.1	47	11045	18.11

far-zone electric field, residual errors and MVM times in each iteration obtained from T-MLFMA are compared with that of the conventional MLFMA. The numerical results are tabulated in Table 4.11 for 2 different threshold values of 0.1 and 0.05, and these results are shown in red and blue colors, respectively. For the threshold value of 0.1, the number of iterations are reduced significantly from 74 to 47. However, it does not provide accurate result for the back-scattered fields. Therefore, when we decrease the threshold value to 0.05, we obtain more accurate results for the back-scattered field as can be observed in Fig. 4.12. However, the MVM time is increased from 11045 seconds to 12252 seconds with respect to the 0.1 threshold case. For the threshold value of 0.05, we achieve approximately 1.65 times speed up by obtaining 1.29% far-field error.

Next, we again consider a 3-layer spherical shell geometry which has a 3λ outermost diameter, However, from outer to inner, thicknesses and ϵ_r values of the shells are $2\lambda/15$, $\lambda/10$, $\lambda/10$ and 6, 4, 2, respectively. The operating frequency is 1 GHz ($\lambda = 0.3$ m). The object is discretized with 1,955,966 SWG functions again by considering the mesh mating conditions, which ensure smooth transitions in meshing at the border of the two regions. Scattered far-zone electric field, residual errors and MVM times in each iteration obtained from T-MLFMA are compared with that of the conventional MLFMA. The numerical results are depicted in Fig. 4.13 for 3 different threshold and counter value combinations. Moreover, the details of the numerical results are tabulated in Table 4.12. Firstly, threshold and counter values are set to 0.1 and 3, respectively. Secondly, the counter value is increased to 5 by keeping the threshold value the same. Finally, the threshold

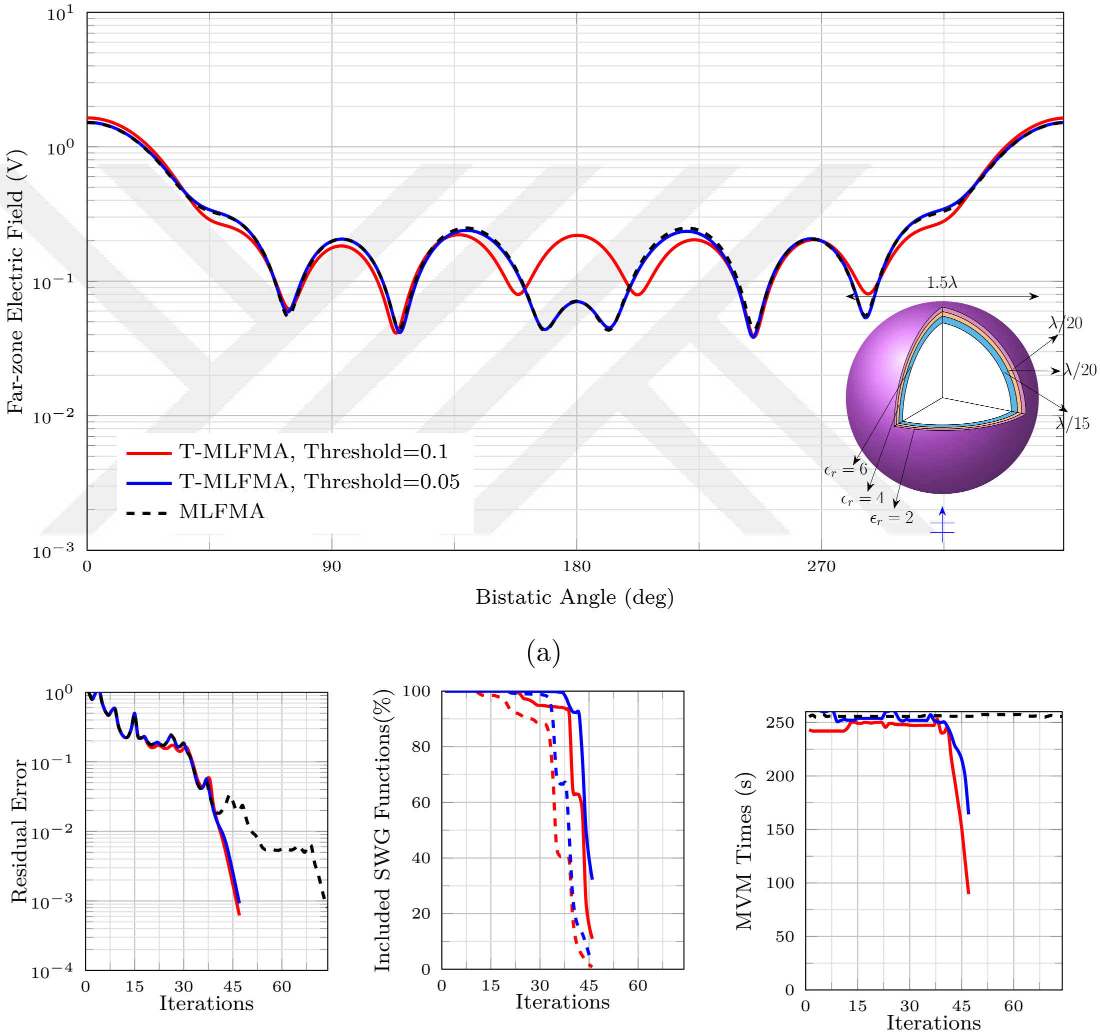

Figure 4.12: (a) The scattered electric field of the 3 layer shell geometry with the outermost diameter 1.5λ diameter with $\lambda/15$, $\lambda/20$ and $\lambda/20$ thicknesses and ϵ_r values 2, 4 and 6, respectively, from outer to inner, obtained with MLFMA and T-MLFMA for different Basis-Testing Trimming Error Threshold Values with BTC = TTC = 5, (b) residual errors, (c) included SWG functions, and (d) MVM time at each iteration

and counter values are assigned as 0.05 and 3, respectively. In the first case, T-MLFMA provides approximately 1.93 times speed-up with 5.83% far-field error with respect to the conventional MLMFA as indicated in Table 4.12. For the second case, we achieve approximately 1.77 times speed-up and 2.14% far-field error, and finally for the third situation, we achieve approximately 1.51 times speed-up and 1.51% far-field error.

Table 4.12: Numerical results of MLFMA and T-MLFMA for different threshold and counter values for the scattering from the 3 layer shell geometry with the outermost diameter is 3λ, and with $2\lambda/15$, $\lambda/10$ and $\lambda/10$ thicknesses and ϵ_r values 6, 4 and 2, respectively, from outer to inner at 1 GHz

	BTET and TTET Value	BTC and TTC Value	Number Of Iterations	MVM Time (s)	Error (%)
MLFMA	-	-	468	115025	-
T-MLFMA	0.1	3	251	59619	5.83
	0.1	5	266	65069	2.14
	0.05	3	315	76365	1.51

Now, after investigating the performance of T-MLFMA for different BTET and TTET values for two three-layer shell geometries, we set BTET and TTET values to 0.1, BTC and TTC values to 3 for another set of three-layer shell geometry simulations. The trimming is applied for both basis and testing. The operating frequency is 1 GHz ($\lambda = 0.3$ m). The outermost diameter of the three-layer shell object is 3λ, and from outer to inner, thicknesses are $2\lambda/15$, $\lambda/10$ and $\lambda/10$. Two different simulations with different ϵ_r values for shell layers are performed. As the first simulation, the ϵ_r values from outer to inner are set to 6, 1.2 and 1.5, respectively. As the second simulation, the ϵ_r values from outer to inner are set to 8, 1.2 and 3, respectively. The object is discretized with 1,955,966 SWG functions for both simulations. The details of T-MLFMA and MLFMA results for both simulations are tabulated in Table 4.13. In Fig. 4.14(a) and (b), the scattered far-fields obtained with T-MLFMA and MLFMA are presented for both simulations. T-MLFMA provides 2.2 and 2.7 times speed-up in MVM times, respectively. Moreover, significantly accurate results are achieved while the far-field error is at 2.17% and 5.19% for both simulations, respectively.

Homogeneous Cone Results: As a different geometry, we consider homogeneous

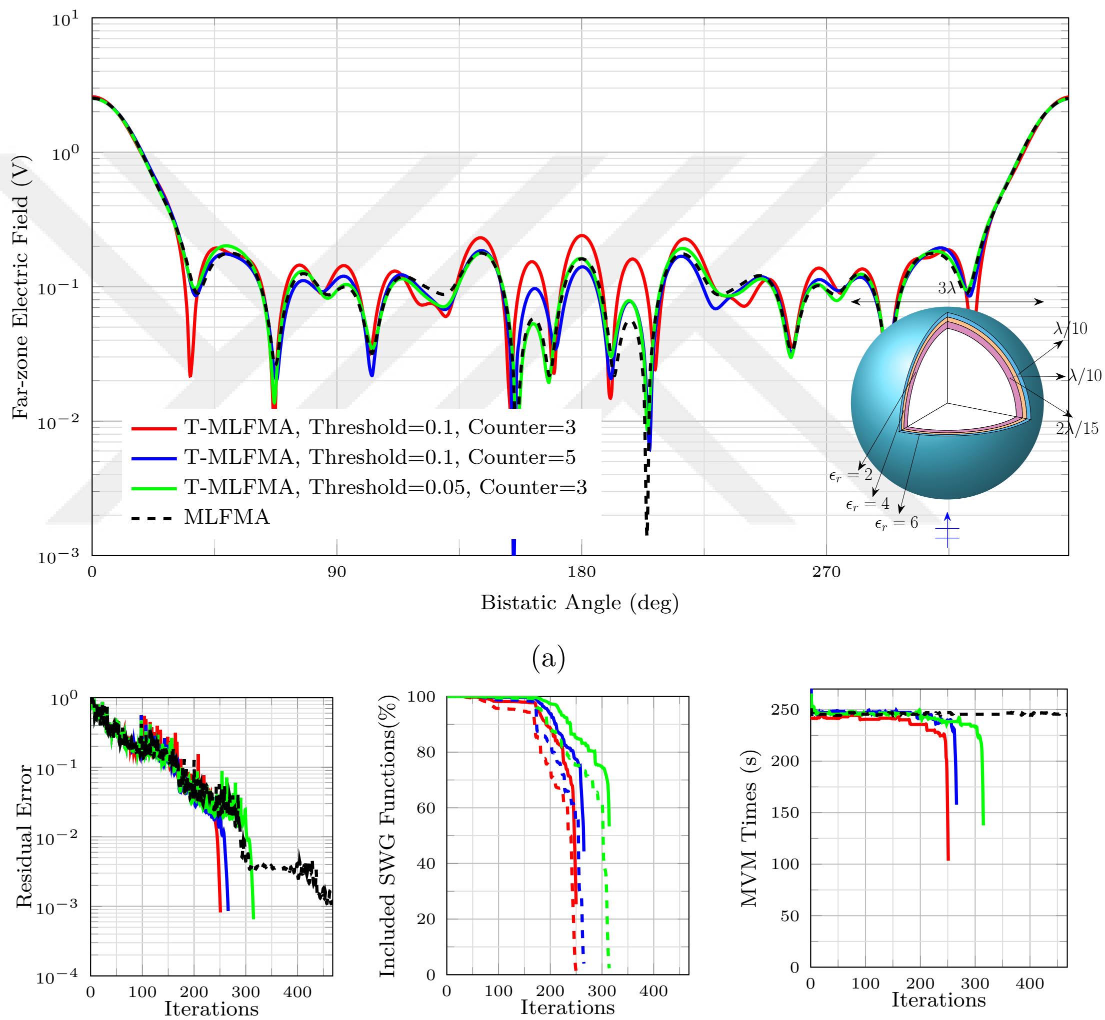

Figure 4.13: (a) The scattered electric field of the 3 layer shell geometry with the outermost diameter is 3λ, and with $2\lambda/15$, $\lambda/10$ and $\lambda/10$ thicknesses and ϵ_r values 6, 4 and 2, respectively, from outer to inner, obtained with MLFMA and T-MLFMA for different threshold and counter values, (b) residual errors, (c) included SWG functions, and (d) MVM time at each iteration

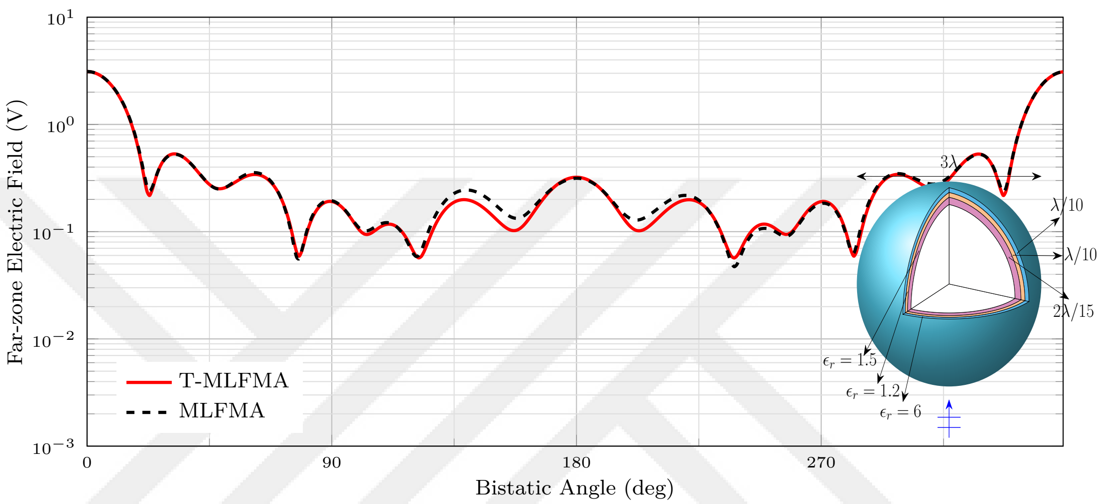

(a)

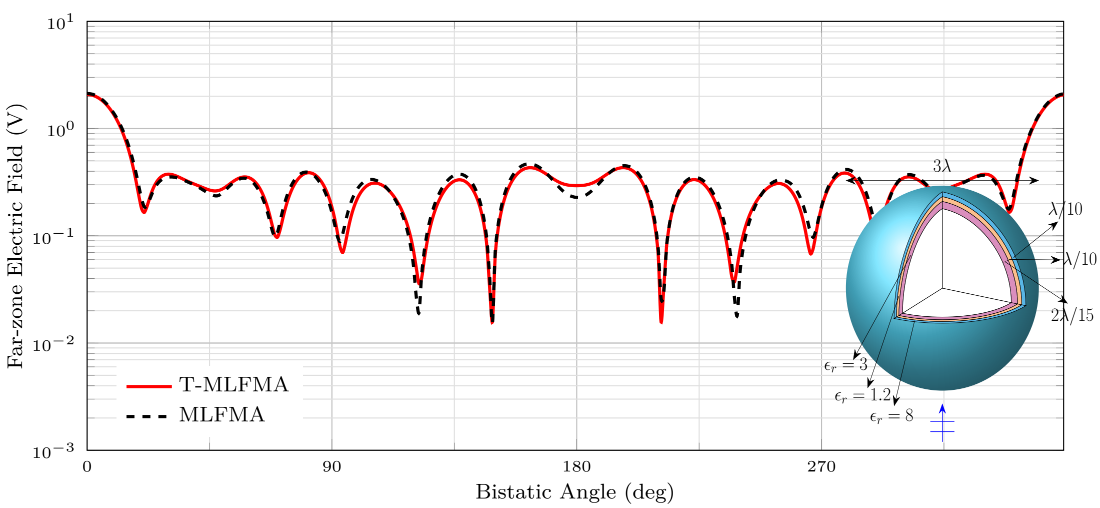

(b)

Figure 4.14: (a) The scattered electric field of the 3 layer shell geometry with a 3λ outermost diameter with $2\lambda/15$, $\lambda/10$ and $\lambda/10$ thicknesses and (a) ϵ_r values 6, 1.2 and 1.5, respectively, from outer to inner and (b) ϵ_r values 8, 1.2 and 3, respectively, from outer to inner, obtained with MLFMA and T-MLFMA with BTET = TTET = 0.1 and BTC = TTC = 3

Table 4.13: Numerical results of MLFMA and T-MLFMA for the scattering from the 3 layer shell geometries with a 3λ outermost diameter with $2\lambda/15$, $\lambda/10$ and $\lambda/10$ thicknesses and ϵ_r values 6, 1.2 and 1.5, from outer to inner and ϵ_r values 8, 1.2 and 3, from outer to inner at 1 GHz

	ϵ_r	BTET and TTET	BTC and TTC	Number of Iterations	MVM Time (s)	Error (%)
MLFMA	6-1.2-1.5	-	-	280	60401	-
T-MLFMA		0.1	3	134	27600	2.17
MLFMA	8-1.2-3	-	-	577	131275	-
T-MLFMA		0.1	3	236	48994	5.19

cone, which has a λ diameter and λ height with $\epsilon_r = 5$. The operating frequency is 1 GHz ($\lambda = 0.3$ m). The object is discretized with 453,762 SWG functions. Scattered far-zone electric field, residual errors and MVM times in each iteration obtained from T-MLFMA are compared with that of the conventional MLFMA. The numerical results are depicted in Fig. 4.15 for 3 different threshold values of 0.1, 0.05, and 0.03 in red, blue and green colors, respectively. TTC and BTC values are set to 3. The details of the numerical results are tabulated in Table 4.14. For the threshold value of 0.1, the number of iterations are reduced from 56 to 33 and MVM time drops from 1170 seconds to 641 seconds (1.82 times speed-up) with a far-field error 9.28% with respect to the conventional MLFMA. However, for the threshold values of 0.05 and 0.03, more accurate results are obtained for the scattered far-field with far-field errors 5.81% and 2.76%, respectively. Moreover, T-MLFMA provides 1.52 and 1.41 times speed-up for the threshold values of 0.05 and 0.03, respectively.

Table 4.14: Numerical results obtained with MLFMA and T-MLFMA for different threshold values for the scattering from homogeneous cone with a λ diameter and λ height with $\epsilon_r = 5$ at 1 GHz

	BTET and TTET Value	Number Of Iterations	MVM Time (s)	Error (%)
MLFMA	-	56	1170	-
T-MLFMA	0.1	33	641	9.28
	0.05	38	767	5.81
	0.03	40	828	2.76

Next, we set BTET and TTET values to 0.1, BTC and TTC values to 3 for another set of cone geometry simulations. The trimming is applied for both basis

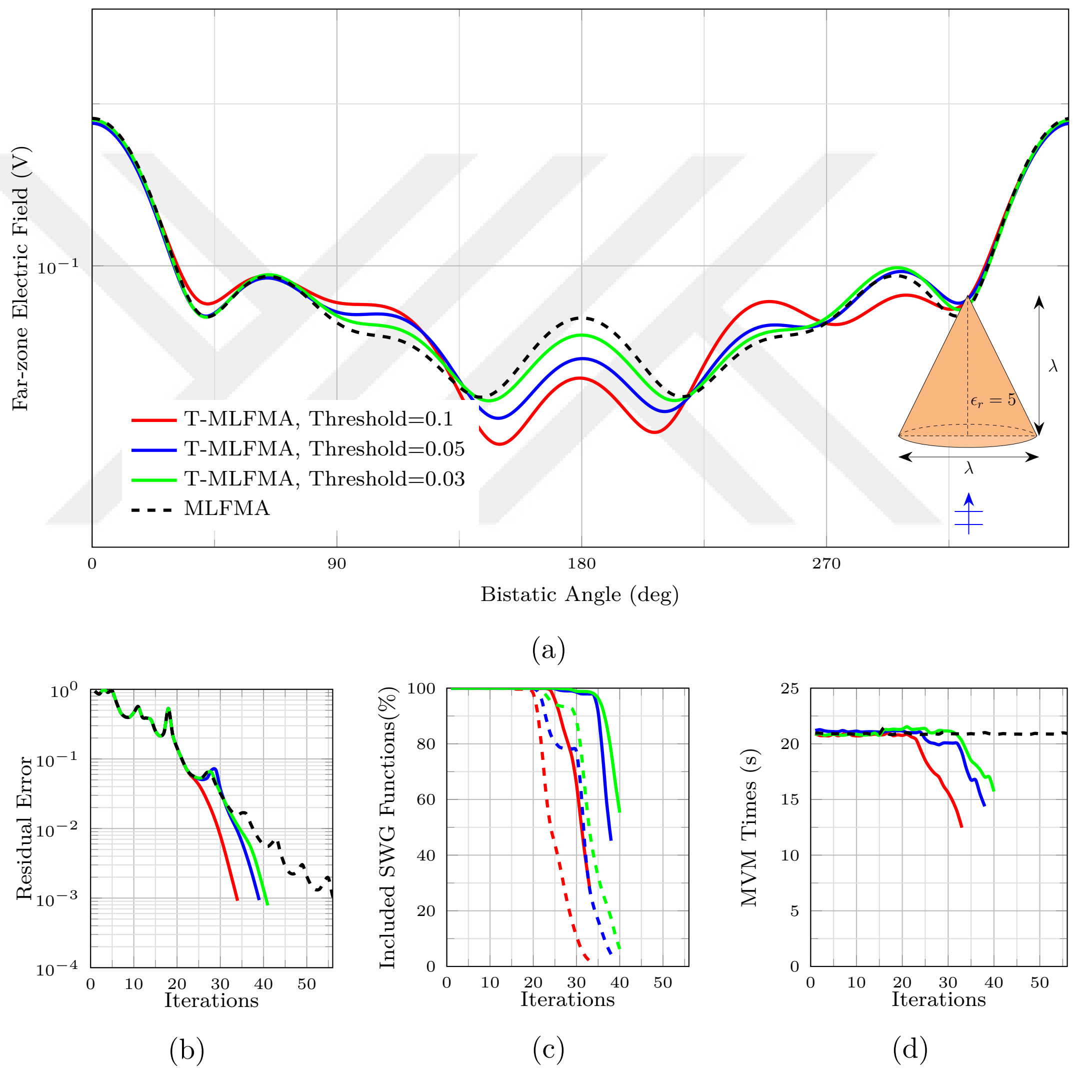

Figure 4.15: (a) The scattered electric field of homogeneous cone with a λ diameter and λ height with $\epsilon_r = 5$, obtained with MLFMA and T-MLFMA for different Basis-Testing Trimming Error Threshold Values with BTC = TTC = 3, (b) residual errors, (c) included SWG functions, and (d) MVM time at each iteration

and testing. Similar to the previous case, scattering from a homogeneous cone with ϵ_r value of 3 is performed. The cone has a λ diameter and λ height. The object is discretized with 121,994 SWG functions. Scattered far-fields obtained from MLFMA and T-MLFMA are compared in Fig. 4.16(a). The details of T-MLFMA and MLFMA numerical results are presented in Table 4.15. T-MLFMA provides 1.47 times speed-up in MVM times and scattered far-field results show high accuracy with far-field error 1.28%. Similarly, a larger homogeneous cone with a 2λ diameter and 2λ height is considered. The object, again, has $\epsilon_r = 3$. This object is discretized with 693,438 SWG functions. Scattered far-fields obtained from MLFMA and T-MLFMA are compared in Fig. 4.16(b). The T-MLFMA and MLFMA numerical results are presented in Table 4.15. T-MLFMA provides 1.75 times speed-up in MVM times and scattered far-field results show high accuracy with the far-field error 2.49%.

Table 4.15: Numerical results obtained from MLFMA and T-MLFMA for different threshold values for the scattering from homogeneous cones with a λ diameter, λ height and a 2λ diameter, 2λ height with $\epsilon_r = 3$ at 1 GHz

	Diameter	Height	Number of Iterations	MVM Time (s)	Error (%)
MLFMA	λ	λ	22	236	-
T-MLFMA			17	162	1.28
MLFMA	2λ	2λ	79	12888	-
T-MLFMA			47	7426	2.49

Homogeneous Torus Results: After analyzing the T-MLFMA results for the cone geometry, we present T-MLFMA results for various dielectric torus geometries. In the first simulation, the inner radius of the torus is $\lambda/3$ and the outer radius is $2\lambda/3$ with $\epsilon_r = 3$. The operating frequency is 1 GHz ($\lambda = 0.3$ m). The object is discretized with 122,567 SWG functions. Scattered far-zone electric field, residual errors and MVM times in each iteration obtained from T-MLFMA are compared with that of the conventional MLFMA. The numerical results are depicted in Fig. 4.17 for 3 different threshold values of 0.3, 0.2, and 0.1 in red, blue and green colors, respectively. TTC and BTC values are set to 3. Moreover, the details of numerical results are tabulated in Table 4.16. For the threshold value of 0.1, the number of iterations are reduced from 20 to 16 and MVM time drops from 140 seconds to 98 seconds with a significantly high accuracy for the scattered

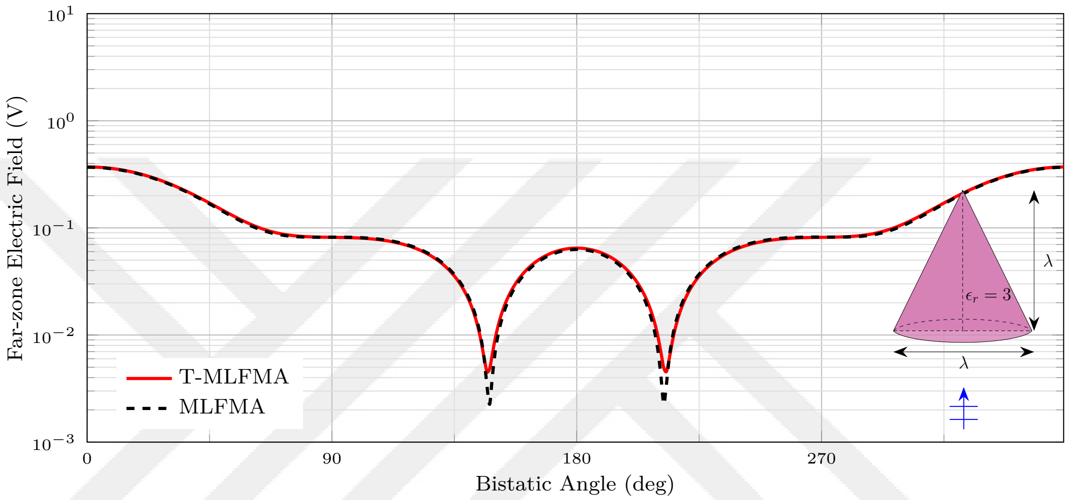

(a)

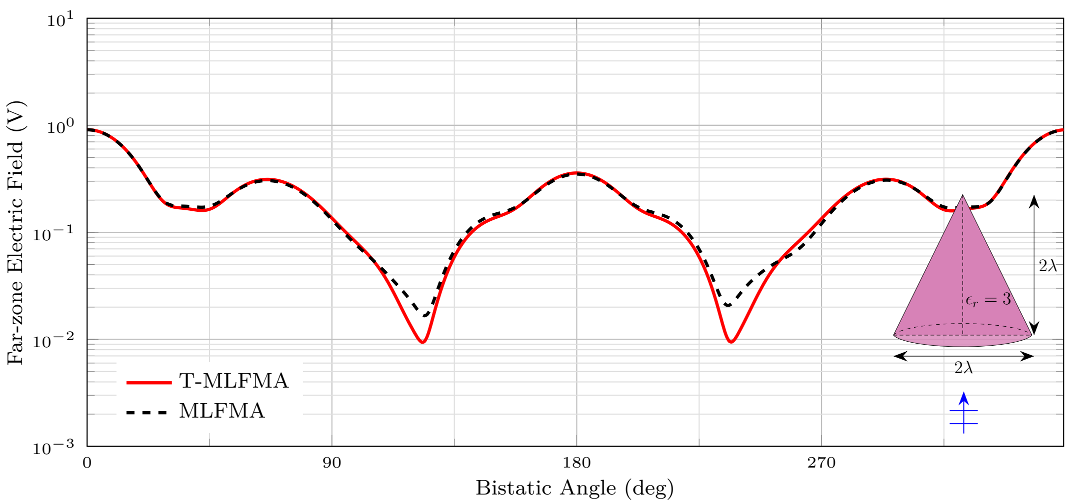

(b)

Figure 4.16: The scattered electric field of the homogeneous cone with (a) λ diameter and λ height with $\epsilon_r = 3$, (b) 2λ diameter and 2λ height with $\epsilon_r = 3$ obtained from MLFMA and T-MLFMA with BTET = TTET = 0.1 and BTC = TTC = 3

far-field. Moreover, the number of iterations are reduced to 15 and MVM time drops to 77 seconds (1.82 times speed-up) for the threshold value of 0.3 with the far-field error 1.78%.

Table 4.16: Numerical results obtained from MLFMA and T-MLFMA for different threshold values for the scattering from a homogeneous torus with a $\lambda/3$ inner radius and $2\lambda/3$ outer radius with $\epsilon_r = 3$ at 1 GHz

	BTET and TTET Value	Number Of Iterations	MVM Time (s)	Error (%)
MLFMA	-	20	140	-
T-MLFMA	0.3	15	77	1.78
	0.2	16	79	1.04
	0.1	16	98	0.50

Table 4.17: Numerical results of MLFMA and T-MLFMA for different threshold values for the scattering from the homogeneous torus with $\lambda/2$ inner radius and $3\lambda/2$ outer radius with $\epsilon_r = 5$ at 1 GHz

	BTET and TTET Value	Number Of Iterations	MVM Time (s)	Error (%)
MLFMA	-	1192	143563	-
T-MLFMA	0.1	209	25048	8.09
	0.05	317	37801	5.27
	0.03	370	44527	4.70

Next, we consider another homogeneous torus geometry with $\lambda/2$ inner radius and $3\lambda/2$ outer radius, and $\epsilon_r = 5$ at the same frequency (1 GHz). The object is discretized with 1,220,774 SWG functions. Scattered far-zone electric field, residual errors and MVM times in each iteration obtained from T-MLFMA are compared with that of the conventional MLFMA. The numerical results are shown in Fig. 4.18 for 3 different threshold values of 0.1, 0.05, and 0.03 in red, blue and green colors, respectively. TTC and BTC values are set to 5. Moreover, Table 4.17 tabulated the details of the numerical results. For the threshold value of 0.03, the number of iterations are reduced from 1192 to 370 and MVM time drops from 143563 seconds to 44527 seconds (3.3 times speed-up) with a 4.70% far-field error with respect to conventional MLFMA. Moreover, for the threshold value of 0.1, the number of iterations are reduced to 209 and MVM time drops to 25048 seconds (5.8 times speed-up) with a far-field error of 8.09%. Considering this result and the result for the torus geometry with $\epsilon_r = 3$, we can conclude

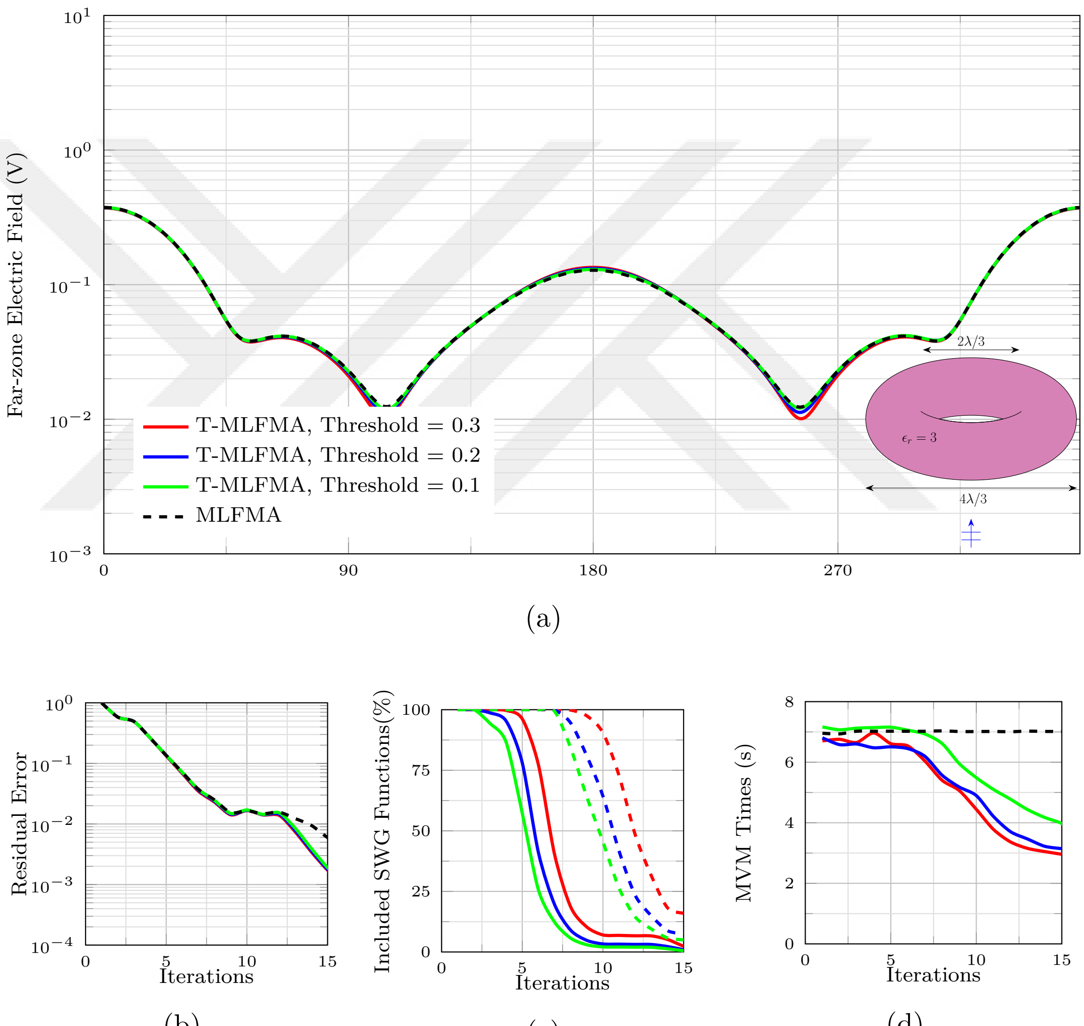

Figure 4.17: (a) The scattered electric field of the homogeneous torus with a $\lambda/3$ inner radius and $2\lambda/3$ outer radius with $\epsilon_r = 3$ obtained with MLFMA and T-MLFMA for different Basis-Testing Trimming Error Threshold Values with BTC = TTC = 3, (b) residual errors, (c) included SWG functions, and (d) MVM time at each iteration

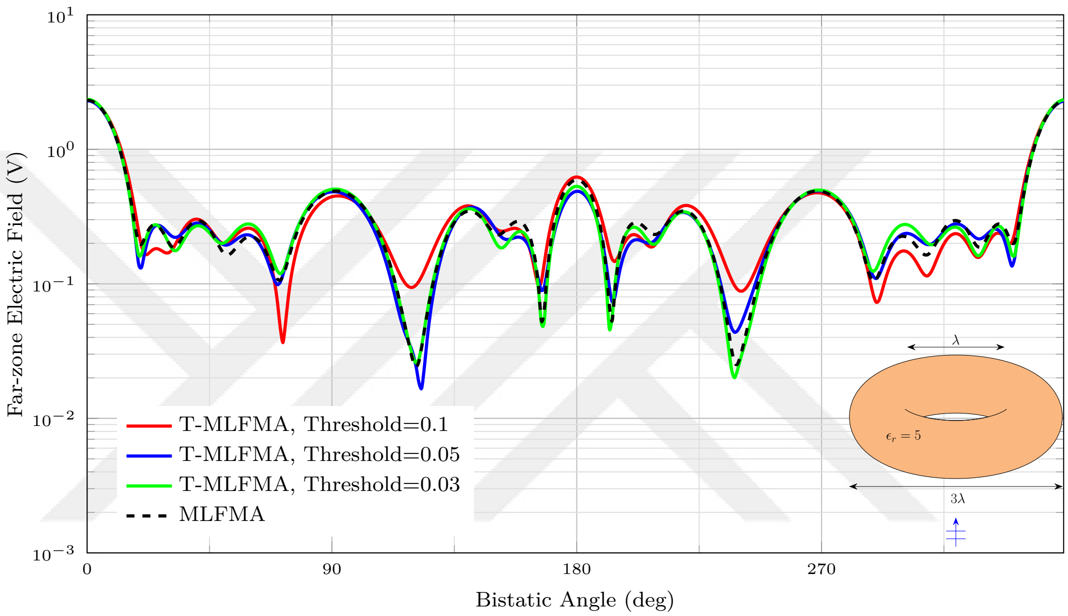

(a)

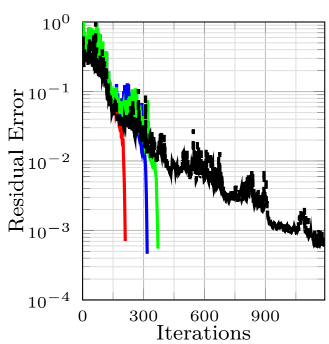

(b)

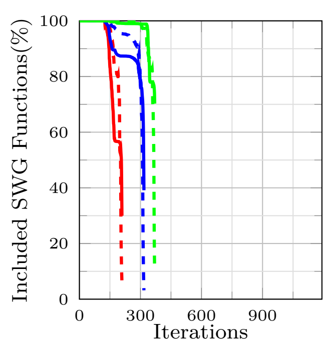

(c)

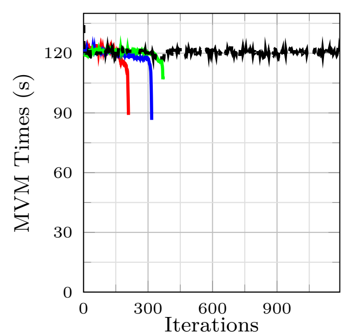

(d)

Figure 4.18: (a) The scattered electric field of the homogeneous torus with a $\lambda/2$ inner radius and $3\lambda/2$ outer radius with $\epsilon_r = 5$ obtained from MLFMA and T-MLFMA for different Basis-Testing Trimming Error Threshold Values with BTC = TTC = 3, (b) residual errors, (c) included SWG functions, and (d) MVM time at each iteration

that lower trimming threshold and larger trimming counter values are required to achieve smaller far-field error for larger values of ϵ_r.

After investigating the performance of T-MLFMA for two torus geometries with different ϵ_r values, we set BTET and TTET values to 0.1, BTC and TTC values to 3 for another set of torus geometry simulations. The trimming is applied for both basis and testing. As the first simulation, scattering from a homogeneous torus object with $\lambda/3$ inner radius and $2\lambda/3$ outer radius with $\epsilon_r = 6$ is performed. The object is discretized with 122,567 SWG functions. Scattered far-fields obtained with MLFMA and T-MLFMA are compared in Fig. 4.19(a). The details T-MLFMA and MLFMA numerical results are tabulated in Table 4.18. T-MLFMA provides 2.5 times speed-up in MVM times and scattered far-field results are accurate with a far-field error of 2.17%. As the second example, a larger torus object with λ inner radius and 2λ outer radius with $\epsilon_r = 3$ is considered. This object is discretized with 1,988,043 SWG functions. Scattered far-fields obtained with MLFMA and T-MLFMA are compared in Fig. 4.19(b). The details of T-MLFMA and MLFMA numerical results are presented also in Table 4.18. T-MLFMA provides 4.52 times speed-up in MVM times and highly accurate scattered far-field results are obtained with a far-field error of 1.35%.

Table 4.18: Numerical results obtained with MLFMA and T-MLFMA for the scattering from a homogeneous torus with a $\lambda/3$ inner radius, $2\lambda/3$ outer radius with $\epsilon_r = 6$ and with a λ inner radius, 2λ outer radius with $\epsilon_r = 3$ at 1 GHz

	Inner Radius	Outer Radius	ϵ_r	Number of Iterations	MVM Time (s)	Error (%)
MLFMA	$\lambda/3$	$2\lambda/3$	6	90	506	-
T-MLFMA				48	200	2.17
MLFMA	λ	2λ	3	358	353795	-
T-MLFMA				82	78244	1.35

Homogeneous Cylinder Results: We present numerical results this time for a homogeneous dielectric cylinder. The diameter and the height of the cylinder is λ and 2λ, respectively, with $\epsilon_r = 5$. The operating frequency is 1 GHz ($\lambda = 0.3$ m). The object is discretized with 1,389,170 SWG functions. Scattered far-zone electric field, residual errors and MVM times in each iteration obtained from T-MLFMA are compared with that of the conventional MLFMA. The numerical

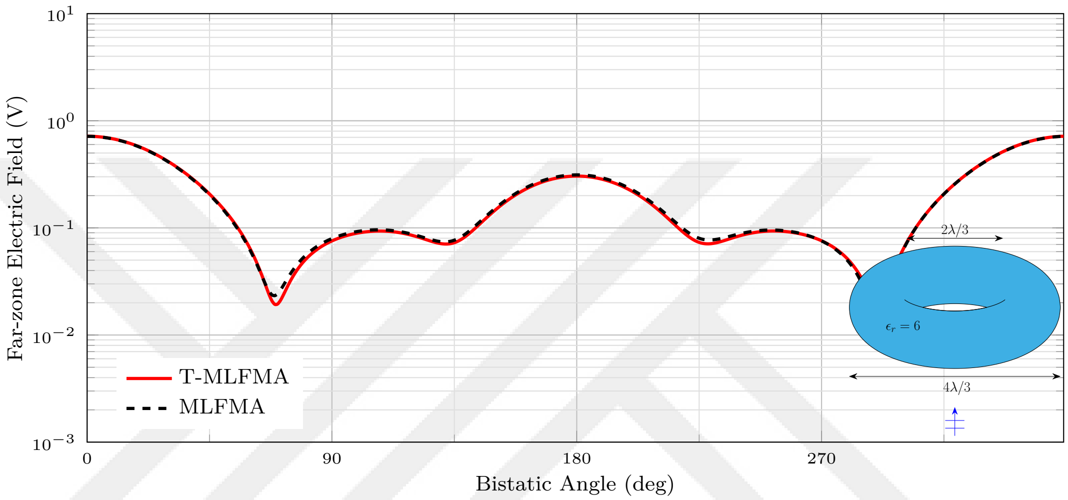

(a)

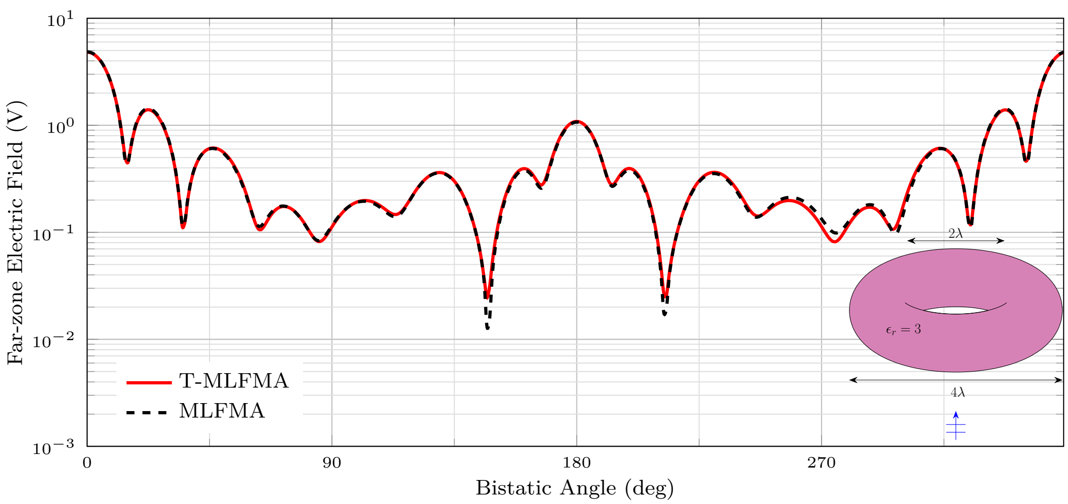

(b)

Figure 4.19: The scattered electric field of a homogeneous torus (a) with a $\lambda/3$ inner radius and $2\lambda/3$ outer radius with $\epsilon_r = 6$, (b) with a λ inner radius and 2λ outer radius with $\epsilon_r = 3$, obtained with MLFMA and T-MLFMA with BTET = TTET = 0.1 and BTC = TTC = 3

results are depicted in Fig. 4.20 for 3 different threshold values of 0.1, 0.05, and 0.03 in red, blue and green colors, respectively. TTC and BTC values are set to 5. Moreover, the details of numerical results are tabulated in Table 4.19. For the threshold value of 0.1, the number of iterations are reduced from 266 to 164 and MVM time drops from 32478 seconds to 19502 seconds (1.67 times speed-up) with a 27.25% far-field error with respect to the conventional MLFMA. On the other hand, the number of iterations are 203 and 206, and MVM times are obtained as 24425 seconds (1.34 times speed-up) and 24757 seconds (1.32 times speed-up) for the threshold values of 0.05 and 0.03, respectively. We obtain significantly more accurate results for the threshold value of 0.03 with a far-field error of 3.51%.

Table 4.19: Numerical results obtained with MLFMA and T-MLFMA for different threshold values for the scattering from a homogeneous cylinder with λ diameter and 2λ height with ϵ_r = 5 at 1 GHz

	BTET and TTET Value	Number Of Iterations	MVM Time (s)	Error (%)
MLFMA	-	266	32478	-
T-MLFMA	0.1	164	24425	27.25
	0.05	203	24757	14.70
	0.03	206	32478	3.51

Inhomogeneous Cylinder Results: Next, we consider inhomogeneous cylinder geometries. The first geometry, the object involves two concentric cylinders with a $\lambda/4$ diameter and $\lambda/4$ height for the inner cylinder, and a $\lambda/2$ diameter and $\lambda/2$ height for the outer cylinder. The inner and outer cylinders have $\epsilon_r = 6$ and $\epsilon_r = 3$, respectively. The operating frequency is 1 GHz ($\lambda = 0.3$ m). The object is dicretized with 74,432 SWG functions by considering the mesh mating conditions. Scattered far-zone electric field, residual errors and MVM times in each iteration obtained from T-MLFMA are compared with that of the conventional MLFMA. The numerical results are depicted in Fig. 4.21 for 3 different threshold values of 0.2, 0.1, and 0.05 in red, blue and green colors, respectively. TTC and BTC values are set to 5. Moreover, the details of the numerical results are tabulated in Table 4.20. The number of iterations are reduced from 48 to 38 and MVM time drops from 996 seconds to 502 seconds (approximately two-fold acceleration) with a 4.82% far-field error with respect to the conventional MLFMA for the threshold value of 0.2. On the other hand, the number of iterations are obtained as 39 and

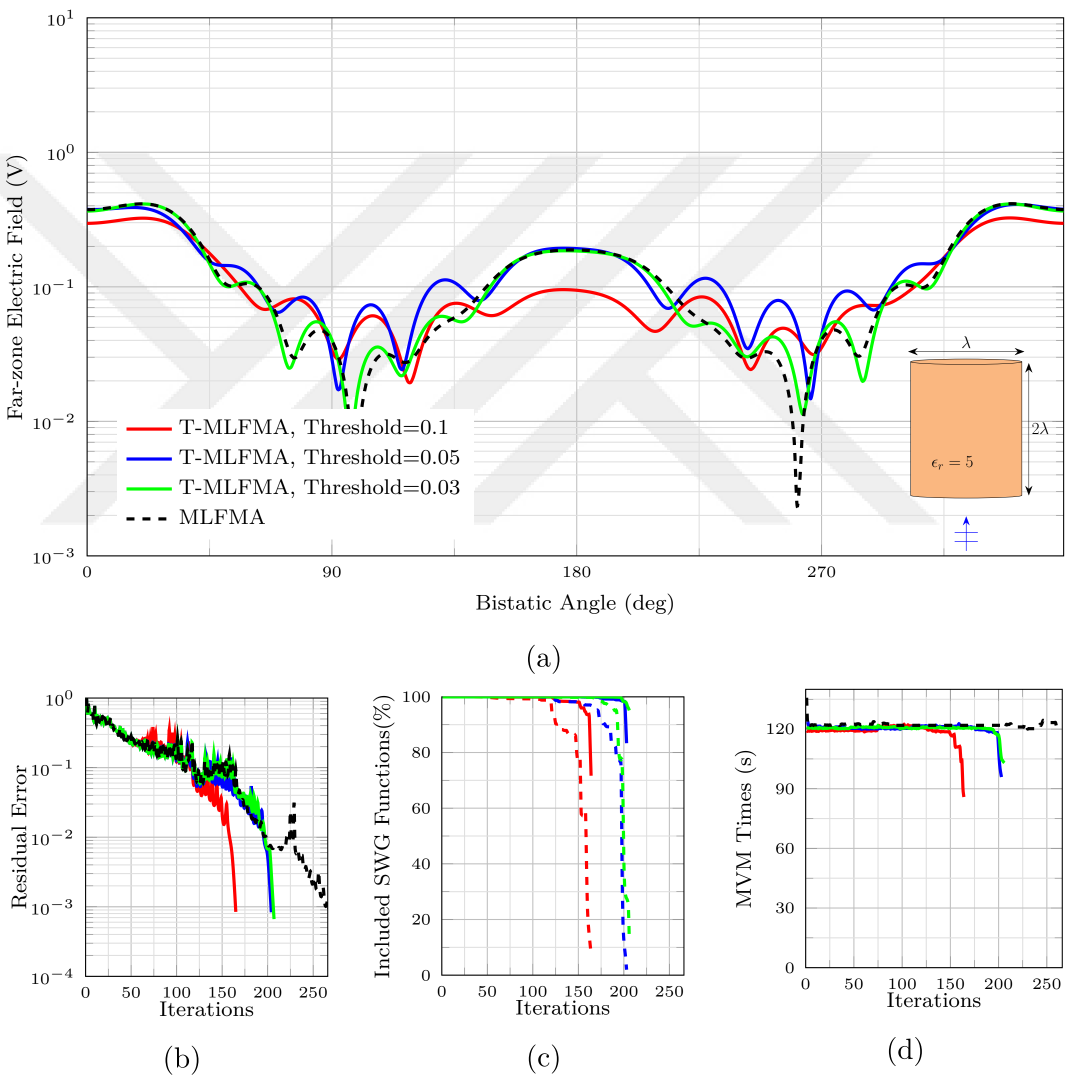

Figure 4.20: (a) The scattered electric field of a homogeneous cylinder with λ diameter and 2λ height with $\epsilon_r = 5$ obtained with MLFMA and T-MLFMA for different Basis-Testing Trimming Error Threshold Values with BTC = TTC = 3, (b) residual errors, (c) included SWG functions, and (d) MVM time at each iteration

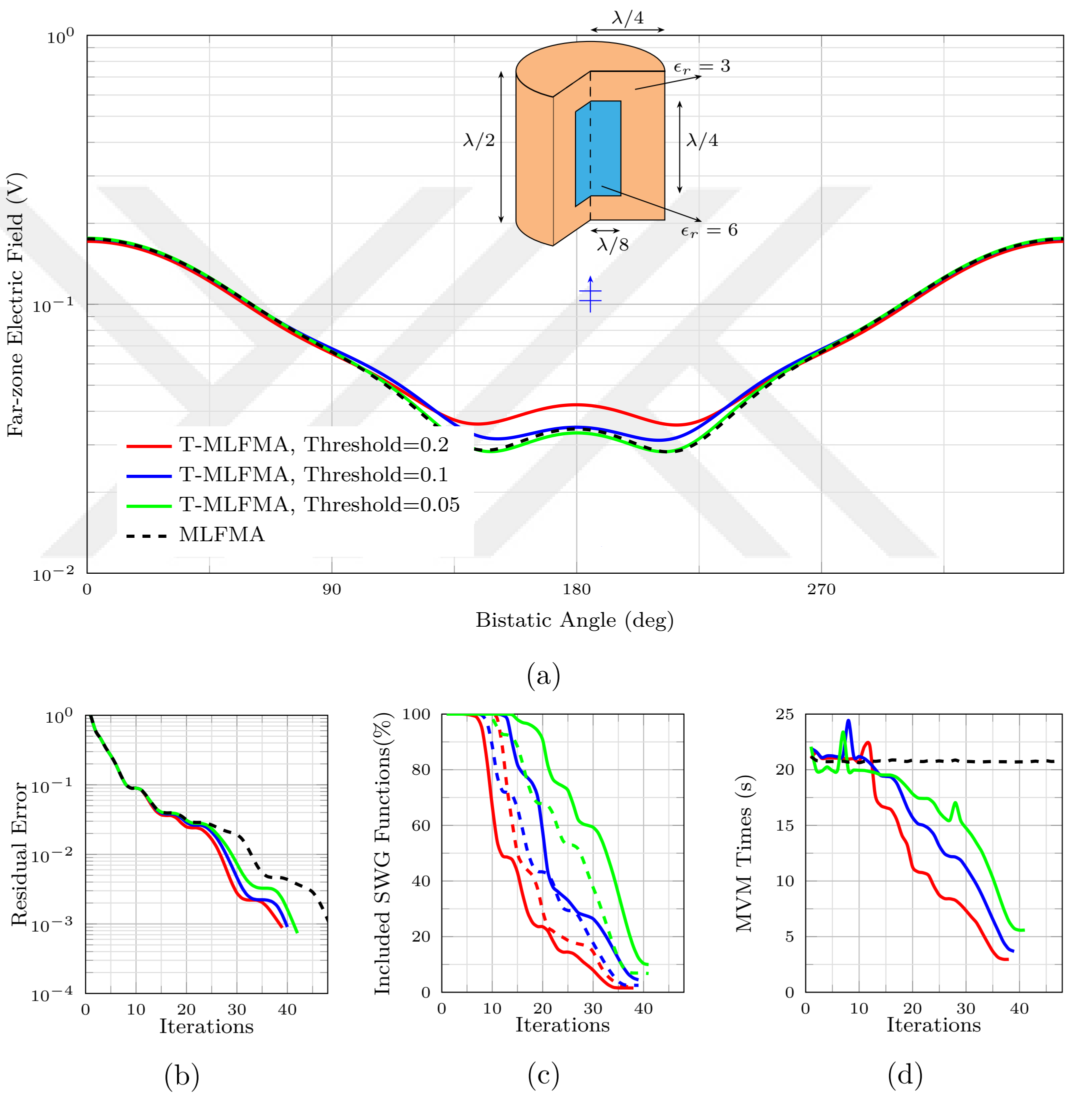

Figure 4.21: (a) The scattered electric field of two concentric cylinders, where the inner cylinder has a $\lambda/4$ diameter and $\lambda/4$ height with $\epsilon_r = 6$ and the outer cylinderical shell has a $\lambda/2$ diameter and $\lambda/2$ height with $\epsilon_r = 3$, obtained with MLFMA and T-MLFMA for different Basis-Testing Trimming Error Threshold Values with BTC = TTC = 5, (b) residual errors, (c) included SWG functions, and (d) MVM time at each iteration

41, and MVM times are obtained as 597 seconds (1.67 times speed-up) and 663 seconds (1.50 times speed-up) for the threshold values of 0.1 and 0.05, respectively. We obtain significantly more accurate results for the threshold value of 0.05 with the far-field error 0.75%.

Table 4.20: Numerical results obtained with MLFMA and T-MLFMA for different threshold values for the scattering from two concentric cylinders, where the inner cylinder has a $\lambda/4$ diameter and $\lambda/4$ height with $\epsilon_r = 6$, and the outer cylinderical shell has a $\lambda/2$ diameter and $\lambda/2$ height with $\epsilon_r = 3$ at 1 GHz

	BTET and TTET Value	Number Of Iterations	MVM Time (s)	Error (%)
MLFMA	-	48	996	-
T-MLFMA	0.2	38	502	4.82
	0.1	39	597	2.30
	0.05	41	663	0.75

Table 4.21: Numerical results of MLFMA and T-MLFMA for different threshold values for the scattering from the concentric cylinders, where inner cylinder has $\lambda/2$ diameter and $\lambda/2$ height with $\epsilon_r = 4$ and outer cylindrical shell has λ diameter and λ height with $\epsilon_r = 2.2$ at 1 GHz

	BTET and TTET Value	Number Of Iterations	MVM Time (s)	Error (%)
MLFMA	-	290	108611	-
T-MLFMA	0.1	116	25935	7.56
	0.05	151	41443	6.71
	0.01	228	65872	1.18

As a second example for the inhomogeneous cylinder case, we again consider, two concentric cylinders but with a $\lambda/2$ diameter and $\lambda/2$ height for the inner cylinder, and a λ diameter and λ height for the outer cylinder. The inner and outer cylinders have $\epsilon_r = 4$ and $\epsilon_r = 2.2$, respectively. The object is dicretized with 505,072 SWG functions by considering the mesh mating conditions which ensure smooth transitions in meshing at the border of the two regions. Scattered far-zone electric field, residual errors and MVM times in each iteration obtained from T-MLFMA are compared with that of the conventional MLFMA. The operating frequency is 1 GHz ($\lambda = 0.3$ m). Fig. 4.22 shows the numerical results for 3 different threshold values of 0.1, 0.05, and 0.01 in red, blue and green colors, respectively. TTC and BTC values are set to 5. Moreover, the details of numerical results can be seen in Table 4.21. We present approximately 4 times acceleration

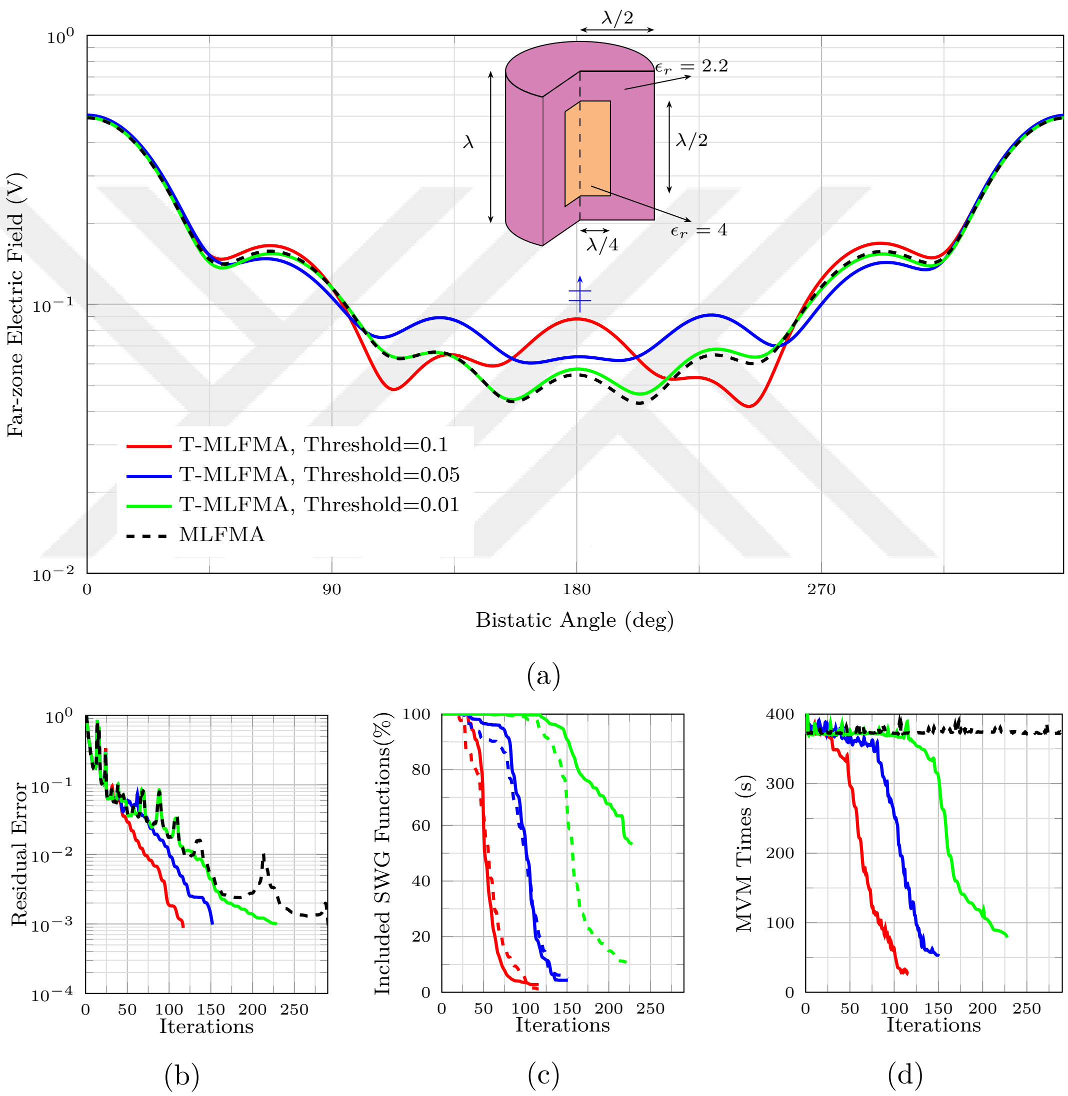

Figure 4.22: (a) The scattered electric field of two concentric cylinders, where the inner cylinder has a $\lambda/2$ diameter and $\lambda/2$ height with $\epsilon_r = 4$, and the outer cylinderical shell has a λ diameter and λ height with $\epsilon_r = 2.2$, obtained with MLFMA and T-MLFMA for different Basis-Testing Trimming Error Threshold Values with BTC = TTC = 5, (b) residual errors, (c) included SWG functions, and (d) MVM time at each iteration

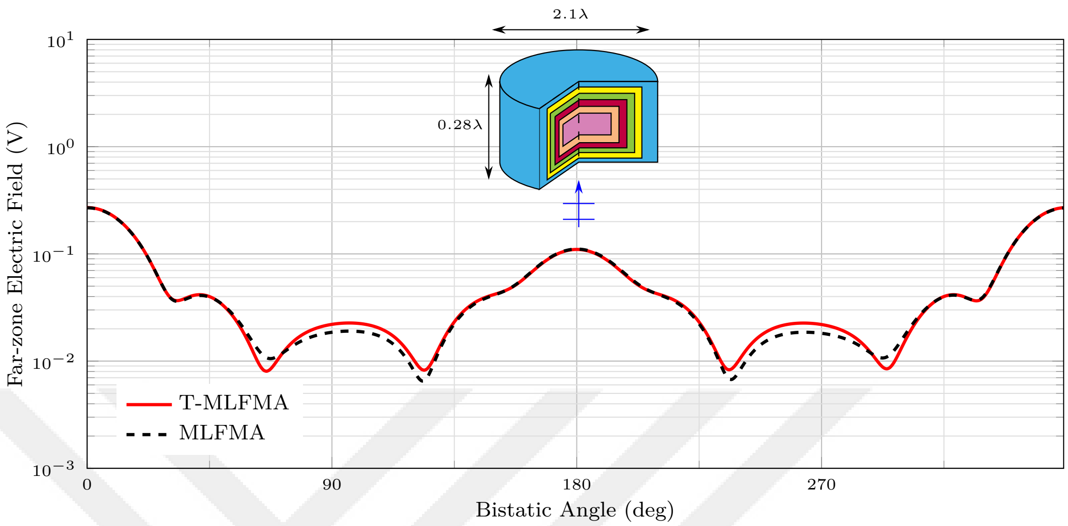

Figure 4.23: The scattered electric field of cylindrical Luneburg lens with BTET = TTET = 0.01 and BTC = TTC = 5, sizes and ϵ_r value of each layer are tabulated in Table 4.22

for the threshold value of 0.1 with a far-field error of 7.56%. However, we achieve more accurate results for the threshold values of 0.05 and 0.01 with 6.71% and 1.18% far-field error values with respect to the conventional MLFMA, and 2.60 and 1.65 times speed-ups in MVM times, respectively.

Next, we consider a cylindrical Luneburg lens as a significantly more challenging geometry which involves 6 different concentric dielectric layers [40] as sketched at the in set of in Fig 4.23 and sizes of these layers are tabulated in Table 4.22. ϵ_r values of layers are 12, 10, 8, 6, 4 and 2 from inner to outer. The object is discretized with 777,612 SWG functions by considering the mesh mating conditions at the border of any of the two regions, and the operating frequency is 7 GHz (λ=0.0428 m). Scattered far-fields for MLFMA and T-MLFMA are compared in Fig. 4.23. The trimming is applied for both basis and testing, and BTET and TTET have the same value of 0.01, whereas BTC and TTC values are set to 5 for T-MLFMA simulation. With T-MLFMA, the number of iterations are decreased from 432 to 327, and MVM times drops from 22009 seconds to 15242 seconds. T-MLFMA provides approximately 1.5 times speed-up in MVM times and the scattered far-field results are accurate with a far-field error of 2.20% with respect to MLFMA result.

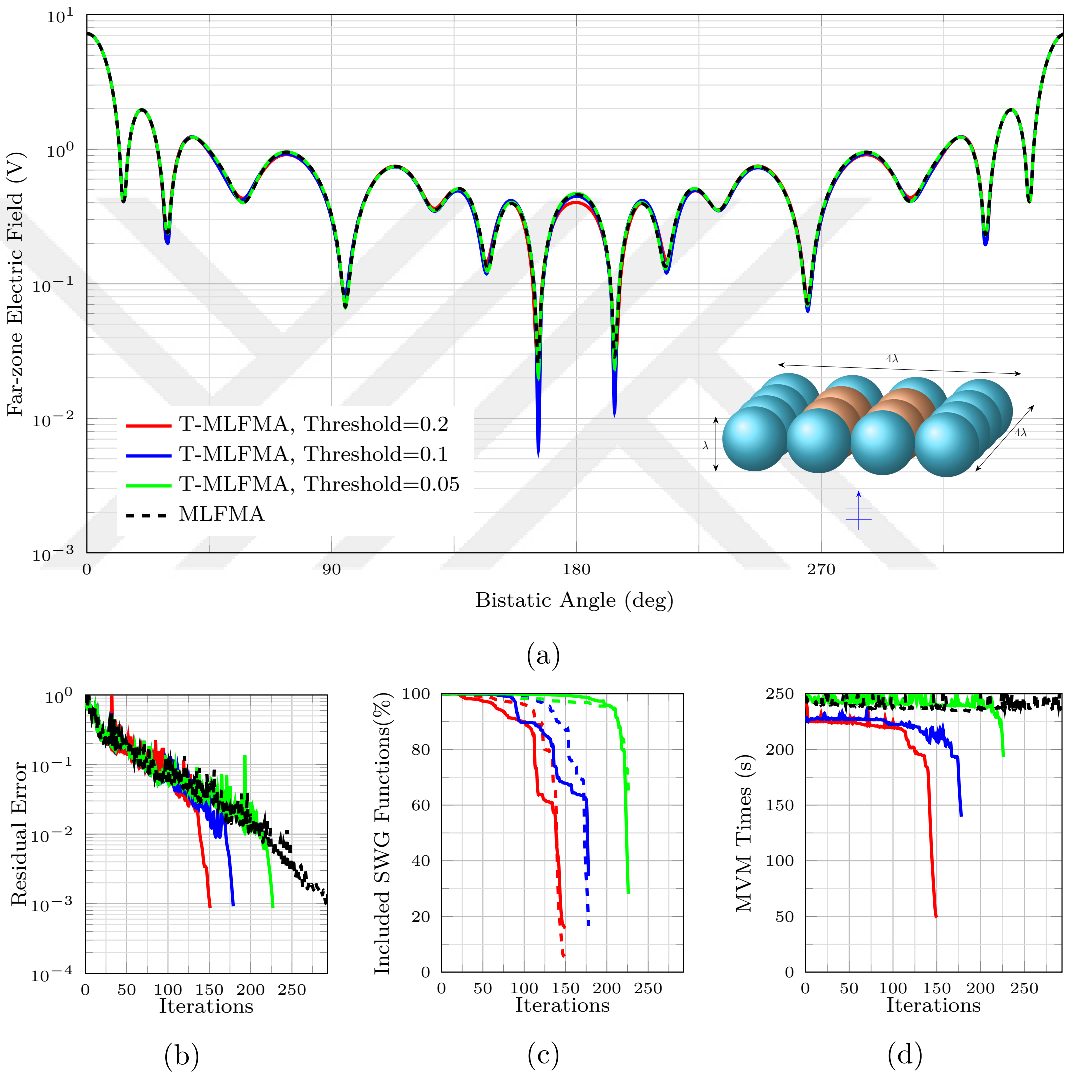

Figure 4.24: (a) The scattered electric field of an array of inhomogeneous spheres (each has λ diameter and ϵ_r value in each sphere is linearly decreasing from the center of each sphere to the surface in z direction, 4 spheres around the origin have $\epsilon_r = 2.5$ at z = 0 and $\epsilon_r = 1.5$ at z = $\pm$radius and remaining spheres have $\epsilon_r = 3.5$ at z = 0 and $\epsilon_r = 2.5$ at z = $\pm$radius). Results are obtained with MLFMA and T-MLFMA for different Basis-Testing Trimming Error Threshold Values with BTC = TTC = 5, (b) residual errors, (c) included SWG functions, and (d) MVM time at each iteration

Table 4.22: Sizes and ϵ_r values of each layer of cylindrical Luneburg lens

Cylinder Number	Diameter (mm)	Height (mm)	ϵ_r
1 (Innermost)	31.2	3.32	12
2	53.2	6.62	10
3	69.7	8.8	8
4	76.5	11	6
5	89.1	12.4	4
6 (Outermost)	95.4	13.8	2

Inhomogeneous Full-Sphere Array Results: The next numerical example is an array of dielectric spheres, we increased the size of the problem by creating array of spheres. The array consists of 16 dielectric spheres, which are placed side by side on xy-plane in the form of a 4x4 array. The diameter of each sphere is λ and the ϵ_r value inside of each sphere is decreasing linearly from the center of the each sphere to surface of the each sphere in z-direction. 4 spheres around the origin are shown in apricot color, the ϵ_r value inside the sphere is decreasing from 2.5 to 1.5 while the absolute value of the distance to the center of sphere in z-direction is increasing up to the radius. For the remaining spheres, the ϵ_r value inside the sphere is decreasing from 3.5 to 2.5 while the absolute value of the distance to the center of sphere in z-direction is increasing up to the radius. The array is dicretized with 922,362 SWG functions. Scattered far-zone electric field, residual errors and MVM times in each iteration obtained from T-MLFMA are compared with that of the conventional MLFMA. The numerical results are depicted in Fig. 4.24 for 3 different threshold values of 0.2, 0.1, and 0.05 in red, blue and green colors, respectively. TTC and BTC values are set to 5 and Table 4.23 presents the details of the numerical results. We obtain approximately 2.3 times speed-up for the threshold value of 0.2 with a far-field error of 1.48% with respect to MLFMA result. However, we achieve more accurate results for the threshold values of 0.1 and 0.05 with 1.25% and 0.32% far-field error values, respectively, obtaining 1.80 and 1.28 times speed-ups in MVM times.

Inhomogeneous Cone Array Results: We consider another type of array which consists of 16 dielectric cones, and similar to the array of dielectric spheres they are placed on xy plane in the form of a 4x4 array. The diameter and height of

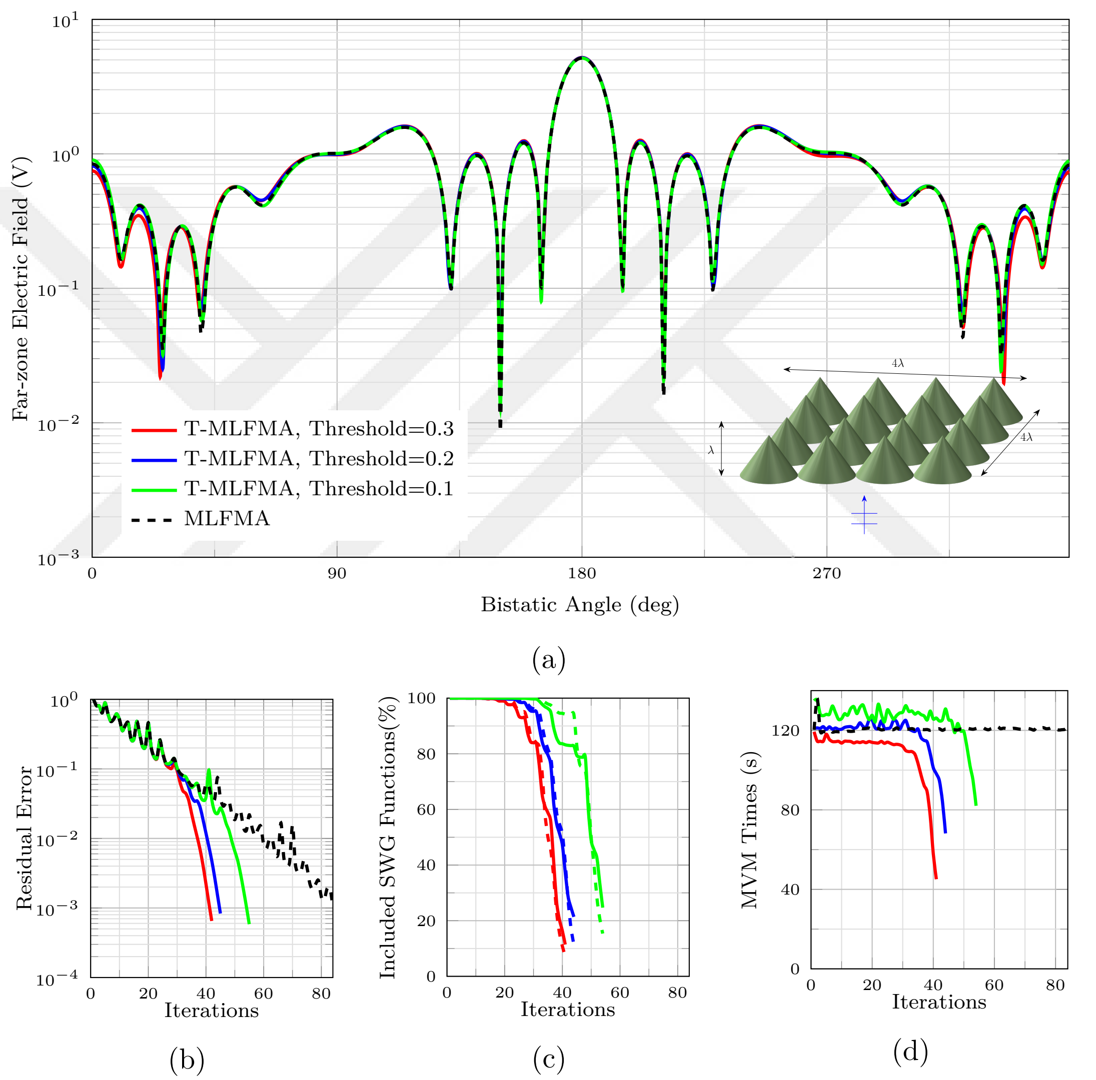

Figure 4.25: (a) The scattered electric field of the array of inhomogeneous cones (each has λ diameter and λ height and ϵ_r value in each cone is linearly decreasing from the tip of the each cone to the base in the z-direction, each cone has $\epsilon_r = 7.5$ at the tip and $\epsilon_r = 1.5$ at the base) obtained with MLFMA and T-MLFMA for different Basis-Testing Trimming Error Threshold Values with BTC = TTC = 3, (b) residual errors, (c) included SWG functions, and (d) MVM time at each iteration

Table 4.23: Numerical results of MLFMA and T-MLFMA for different threshold values for the array of inhomogeneous spheres (each has λ diameter and ϵ_r value inside of each sphere is decreasing linearly from the center of the each sphere to surface of the each sphere in z-direction, the ϵ_r value of 4 spheres around the origin is decreasing from 2.5 to 1.5 while the absolute value of the distance to the center of sphere in z-direction is increasing up to the radius, and the ϵ_r value inside of remaining spheres is decreasing from 3.5 to 2.5 while the absolute value of the distance to the center of sphere in z-direction is increasing up to the radius) at 1 GHz

	BTET and TTET Value	Number Of Iterations	MVM Time (s)	Error (%)
MLFMA	-	293	70219	-
T-MLFMA	0.2	150	31529	1.48
	0.1	178	39149	1.25
	0.05	226	54824	0.32

Table 4.24: Numerical results of MLFMA and T-MLFMA for different threshold values for the array of inhomogeneous cones (each has a λ diameter and λ height, and ϵ_r value of each cone is linearly decreasing from the tip of the each cone to the base in the z-direction, the ϵ_r value is 7.5 and 1.5 at the tip and at the base, respectively) at 1 GHz

	BTET and TTET Value	Number Of Iterations	MVM Time (s)	Error (%)
MLFMA	-	84	10142	-
T-MLFMA	0.3	41	4426	2.77
	0.2	44	5166	1.56
	0.1	54	6781	1.14

each cone is λ. Moreover, the ϵ_r values are decreasing linearly from the tip of each cone to its base. The ϵ_r value is 7.5 at the tip and 1.5 at the base. The array is dicretized with 698,550 SWG functions. Scattered far-zone electric field, residual errors and MVM times in each iteration obtained from T-MLFMA are compared with that of the conventional MLFMA. The numerical results are depicted in Fig. 4.25 for 3 different threshold values of 0.3, 0.2, and 0.1 in red, blue and green colors, respectively. TTC and BTC values are set to 3. Moreover, Table 4.24 tabulates the details of the numerical results. We obtain approximately 2.3 times speed-up for the threshold value of 0.3 with a far-field error of 2.77% with respect to MLFMA. However, it is possible to achieve more accurate results for the threshold values of 0.2 and 0.1 with 1.56% and 1.14% far-field error values, respectively, obtaining 1.96 and 1.49 times speed-ups in MVM times.

Homogeneous Cube Results: We also consider the scattering from a dielectric cube with edge length λ and ϵ_r value of 3. The dielectric cube is discretized with 372,192 SWG functions and firstly illuminated by an x-polarized plane wave directly traveling toward the face of the cube, secondly it is illuminated by an x-polarized plane wave traveling toward the edge of the cube, and finally, it is illuminated by a y-polarized plane wave traveling toward the corner of the cube. Scattered far-fields obtained with MLFMA and T-MLFMA for each illumination are compared in Fig. 4.26(a), (b) and (c). The scattered field at $\phi = 90°$ and $\phi = 45°$ planes are sketched for edge and corner illuminations, respectively. Some details of T-MLFMA and MLFMA results are tabulated in Table 4.25. The trimming is applied for both basis and testing, with BTET and TTET have the same value of 0.1 and BTC and TTC values are set to 3 for T-MLFMA simulations. T-MLFMA enables 1.5, 1.9 and 1.7 times speed-up in MVM times with far-field errors of 1.58%, 7.79% and 5.12%, for face, edge and corner illuminations, respectively, with respect to the MLFMA results.

Table 4.25: Numerical results obtained with MLFMA and T-MLFMA for a homogeneous cube with λ edge length and $\epsilon_r = 3$ illuminated from the face, edge and corner at 1 GHz

	Illumination Type	Number of Iterations	MVM Time (s)	Error (%)
MLFMA	Face	48	2595	-
T-MLFMA		33	1741	1.58
MLFMA	Edge	52	2979	-
T-MLFMA		31	1569	7.78
MLFMA	Corner	52	2911	-
T-MLFMA		32	1710	5.12

Layered Square Column Results: Our final numerical result is a layered square column, which involves 3 different layers on top of each other [41]. Heights of these layers (from bottom to top) are λ, 2λ and λ, and the side length of the base of this column is λ. The bottom, middle and top layers have ϵ_r values of 2.5, 1.1 and 3.4, respectively. The object is discretized with 456,301 SWG functions by considering the mesh mating conditions. Scattered far-fields obtained with MLFMA and T-MLFMA are compared in Fig. 4.27. The trimming is applied for both basis and testing, and BTET and TTET have the same value of 0.1, and also BTC and TTC values are set to 3 for T-MLFMA simulation. With T-MLFMA, the number of iterations is decreased from 62 to 47, and MVM times drops from

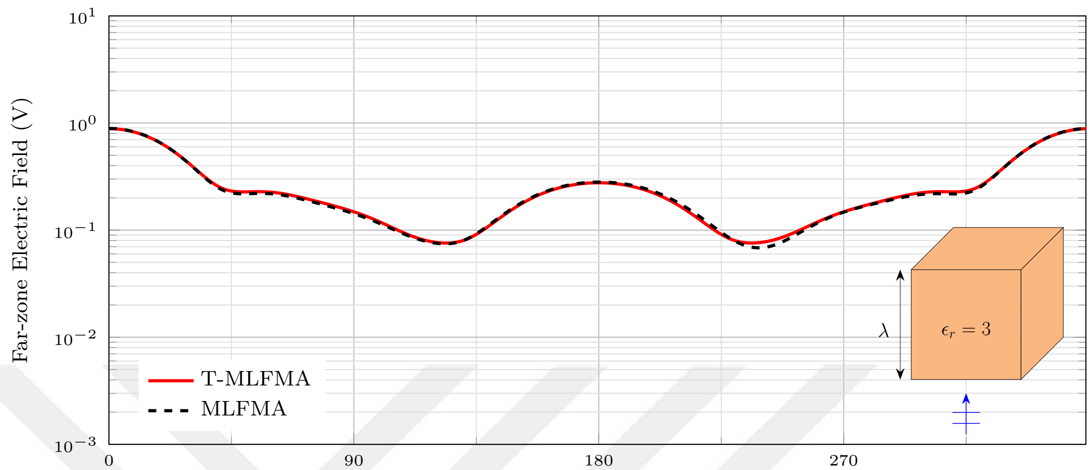

(a)

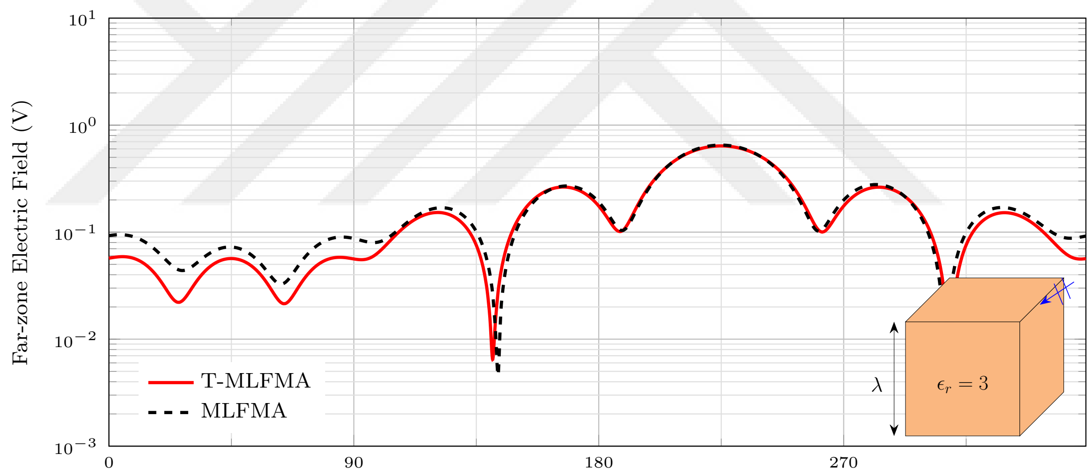

(b)

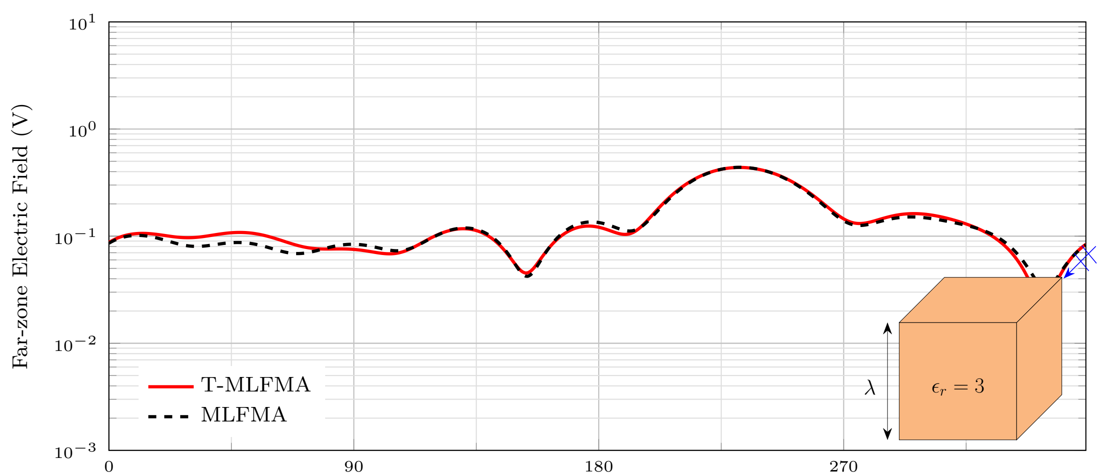

(c)

Figure 4.26: The scattered electric field of the homogeneous cube with λ edge length and ϵ_r = 3 obtained with MLFMA and T-MLFMA with BTET = TTET = 0.1 and BTC = TTC = 3 illuminated from the (a) face, (b) edge and (c) corner

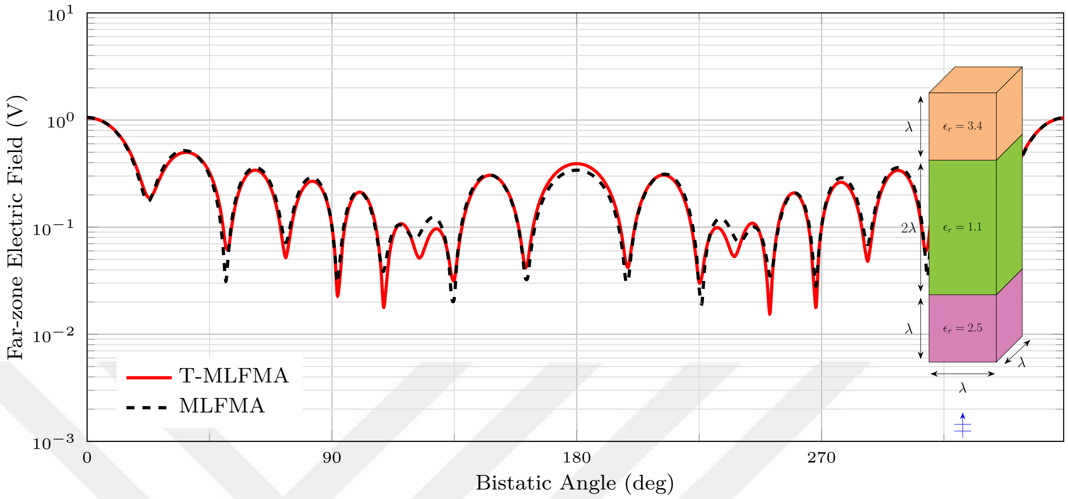

Figure 4.27: The scattered electric field of a layered square column obtained from MLFMA and T-MLFMA with BTET = TTET = 0.1 and BTC = TTC = 3

1600 seconds to 1042 seconds. T-MLFMA provides 1.7 times speed-up in MVM time and the far-field scattering results show high accuracy and consistency with a far-field error of 5.67% with respect to MLFMA.

In this section, we have showed and discussed the accuracy and efficiency of T-MLFMA for the scattering from several geometries such as cone, torus, cylinder, cube etc. in addition to spherical geometries. As we mentioned in FCNN part, we have showed that the training with only a small size of homogeneous dielectric spheres is sufficient to estimate current coefficients for relatively more complex dielectric objects, since the interactions of SWG functions are random in any sufficiently large volume.

Chapter 5

Conclusion

In this thesis, we have presented a successful application of T-MLMFA to VIEs, where the solution is accelerated by a progressive elimination of interactions during the iterations using FCNN and thresholding. The elimination of matrix columns is achieved by the estimation of converged current coefficients via ML techniques, while the elimination of rows is performed by a simple comparison of the actual and calculated RHS vectors. As a result of these eliminations, the tree structure is sparsified and significant acceleration is achieved due to the decrease in the number of iterations as well as MVM time per iteration as the iterations proceed.

In this study, we have given the results for T-MLFMA and the conventional MLFMA for scattering from relatively complex homogeneous and inhomogeneous dielectric geometries such as spherical shell layers, cone, torus, cylinder, and cube, etc., along with homogeneous dielectric sphere. The far-zone scattered fields, progress in residual errors, trimmed SWG counts and MVM time at each iteration are compared for T-MLFMA and the conventional MLFMA in each example. As a result, we achieved 1.5 to 10 times speed-up in MVM time compared to the conventional MLFMA depending on the geometry of the scatterer and the value of ϵ_r. Especially, significant accelerations are observed for larger objects with high values of ϵ_r, since the solutions are obtained generally in prolonging iterations in these examples. It should be noted that, in all simulations, the same FCNN, which is trained with only a group of small sized homogeneous spheres, is used. We observed that training with only a group of small sized homogeneous spheres is sufficient to estimate current coefficients for relatively more complex objects since the interactions of SWG functions are random in any volume. As a result, the successful application of T-MLFMA to VIEs enables us to obtain fast solutions for highly inhomogeneous, large complex objects, which are often encountered in various areas, such as biomedical imaging applications, radomes, electromagnetic absorbers. As a future work, the training group can be enhanced to attack much more complicated lossy dielectric geometries.

Bibliography

[1] W. Chew, E. Michielssen, J. M. Song, and J. M. Jin, Fast and Effcient Algorithms in Computational Electromagnetics. USA: Artech House, Inc., 2001.

[2] Weng Cho Chew, Jian-Ming Jin, Cai-Cheng Lu, E. Michielssen and J. M. Song, "Fast solution methods in electromagnetics," in *IEEE Transactions on Antennas and Propagation*, vol. 45, no. 3, pp. 533-543, March 1997.

[3] J. L. Volakis, "Alternative field representations and integral equations for modeling inhomogeneous dielectrics," in *IEEE Transactions on Microwave Theory and Techniques*, vol. 40, no. 3, pp. 604-608, March 1992.

[4] C. C. Lu, J. M. Song and W. C. Chew, "A multilevel fast multipole algorithm for solving 3D volume integral equations of electromagnetic scattering," *IEEE Antennas and Propagation Society International Symposium.* Transmitting Waves of Progress to the Next Millennium. 2000 Digest. Held in conjunction with: USNC/URSI National Radio Science Meeting (C, 2000, pp. 1864-1867 vol.4).

[5] W. Gibson, The Method of Moments in Electromagnetics. CRC Press, 2007.

[6] N. Engheta, W. D. Murphy, V. Rokhlin and M. S. Vassiliou, "The fast multipole method (FMM) for electromagnetic scattering problems," in *IEEE Transactions on Antennas and Propagation*, vol. 40, no. 6, pp. 634-641, June 1992.

[7] J. Song, Cai-Cheng Lu and Weng Cho Chew, "Multilevel fast multipole algorithm for electromagnetic scattering by large complex objects," in *IEEE Transactions on Antennas and Propagation*, vol. 45, no. 10, pp. 1488-1493, Oct. 1997.

[8] O. Ergul and L. Gurel, The Multilevel Fast Multipole Algorithm for Solving Large-Scale Computational Electromagnetics Problems. 2014.

[9] Jiming Song and Weng Cho Chew, "The Fast Illinois Solver Code: requirements and scaling properties," in *IEEE Computational Science and Engineering*, vol. 5, no. 3, pp. 19-23, July-Sept. 1998

[10] Y. Wu and W. Chew, "The Modern High Frequency Methods for Solving Electromagnetic Scattering Problems (Invited Paper)", *Progress In Electromagnetics Research*, vol. 156, pp. 63-82, 2016.

[11] Kechroud, R., Antoine, X. and Soulaïmani, A., 2005. Numerical accuracy of a Padé-type non-reflecting boundary condition for the finite element solution of acoustic scattering problems at high-frequency. *International Journal for Numerical Methods in Engineering*, 64(10), pp.1275-1302.

[12] L. Gurel and O. Ergul, "Hierarchical parallelization of the multilevel fast multipole algorithm (MLFMA)", Proceedings of the IEEE, vol. 101, no. 2, pp. 332-341, 2013.

[13] Ö. Ergul and L. Gurel, "A Hierarchical Partitioning Strategy for an Efficient Parallelization of the Multilevel Fast Multipole Algorithm," in *IEEE Transactions on Antennas and Propagation*, vol. 57, no. 6, pp. 1740-1750, June 2009, doi: 10.1109/TAP.2009.2019913.

[14] M. Yang, H. Gao, W. Song and X. Sheng, "An Effective Domain-Decomposition-Based Preconditioner for the FE-BI-MLFMA Method for 3D Scattering Problems," in *IEEE Transactions on Antennas and Propagation*, vol. 62, no. 4, pp. 2263-2268, April 2014,

[15] B. Khalichi, Ö. Ergül and V. B. Erüirk, "Near-Field-Based Preconditioning Technique in the Incomplete-Leaf MLFMA for Nonuniformly Discretized Electromagnetic Scattering Problems," *2021 IEEE International Symposium on Antennas and Propagation and USNC-URSI Radio Science Meeting (APS/URSI)*, 2021, pp. 1335-1336.

[16] M. Takrimi, Ö. Ergül and V. B. Ertürk, "Incomplete-Leaf Multilevel Fast Multipole Algorithm for Multiscale Penetrable Objects Formulated With Volume Integral Equations," in *IEEE Transactions on Antennas and Propagation*, vol. 65, no. 9, pp. 4914-4918, Sept. 2017.

[17] Jordan, M. and Mitchell, T., 2015. Machine learning: Trends, perspectives, and prospects. *Science*, 349(6245), pp.255-260.

[18] Liu, B., Aliakbarian, H., Ma, Z., Vandenbosch, G., Gielen, G. and Excell, P., 2014. An Efficient Method for Antenna Design Optimization Based on Evolutionary Computation and Machine Learning Techniques. *IEEE Transactions on Antennas and Propagation*, 62(1), pp.7-18.

[19] Wei, Z. and Chen, X., 2019. Physics-Inspired Convolutional Neural Network for Solving Full-Wave Inverse Scattering Problems. *IEEE Transactions on Antennas and Propagation*, 67(9), pp.6138-6148.

[20] Shan, T., Tang, W., Dang, X., Li, M., Yang, F., Xu, S. and Wu, J., 2020. Study on a Fast Solver for Poisson's Equation Based on Deep Learning Technique. *IEEE Transactions on Antennas and Propagation*, 68(9), pp.6725-6733.

[21] B. Karaosmanoğlu, "Electromagnetic Interaction Complexity Reduction Using Deep Learning," Ph.D. dissertation, Dept. Elect. Electron. Eng., Middle East Technical Univ., Ankara, Turkey, 2019.

[22] Karaosmanoglu, B., Ergul, O. (2021). Acceleration of MLFMA simulations using trimmed tree structures. *IEEE Trans. Antennas Propag.*, 69(1), 356–365.

[23] Conwell, P. R., Barber, P. W., Rushforth, C. K. (1984). Resonant spectra of dielectric spheres. *J. Opt. Soc. Am. A*, 1(1), 62.

[24] X. Millard and Q. H. Liu, "A fast volume integral equation solver for electromagnetic scattering from large inhomogeneous objects in planarly layered media," *IEEE Trans. Antennas Propag.*, vol. 51, no. 9, pp. 2393–2401, Sep. 2003.

[25] V. B. Kumar, S. S. Kumar and V. Saboo, "Dermatological disease detection using image processing and machine learning," *2016 Third International Conference on Artificial Intelligence and Pattern Recognition (AIPR)*, 2016, pp. 1-6.

[26] C. Balanis, Advanced Engineering Electromagnetics. Wiley, 2012.

[27] M. M. Botha, "Solving the volume integral equations of electromagnetic scattering," *J. Comput. Phys.*, vol. 218, no. 1, pp. 141–158, 2006.

[28] C.-C. Lu, P. Yla-Oijala, M. Taskinen, and J. Sarvas, "Comparison of two volume integral equation formulations for solving electromagnetic scattering by inhomogeneous dielectric objects," *Antenn. Propag. Soc. Int. Symp.*, pp. 1–4, June 2009.

[29] Schaubert, D., Wilton, D., Glisson, A. (1984). A tetrahedral modeling method for electromagnetic scattering by arbitrarily shaped inhomogeneous dielectric bodies. *IEEE Trans. Antennas Propag.*, 32(1), 77–85.

[30] M. Takrimi, "Implementation of a broadband multilevel fast multipole algorithm for multiscale electromagnetics problems," Ph.D. dissertation, Dept. Elect. Electron. Eng., Bilkent Univ., Ankara, Turkey, 2016.

[31] R. Graglia, "On the numerical integration of the linear shape functions times the 3-D Green's function or its gradient on a plane triangle," *IEEE Trans. Antennas Propag*, vol. 41, no. 10, pp. 1448–1455, 1993.

[32] Yu, J., 1984. Symmetric gaussian quadrature formulae for tetrahedronal regions. *Computer Methods in Applied Mechanics and Engineering*, 43(3), pp.349-353.

[33] S. Järvenpää, M. Taskinen, and P. Ylä-Oijala, "Singularity extraction technique for integral equation methods with higher order basis functions on plane triangles and tetrahedra," *Int. J. Numer. Meth. Eng.*, vol. 58, pp. 1149–1165, Oct. 2003

[34] M. Taskinen, “On the fully analytical integration of singular double integrals arising from the integral equation methods,” in *Computational Electromagnetics International Workshop (CEM)*, vol. 4, pp. 13–18, IEEE, Aug. 2011.

[35] L. Durand, P. Fishbane and L. Simmons, "Expansion formulas and addition theorems for Gegenbauer functions", *Journal of Mathematical Physics*, vol. 17, no. 11, pp. 1933-1948, 1976. Available: 10.1063/1.522831.

[36] Koc, S., Song, J., Chew, W. C. (1999). Error analysis for the numerical evaluation of the diagonal forms of the scalar spherical addition theorem. *SIAM J. Numer. Anal.*, 36(3), 906–921.

[37] Kalfa, M., Erturk, V. B., Ergul, O. (2021). Error Analysis of MLFMA With Closed-Form Expressions. *IEEE Trans. Antennas Propag.*, 69(10), 6618–6623.

[38] Y. Saad and M. H. Schultz, "GMRES": A Generalized Minimal Residual Algorithm for Solving Nonsymmetric Linear Systems," SIAM Journal on Scienti c and Statistical Computing, vol. 7, pp. 856-869, July 1986.

[39] D. P. Kingma and J. Ba, : A method for stochastic optimization," 2017.

[40] C. Mateo-Segura, A. Dyke, H. Dyke, S. Haq and Y. Hao, "Flat Luneburg Lens via Transformation Optics for Directive Antenna Applications," in *IEEE Transactions on Antennas and Propagation*, vol. 62, no. 4, pp. 1945-1953, April 2014.

[41] M. Kong et al., "Fast Electromagnetic Scattering Analysis of Inhomogeneous Dielectric Objects Over a Wide Incident Angle", *IEEE Antennas and Wireless Propagation Letters*, vol. 20, no. 8, pp. 1527-1531, 2021.